

**GRAPHITE NANOPATELET ASSEMBLIES FOR TRANSPARENT AND
CATALYTIC ELECTRODES IN DYE-SENSITIZED SOLAR CELLS**

By

Patrick Aderhold

A DISSERTATION

Submitted to
Michigan State University
in partial fulfillment of the requirements
for the degree of

Materials Science and Engineering – Doctor of Philosophy

2013

ABSTRACT

GRAPHITE NANOPLETELET ASSEMBLIES FOR TRANSPARENT AND CATALYTIC ELECTRODES IN DYE-SENSITIZED SOLAR CELLS

By

Patrick Aderhold

Dye sensitized solar cells (DSSCs) are a class of photovoltaic devices that provide high conversion efficiency without requiring high purity materials or capital-intensive production facilities. Research to improve performance in the individual components is active, but attention must be paid to methods that improve scalability and production cost as well. Graphite nanoplatelets (GNP), thin stacks of graphene sheets with nanometer-scale thickness and micron-scale lateral dimensions, provide a unique opportunity for creating DSSC electrodes with simple manufacturing techniques and low-energy processing. For the counterelectrode, a composite paper made by cofiltration and pressing of GNP and polypropylene (PP), yields a highly electrically conductive surface that is mechanically robust and chemically stable in electrolyte. Decoration of this surface with platinum nanoparticles (PtNPs) by a rapid microwave heating process produces a catalytic surface that rivals the current “thermalized” platinum standard counterelectrode in performance. The GNP/PP/PtNP system, however, requires lower processing temperature and requires a fraction of the Pt loading. For the transparent electrode, thin sheets of GNP can be deposited on glass surfaces to create highly transparent coatings for use in photoanode construction. Substrate interactions and post treatments are examined and techniques for optimization are outlined. Overall, GNP is shown to be a versatile and effective starting material for DSSC electrode construction and demonstrates its potential as a building-block in next-generation photovoltaic devices.

Copyright by
PATRICK ADERHOLD
2013

to anyone who manages to display skepticism and curiosity
amid rampant apathy, in you I find my inspiration

ACKNOWLEDGEMENTS

I am indebted to my advisor, Dr. Lawrence T. Drzal for his patience, professionalism and commitment (financially and intellectually) to my pursuits. My committee, consisting of Drs. Sakamoto, Barton and McCusker provided time and wisdom whenever they were called upon and I thank them for their candor and encouragement. Formerly on the committee, the late Dr. Baker deserves mention as well. He was as sharp as a professor can be and as humble as we all wish we were. I am one of the great many of his colleagues who wishes he took the time to express his great admiration when he had the chance.

The staff of the Composite Materials and Structures Center was also critically important to my development throughout my time at MSU. Brian and Per deserve special mention for their courtesy and equanimity when working with so many novice grad students. It was truly a feat beyond compare. Collaboration on this work with several members of the Chemistry department was invaluable as well. The most generous donation of thought and effort was from Lisa Harlow. Your advice on solar cell construction and electrochemical characterization saved me many months and much frustration.

To the graduate students in our lab who preceded me, I am forever grateful. Kiki, Steve, Dana and Tao, your generosity with your time was not unnoticed and I will always look to you with a feeling of solidarity. To the graduate students who arrived after me, Sanjib, Huang, Xian, Jinglei, Anchita, Yan and Dee, I can't help but be jealous of how quickly you've progressed. I know you will all be successful in your future endeavors and can only hope you found as much value in our discussions as I did from my senior colleagues.

And lastly, I owe a special word of appreciation to my parents. Always doting and attentive, always wishing for the best for their sons, I know you wanted nothing more than to hear that I was progressing quickly and achieving great things. I imagine hearing my frustration led to much vicarious discomfort and for that I am regretful. But know that I am now cured of hubris and naiveté and have a greater sensitivity to the struggles that masquerade as everyday life. We can all look forward to brighter days ahead.

TABLE OF CONTENTS

LIST OF TABLES	viii
LIST OF FIGURES	ix
Chapter 1 Introduction	1
Project Background	1
Dye-Sensitized Solar Cells	3
Graphene and Graphite Nanoplatelets	9
Chapter 2 Platinum-Decorated Catalytic Electrode Fabrication	18
Background	18
Microwave Platinum Nanoparticle Synthesis	18
Thin Film Catalytic Layer	19
Platinum-Decorated GNP Paper	25
Platinum-Decorated Composite Paper	34
Conclusions	56
Chapter 3 Platinum-Decorated Composite Papers for Dye-Sensitized Solar Cell	
Counterelectrodes	60
Background	60
Catalytic Activity	72
DSSC Fabrication	78
DSSC Characterization	83
Impedance Characterization	88
Conclusions	92
Chapter 4 Graphite Nano-platelet Assemblies for Transparent Electrodes	96
Background	96
Liquid-Liquid Interfacial Self-Assembly	98
Melt-Processing GNP/Polymer Substrates	105
Conclusions	109
Chapter 5 Conclusions and Future Work	114
Review	114
Transparent Electrode Improvements	115
Counterelectrode Improvement	120
DSSC Efficiency Improvement	124
PET Substrates for Flexible Devices	126
Conclusions	129

LIST OF TABLES

Table 3.1: Cell Parameter Averages	84
--	----

LIST OF FIGURES

Figure 1.1: Schematic depiction of a DSSC. The cell functions by (1) photon absorption (2) electron transport in the conduction band of the semiconductor (3) current through the external load (4) catalytic reduction of the redox shuttle and (5) regeneration of the dye. For interpretation of the references to color in this and all other figures, the reader is referred to the electronic version of this dissertation.....	3
Figure 1.2: Comparison of (A) sintered nanoparticle morphology (20 nm particle size) [28] and (B) nanotube array morphology (scale bar 5 μm) in DSSC semiconductor layers [29].....	6
Figure 1.3: Structure of (A) N3 dye and (B) N719 derivative (from [28] and [34], respectively).....	7
Figure 1.4: Visual description of carbon nanostructure formation: Fullerenes (left) carbon nanotubes (center) and graphite (right) are all composed of single or multiple sheets of graphene, folded or stacked [46].....	10
Figure 2.1: Discrete PtNPs seen on GNP, following rapid, microwave heating [13].....	19
Figure 2.2: Digital images of (A) GIC prior to microwave exfoliation and (B) the highly expanded worms produced by rapid microwave heating. SEM images show (C) low magnification of the worms, showing their elongated shaped and (D) higher magnification showing the pleated sturcture follwing expansion.....	20
Figure 2.3: FESEM image of (A) control GNP samples wihtout PtNP synthesis treatment and (B) PtNP-decorated GNP particle. With the exception of occasional aggregates, uniform size and coverage of PtNPs is observed.....	22
Figure 2.4: Film delamination leading resulting form rapid heating in polar solvent. Stable GNP film (A) prior to microwave heating and (B) after microwave heating.....	23
Figure 2.5: TEM and FESEM observation of PtNPs on GNP powder after rapid, microwave synthesis, washing and centrifugation (scalebars at 5 nm and 10 nm respectively).....	24
Figure 2.6: Continous PtNP-decorated GNP coatings on glass substrates seen on (A) white background, (B) back-lit and (C) tilted to show minimal topology of film.....	24
Figure 2.7: (A) Schematic for GNP paper formation and digital images (B) before and (C) after pressing and annealing. Image (D) shows a cross-sectional view of the paper embedded in epoxy, polished, gold-coated and mounted for SEM observation.....	26

Figure 2.8: Thermogravimetric analysis of GNP paper (run at 10°C/min in air). (A) shows the negligible weight loss of the GNP paper up to the onset of graphite degradation at around 600°C and (B) shows the comparison of the derivative of weight loss percentage, notably the lack of the PEI degradation peak around 450°C, indicating high purity of the material.	27
Figure 2.9: (A) Control untreated GNP paper sample in comparison to (B) GNP/PtNP paper after nanoparticle synthesis, washing and drying. Uniform coverage of discrete nanoparticles is seen, similar to thin-film GNP/PtNP samples.	29
Figure 2.10: (A) GNP/Pt electrode after pressing onto molten Surlyn on glass. FESEM imaging of (B) 20µM and (C) 200µM CPA-treated samples show presence of numerous PtNPs even <i>after</i> rigorous pressing.	30
Figure 2.11: Representative images from multiple locations on 20 µM CPA-treated GNP paper. FESEM images (A,C and E) were imported to image analysis software to calculate their particle size distributions (B, D and F, respectively).	32
Figure 2.12: Representative images from multiple locations on 200 µM CPA-treated GNP paper. FESEM images (A,C and E) were imported to image analysis software to calculate their particle size distributions (B, D and F, respectively).	33
Figure 2.13: TGA analysis of pure PP degradation in air (10°C/min ramp rate)	35
Figure 2.14: Leeching process to remove PEI consisting of (A) placing dried GNP/PP papers onto a porous PTFE cloth (B) covering with a second porous PTFE cloth and (C) filling with water and stirring at room temperature for over 12 hours	36
Figure 2.15: Thermogravimetric analysis of GNP/PP papers (run at 10°C/min in air). The leached papers show (A) ~50wt% mass loss at the onset of GNP degradation above 600°C. The derivative of wt% loss (B) shows a sharp peak for PEI decomposition that is seen in none of the leached papers, indicating complete removal.....	37
Figure 2.16: Comparison of (A) electrical conductivity and (B) sheet resistance of GNP, GNP/PP and FTO samples at various stages of processing.....	39
Figure 2.17: GNP/PP paper after pressing (A) showing great flexibility. Sample is able to be curled up to a small radius (B) and then uncurled (C) showing no wrinkles, creases or tears.	40
Figure 2.18: Stress-strain curves for pure GNP papers and composite papers made from 50/50wt% GNP and PP. Strain rate of 0.1%/min was used.....	41
Figure 2.19: Confocal microscopy images of (A) unpressed GNP paper (B) pressed GNP paper and (C) pressed GNP/PP paper. All images taken with fluorescein	

isothiocyanate dye in Leco mounting epoxy (~0.25 $\mu\text{g/ml}$) with excitation by 488 nm Ar laser, 505 nm long-pass emission filter and U-Plan Apo 40X oil objective (NA 1.3).	42
Figure 2.20: FESEM images of (A) un-pressed GNP paper (B) pressed GNP paper and (C) pressed GNP/PP paper.	43
Figure 2.21: XPS characterization of oxygen plasma-treated GNP/PP paper surface.	44
Figure 2.22: FESEM observation of GNP/PP surfaces after (A) 1 minute (B) 5 minutes and (C) 40 minutes of oxygen plasma treatment.	45
Figure 2.23: FESEM observation of GNP/PP surface after 40 min oxygen plasma treatment. Some regions show (A) noticeable degradation of GNP particles while others (B,C) show residual polymer presence pooling in depressions in the surface.	46
Figure 2.24: Placement of GNP/PP papers in plasma reactor in (A) standard orientation and (B) inverted orientation, 5 mm above the chamber surface. Image (C) shows inverted papers to be well within the range of the ionization of the oxygen. Image (D) is a representative region of the treated GNP/PP paper surface, showing regions that includes <i>small</i> fractions of oxidized and crumpled graphene platelets and (E) is representative of areas that are clear of oxidized species, showing a clean GNP surface for PtNP decoration.	47
Figure 2.25: Surface presence of oxygen on GNP/PP papers as a function of plasma treatment time.	48
Figure 2.26: Deconvolution of the C-peak in XPS signal. Samples show an increase in the signal attributed to graphite as treatment times increase from (A) 0 min to (B) 1 min (C) 5 min (D) 10 min (E) 20 min and (F) 40 min.	49
Figure 2.27: Representative images showing PtNP coverage of plasma-treated GNP/PP surfaces made by rapid microwave heating in (A) 20 (B) 200 and (C) 1000 μM CPA solutions. The increase in number density of PtNPs from low to high [CPA] can be clearly seen as well as the monodispersity of particle size and lack of aggregates.	56
Figure 3.1: Top-down view of FTO surface (A) before and (B) after Pt coating by thermal decomposition of precursor at 400°C for 15 min. Large aggregates seen over whole surface of sample, a sharp contrast to the discrete PtNP coverage seen in (C) GNP/PP/PtNP samples prepared by rapid microwave irradiation. All images are at identical magnification.	61
Figure 3.2: Top-down view of thermalized FTO system at low magnification with (A) secondary electron (SE) detector and (B) back-scatter electron detector. Using a high tilt angle of 60° and the SE detector illustrates the large size of Pt aggregates on top of the FTO crystallites.	62

Figure 3.3: (A) Elemental abundance and (B) Pt loading at surface of GNP/PP/PtNP and FTO/Pt samples as measured by XPS. Measurements were made on a Perkin Elmer Phi 5400 ESCA system with a magnesium $K\alpha$ X-ray source. Samples were analyzed at pressures between 10^{-9} and 10^{-8} torr with a pass energy of 29.35 eV and a take-off angle of 45° . The spot size is roughly $250 \mu\text{m}^2$. Atomic concentrations were determined using previously determined sensitivity factors. All peaks were referenced to the signature C1s peak for adventitious carbon at 284.6 eV. 64

Figure 3.4: Quantification of Pt loading by XPS and ICP-MS..... 65

Figure 3.5: Top images show GNP/PP/PtNP samples adhered to FESEM mount (A) before and (B) after delamination with adhesive tape. Below, images show 20 μM CPA-treated GNP/PP/PtNP sample (C) before and (D) after delamination experiment. 200 μM CPA sample (E) before and (F) after and 1000 μM CPA sample (G) before and (H) after. 68

Figure 3.6: FESEM imaging of the surface of the suspension-processed, nanoparticle-decorated GNP. Image (A) shows a single GNP particle with brightly visible PtNPs on top and faint PtNPs visible on the bottom of the platelet. Image (B) shows a single, uncoated GNP particle sitting on top of one that is nanoparticle-decorated. Image (C) is a 5X zoom of image (B). 70

Figure 3.7: Bottom of GNP/PP/PtNP paper showing (A) no PtNP coverage over most of the imaged area (B) sparse PtNP coverage in some areas and (C) very infrequent dense coverage of PtNPs and large aggregates. 71

Figure 3.8: Cyclic voltammetry baseline measurements of commercial Pt foil working electrode. Three electrode cell with Pt foil counterelectrode and Ag/AgCl reference electrode. Electrolyte was 5 mM LiI, 0.5 mM I_2 and 0.1 M LiClO_4 . Scan rate was 50 mV/s..... 73

Figure 3.9: Images showing (A) GNP/PP/PtNP and (B) FTO/Pt electrode assembly and reflected light microscope images used for area measurement of (C) GNP/PP/PtNP and (D) FTO/Pt catalytic surfaces. 74

Figure 3.10: Three-cell configuration for measuring catalytic activity of GNP/PP/PtNP and FTO/Pt surfaces. 75

Figure 3.11: CV comparison of catalytic activity on the 10th cycle of GNP/PP/PtNP and FTO/Pt samples. Electrolyte was 5 mM LiI, 0.5 mM I_2 and 0.1 M LiClO_4 . Scan rate was 50 mV/s..... 76

Figure 3.12: CV comparison (10th cycle) of GNP/PP/PtNP, GNP/PP control and thermalized Pt electrodes. Electrolyte was 5 mM LiI, 0.5 mM I ₂ and 0.1 M LiClO ₄ . Scan rate was 50 mV/s.....	77
Figure 3.13: FESEM images of a GNP/PP/PtNP paper (1000 μM CPA) after CV cycling, acetonitrile soaking and drying.....	78
Figure 3.14: Counterelectrode fabrication process including (A) heating of Surlyn to molten state (B) cutting GNP/PP/PtNP paper to fit glass substrate and (C) pressing GNP/PP/PtNP onto molten Surlyn with PFTE mask to prevent abrasion. Image (D) shows the completed counterelectrode.....	79
Figure 3.15: Comparison of sealing efficacy of (A) pure GNP paper and (B) GNP/PP paper.....	80
Figure 3.16: Full cell assembly, including photoanode, counterelectrode, EPDM rubber gasket, binder clips to provide pressure for seal and syringes for loading electrolyte.....	82
Figure 3.17: All JV curves measured for FTO/Pt standards and GNP/PP/PtNP-based cells.....	84
Figure 3.18: Power conversion efficiency averaged for each group of (4) cells.....	85
Figure 3.19: Comparison of representative JV curve from each sample group.....	86
Figure 3.20: Representative JV curves without illumination.....	87
Figure 3.21: Nyquist plots of catalytic electrode surfaces at (A) low impedance values and (B) zoomed out to show the high impedance values.....	89
Figure 3.22: EIS measurement of GNP/PP/PtNP (1000 μM) electrode in comparison to FTO/Pt system.....	91
Figure 4.1: Comparison of electrical and optical properties for graphene, and ITO (as well as other potential transparent electrode systems such as silver wire mesh and single wall carbon nanotubes). Image adapted from [19].....	97
Figure 4.2: Thin film deposition of GNP resulting in highly transparent and conductive layers. Scalebar in lower right image is 1 in. Adapted from [24]......	99
Figure 4.3: (A) Schematic representation of liquid-liquid, interfacial self-assembly of GNP. (1) sonication of GNP in chloroform to mechanically exfoliate and deaggregate (2) addition of water and further sonication, followed by phase separation (3) disruption of GNP-rich layer but jet of liquid from pipet (4) formation of second interface at the top of the water phase (5) evaporation of chloroform, creating GNP layer at air-water interface (6) deposition of GNP	

layer on glass substrate. Image (B) shows the GNP-rich interface between the water on top and chloroform on bottom and image (C) shows the thin layer of GNP at the air-water interface after disruption of the water-chloroform interface and evaporation of surface chloroform.....	101
Figure 4.4: (A) Digital image and (B) optical micrograph of thin film GNP coating on glass. (C) Optical and electrical properties from UV-vis spectroscopy and 2-point electrical conductivity measurements.....	103
Figure 4.5: Surface treatment were performed on glass slides, including silane reaction with (A) trichloro(phenyl)silane (TCPS) and (B) trichlorophenethylsilane (TCPES). (C) Water contact angle measurements for various surface treatments.	104
Figure 4.6: Cross section of pressed GNP paper embedded in epoxy after polishing, oxygen plasma treatment and Tugsten coating.....	106
Figure 4.7: DSC characterization of PET film. Large endotherm at 250°C indicates melt transition.	107
Figure 4.8: GNP/PET assembly (A) before and (B) after pressing at 250°C/1000 psi. Image (C) shows and examples of one delamination step and image (D) shows the high loading of GNP platelets in each of the subsequent delamination steps (each strip of tape is highly opaque after delamination). Image (E) shows the remaining PET/GNP structure, with very high loading of GNP remaining that cannot be removed by micromechanical cleavage.	108
Figure 5.1: GNP from microwave exfoliated GIC (Asbury grade 3772) dropcast on Al stub and imaged by FESEM after (A) 1 min and (B) 10 min sonication in chloroform.	116
Figure 5.2: xGnP® from XG Sciences (grade M-25) after (A) 1 min and (B) 10 min sonication in chlorofom.	116
Figure 5.3: TEM images of individual graphene sheets produced by various liquid-exofoliation and extraction methods. Image (A) from bath sonication in N-methylpyrrolidone [1]. Image (B) from bath sonication in water/sodium dodecylbenzene sulfonate [2]. Image (C) from bath sonication in water/1-pyrenecarboxylic acid [3].	117
Figure 5.4: GNP films on glass were exposed to a 450 W, 30 min, 265 mtorr oxygen treatment. A Digital image (A) of the samples show dark, untreated GNP layers compared to more transparent, oxygen plasma treated samples ones. SEM imaging of the samples (B) before and (C) after the treatment show drastic changes in paticle coverage.	119

Figure 5.5: UV-vis comparison of GNP/PP and FTO/Pt counterelectrode samples. (A) Spectra of various samples plotted for range of visible light and (B) comparison of average surface reflectance over visible range.	121
Figure 5.6: (A) Digital image of high surface area xGnP-C-700 material deposited on thin layers of low surface area graphite by multiple liqui-liquid, interfacial self- assembly interaction. (B) SEM imaging of the surface shows the high surface area of the deposited material, likely improving catalytic ability.	123
Figure 5.7: Digital images of (A) 5 mm by 5 mm photoanode after dyeing and drying and (B) cell construction with standard FTO/Pt counterelectrode and LiI, I ₂ , TBP electrolyte.	125
Figure 5.8: JV curve comparison various FTO/Pt DSSC configurations.	126
Figure 5.9: GNP/PP/PtNP paper on PET film (A) before and (B) after pressing. Image (C) shows the stability of the film during repeated flexing.	127
Figure 5.10: PtNP presence on PET/GNP/PP/PtNP structure after pressing and oxygen plasma treatment. Confirmation of Pt presence was provided by back- scatter imaging of the same area.	128

Chapter 1

Introduction

Project Background

Concern over the energy infrastructure in the developed world is well established. Between dwindling fossil fuels stocks [1] and the indications of anthropogenic climate change [2], the need to switch to clean, renewable energy sources is apparent. A portfolio of technological options is under development, including hydroelectric power [3], wind generation [4], chemical conversion of biomass [5] and geothermal power [6]. Perhaps most promising, though, is conversion of incident solar energy. Simple calculations show a staggering 1366 W/m^2 of incident solar energy reaching the earth from the sun [7]. This is such a large amount that, despite losses to reflection and absorption in the atmosphere, even capturing 0.1% of the sunlight falling on land would be enough to satisfy the energy demands of the entire world [7]. The first photovoltaic (PV) devices, developed at Bell Labs over fifty years ago, relied on doped, single-crystal silicon as the semiconductor and light absorber [8]. With efficiencies steadily climbing and reaching as high as 25%, according to the most recent National Renewable Energy Laboratory reports [9], it is no surprise that silicon-based devices continue to dominate the market, with recent data showing a 91% market share of commercial PV sales [10]. High efficiencies compared to competing technologies accounts for the market dominance. However, despite rapid growth in the last few years (up 250% from 2008 to 2010), PV still accounts for only 0.8% of total electricity capacity (40 GW of out of 4950 GW globally) [11]. Despite heavy investment and years of refining, there are limits to

the cost reductions that silicon-based PVs can obtain. Production of the high-purity silicon is an energy-intensive process, requiring temperatures in excess of 1400°C [12]. Additionally, manufacturing the thin wafers from high-purity silicon ingots lead to significant material losses, only confounding the problem [8]. For PV technology to expand beyond its slim market share and make a significant dent in world energy capacity, a different paradigm is necessary, un-hindered by the materials and manufacturing limitations of high-purity silicon.

Two particular approaches have widespread interest, organic solar cells and dye-sensitized solar cells (DSSCs). Organic solar cells are an extremely active research topic because of the great potential for low-cost manufacturing. Large-scale “roll-to-roll” and printing techniques have the potential to supply large quantities of organic devices at prices that silicon-based technologies can’t match [13]. Though the future looks bright for this technology, overcoming stability issues [14] and improving cell efficiency is imperative. Until recently, organic devices managed to reach only 4-5% conversion efficiency, far below competing technologies [15]. However, record cell efficiencies have been reported in the last few years. In scientific literature, the record stands at 7.4%, reported by Liang et al in 2010 [16], but claims by commercial developers (Heliatek, based in Dresden, Germany) put the mark at 10.7% as of 2012 [9,17]. Though quite impressive, there are no guarantees these rapid increases in performance will continue. This thesis, therefore, will focus on the other primary competition for silicon-based solar devices: dye sensitized solar cells (DSSCs). This category of solar cell has the potential for low cost production as well, but it currently bests organic devices by a

significant margin. The record conversion efficiency of a DSSC was recently reported to be 15% [18], making it obvious why this technology is such an active research topic.

Dye-Sensitized Solar Cells

First proposed by O'Regan and Grätzel in 1991 [19], DSSCs function by delegating the roles of photon absorption, electron transport and hole transport to different chemical species. Rather than a single, high-purity semiconductor material filling all three roles, each component can be optimized for its particular task, thereby improving cell efficiency. A schematic of the construction of a DSSC is shown below in Figure 1.1.

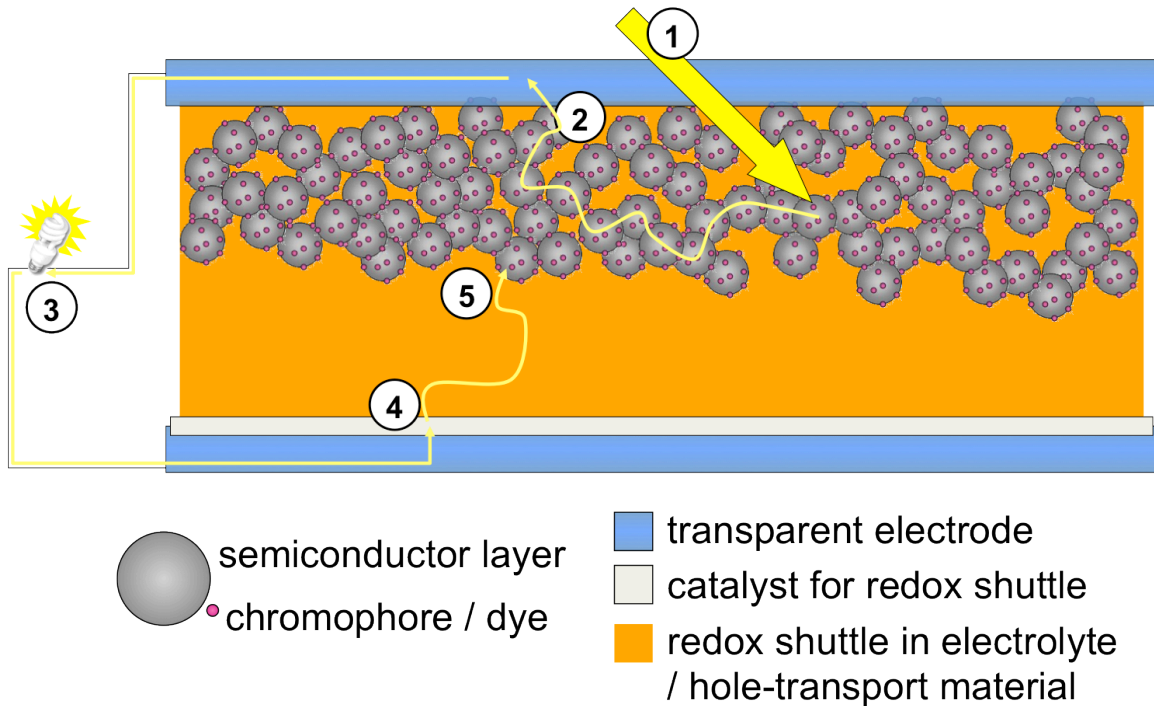


Figure 1.1: Schematic depiction of a DSSC. The cell functions by (1) photon absorption (2) electron transport in the conduction band of the semiconductor (3) current through the external load (4) catalytic reduction of the redox shuttle and (5) regeneration of the dye. For interpretation of the references to color in this and all other figures, the reader is referred to the electronic version of this dissertation.

A photon passes through a transparent, conductive oxide layer, penetrates into the mesoporous, semiconductor layer and excites an electron in the chromophore (step 1 in Figure 1.1, above). This excited electron is then injected into the conduction band of the mesoporous semiconductor and travels towards the current collector (step 2) [20]. Excited electrons are then transported through the external load and return to the counterelectrode (step 3). At the counterelectrode, reduction of triiodide (I_3^-) to iodide (I^-) is facilitated by a catalyst (typically platinum) (step 4), followed by diffusion of the I^- towards the depleted dye and reduction of the oxidized dye, back to its original state (step 5) [21].

There are countless, minor deviations from this basic setup, but the premise of the DSSC remains the same: simple, inexpensive semiconductor material to form the heart of the cell, rather than high-purity silicon. Specifically, titania (TiO_2) (used in the vast majority of DSSC configurations) is so “cheap and abundant” that it is widespread in applications as diverse as health care products, house paint and chewing gum [22]. Additionally, the TiO_2 structure can be formed by sintering processes as low as $230^\circ C$ [20] (but never higher than $450^\circ C$ [19]), making the fabrication process far less energy-intensive than silicon-based devices. This is a critical feature because the “energy payback” of silicon devices (“the time it takes for a photovoltaic system to generate an amount of energy equal to that used in its production”) can be as high as six years [23]. Though life cycle assessments have not yet been performed on DSSCs, they are expected to reduce this payback time significantly [20]. Additional advantages of DSSCs over standard silicon-based devices, include its effectiveness in diffuse light [24] and higher

operating temperatures. Under maximum irradiation, it is common for cells to reach up to 60°C during operation, enough to curtail silicon-based PV performance by 20%. DSSCs, however, see “practically no effect on the power conversion efficiency” [20].

As mentioned earlier, the selection and optimization of individual components makes the number of DSSC configurations virtually limitless. The most exhaustive research, though, is focused on structured growth of the mesoporous semiconductor layer. The high surface area of doctor-bladed 30 nm spheroidal particles allows for excellent dye coverage in a thin (~10 μm) layer. Despite its simple preparation and lack of structure within semiconductor layer, it yields an impressive 7.9% efficiency at AM 1.5 conditions (the intensity and spectrum equivalent to solar noon in North America) [19]. However, a high density of trap states results from the sintering of individual nanoparticles, as opposed to longer, defect-free TiO₂ crystallites. These trap sites limit electron transport to the electrode and end up lowering cell efficiency because of back reactions to the redox species in the electrolyte [25]. Cao et al suggest that these trap sites may be the limiting factor in electron transport [26]. Alternatively, patterned nanowires allow for much faster electron transport over long distances, reducing back reactions and allowing for improved cell efficiency [27]. A comparison of the porous, sintered nanoparticle and ordered nanotube array morphologies can be seen below in Figure 1.2.

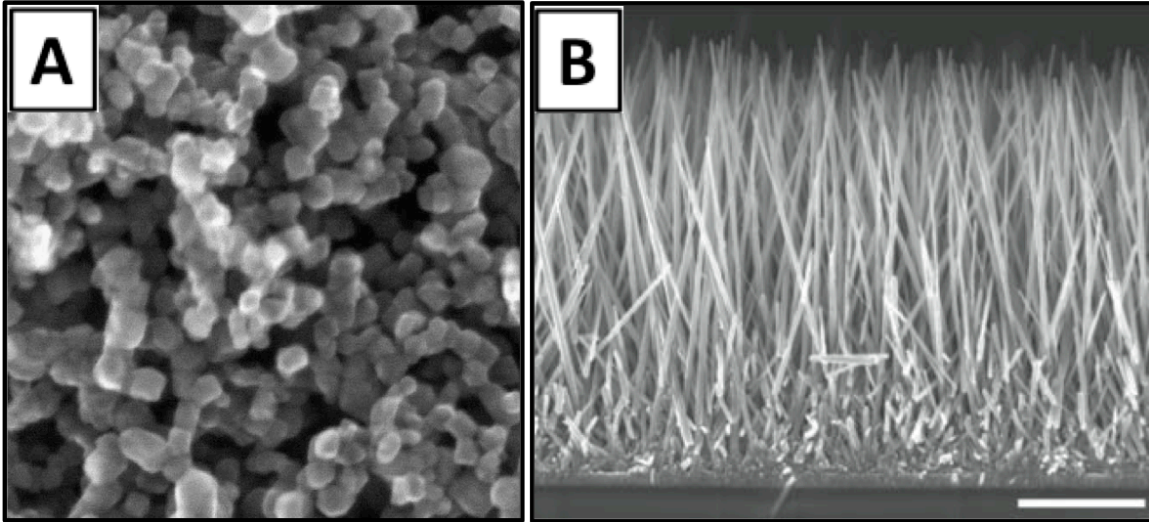


Figure 1.2: Comparison of (A) sintered nanoparticle morphology (20 nm particle size) [28] and (B) nanotube array morphology (scale bar 5 μm) in DSSC semiconductor layers [29]

Several different methods have been presented to obtain ordered TiO_2 growth, such as anodization of titanium metal [27,30], “seed growth” from ZnO quantum dots [29] and “surfactant-assisted self-assembly” of nanocrystallites [31], to name a few. Zhe et al. note the value of removing defect sites, stating that the nanotube arrays (as opposed to sintered nanoparticles) had “similar transport times, whereas recombination was 10 times slower” [27]. Great gains will be made in the coming years as ordered semiconductor layers are improved, but this is by no means the only avenue for DSSC optimization.

Dye engineering is another area of major interest. Dozens of different species have been examined for their potential to absorb light, adhere to the semiconductor substrate and allow for rapid injection of the excited electron, while limiting back reactions to the electrolyte. In 1993, the “N3” dye (cis-bis-(4,4'-dicarboxy-2,2'-bipyridine) dithiocyanato-ruthenium(II), pictured below in Figure 1.3) allowed for DSSC efficiency as high as 10%, a record at the time [32]. Preserving the ruthenium center and altering the attached ligands, led to the development of the highly successful “N719” dye in 2001

[33]. N719 was the standard-bearer for quite some time, with dyes that improve on absorption and overall efficiency only recently being published [34,35].

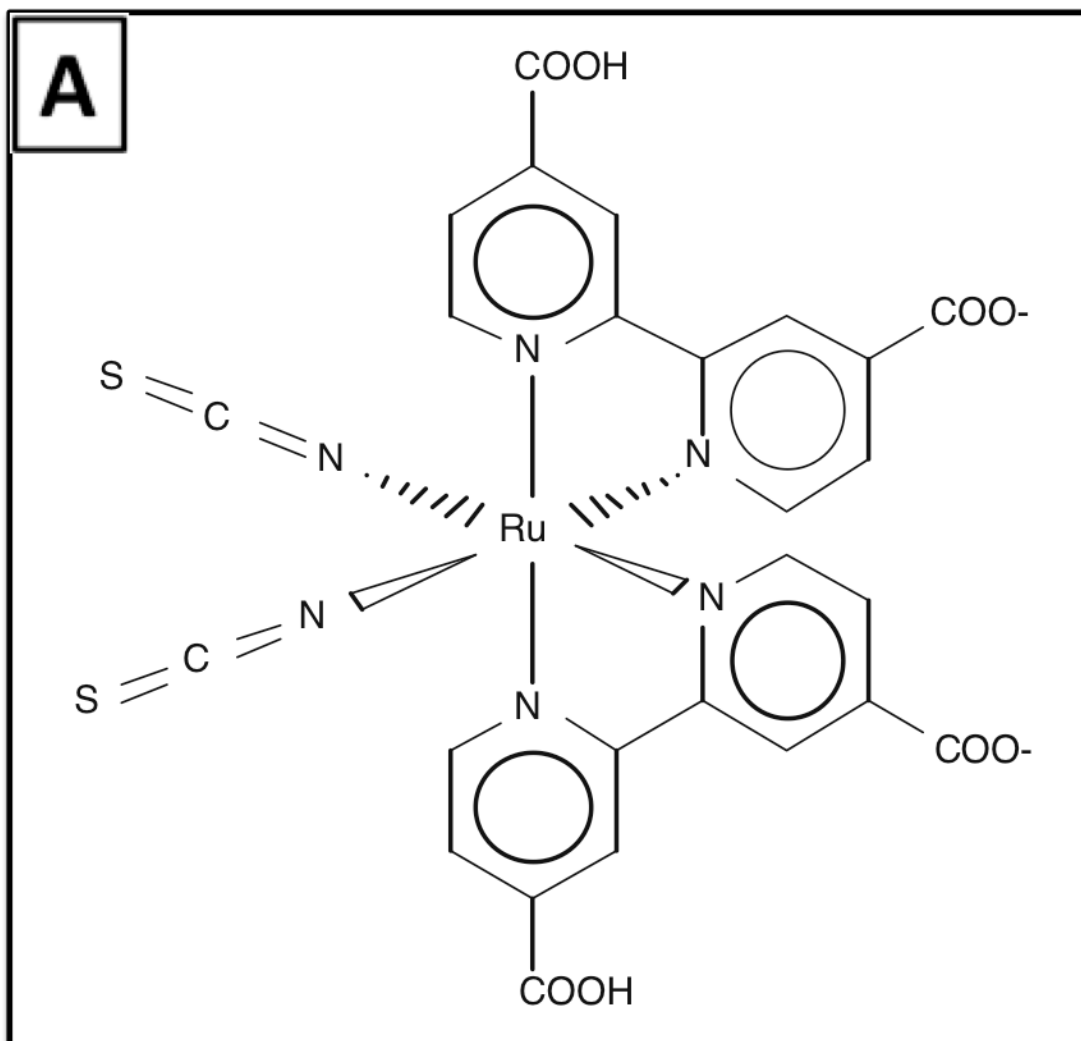
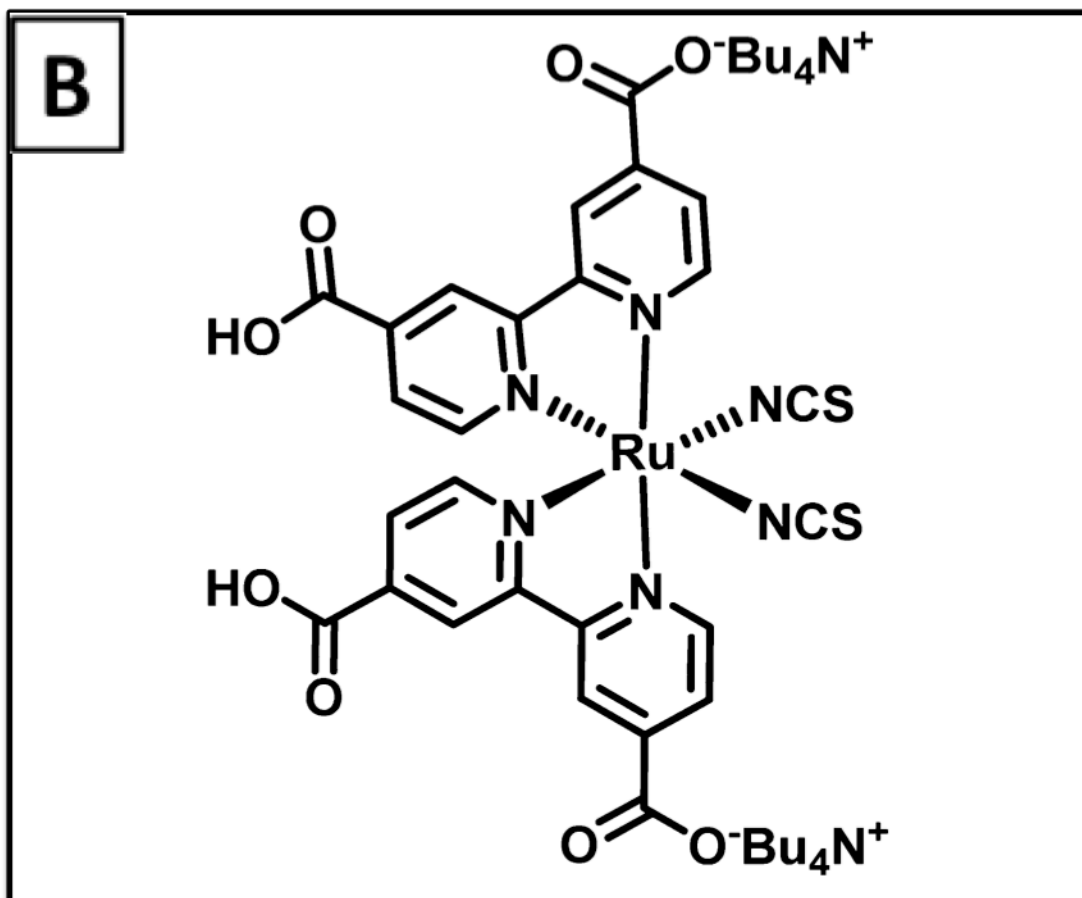


Figure 1.3: Structure of (A) N3 dye and (B) N719 derivative (from [28] and [34], respectively)

Figure 1.3 (cont'd)



Other, more drastic alterations, have led to ruthenium-free dyes, such as iron-based complexes [36], purely organic species [37] and graphene quantum dots [38]. Some of these approaches focus on expanding the absorption profile of the dye into the IR or UV ranges while others provide economic advantages, such as replacing rare earth elements with more common building blocks. The extensive literature suggests further improvements will be made and the ideal dye (or dyes) for commercial DSSC usage has yet to be determined.

In parallel to efforts to improve the semiconductor and dye components, revisions to the original I^-/I_3^- redox shuttle have been made as well. One of the highest conversion

efficiencies on record was reported by a Yella et al., who utilized a cobalt (II/III) redox shuttle. Their 12.3% efficiency was obtained because of the higher (935 mV vs. 800 mV) open circuit potential with the cobalt-based electrolyte [39]. Other groups have shifted away from liquid electrolytes, citing concerns over evaporation and leaking. New ionic liquid [40] and gel electrolyte [41] systems report lower overall cell efficiencies, but open the door to DSSCs with more robust operating conditions. By removing the volatile solvent from the system, cells avoid the problems of leakage and evaporation, both of which lead to cell failure.

Semiconductor patterning, dye engineering and electrolyte modification account for the bulk of research, but certainly not the entirety. Adjustments such as scattering layers to improve absorption [42], blocking agents on the semiconductor to limit back reactions [43] and numerous other alterations affect overall cell performance as well. With so many variables to adjust, cell design can be quite difficult. For this reason, one of the best ways to increase the likelihood of DSSC commercialization is to work on reduction of the cost of the cell, rather than working for incremental gains in efficiency. At Michigan State University, this type of optimization is under way.

Graphene and Graphite Nanoplatelets

One particular initiative is the use of graphite nanoplatelets (GNP) to assemble electrode structures to replace the current transparent conductive oxides (TCOs), most commonly made from indium tin oxide (ITO) or fluorine-doped tin oxide (FTO). Graphite is a layered material, composed of several sheets of graphene, an sp^2 -bonded carbon structure [44]. These stacked sheets are tightly bound by Van der Waals forces,

because of the high surface area of the material [44]. Very similar in chemistry to fullerenes and carbon nanotubes (CNTs) (as shown below in Figure 1.4), it differs in that it is a naturally occurring material, formed by geological processes [45].

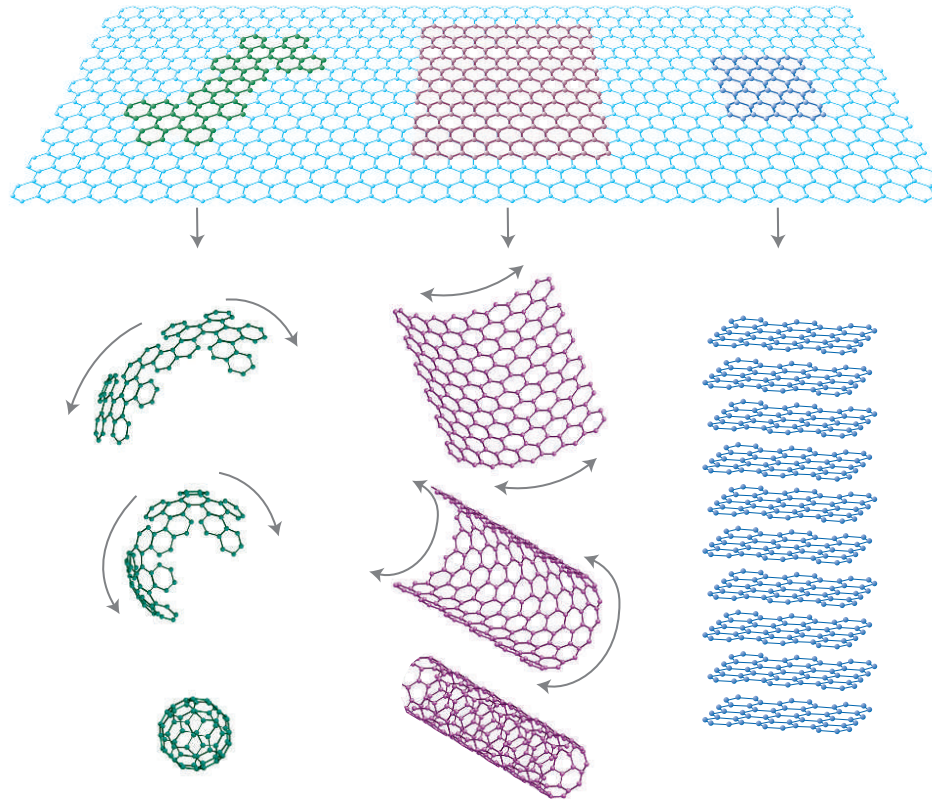


Figure 1.4: Visual description of carbon nanostructure formation: Fullerenes (left) carbon nanotubes (center) and graphite (right) are all composed of single or multiple sheets of graphene, folded or stacked [46]

Because it is naturally abundant, as opposed to fullerenes and CNTs, which are formed by highly energetic processes with small yields [47,48], the potential for large-scale usage at lost cost is far greater [49]. In its natural state, graphite is of little use. It is a polycrystalline material with relatively low electrical conductivity [50] and a low aspect ratio because of the thickness of the graphene stacks [45]. However, by chemical [51], thermal [52] or mechanical [53] exfoliation (separation of the graphene sheets), these stacks can be broken down to fewer than ten sheets. Some groups have even reported

low yields of individual graphene sheets and few-layer graphene (FLG) containing just two or three graphene sheets by proper selection of solvent and extensive centrifugation [54,55]. These different preparation methods have proven quite versatile, ranging from small, extremely thin FLG sheets to larger-scale processing of thicker stacks, capable of gram-quantity yields. Larger-scale processing relies on acid-intercalation, rapid microwave heating to expand the material and high-intensity mechanical exfoliation (with an ultrasonicator horn) to yield thin sheets, with controllable width, allowing for high-aspect ratio material [49]. These graphite nanoplatelets (GNP) have proven to be a multifunctional material, finding utility in applications as diverse as structural nanocomposite materials [56], batteries [57], thermoelectrics [58] and optical electronics [59].

The unique morphology and chemistry of GNP are what allow its assembly into such numerous configurations. Two such methodologies are proposed here for constructing DSSC components that should rival current devices in terms of performance, while having greater potential for cost savings. First, formation of a catalytic, counterelectrode is possible based on forming a highly electrically conductive GNP substrate [60], followed by platinum nanoparticle (PtNP) synthesis [61]. The final structure provides high catalytic surface area and fast electron transport, both critical for a DSSC counterelectrode. Secondly, a thin assembly of GNP can be placed on a transparent, non-conductive substrate as a replacement for the TCO layer of the DSSC. Preliminary work by Biswas et al. has shown that with sufficiently thin starting GNP material, conductive layers can be formed with electrical conductivities rivaling that of ITO [59]. This combination of lost-cost, abundant starting materials and simple, scalable processing has

great potential for changing the economics of DSSC fabrication and will be described in detail in the following chapters.

REFERENCES

REFERENCES

- [1] M. Asif, T. Muneer, *Renewable and Sustainable Energy Reviews* **2007**, *11*, 1388–1413.
- [2] S. H. Kim, C. MacCracken, J. Edmonds, *Progress in Photovoltaics: Research and Applications* **2000**, *8*, 3–15.
- [3] I. Yuksel, *Energy Sources, Part B: Economics, Planning, and Policy* **2007**, *2*, 113–121.
- [4] G. M. Joselin Herbert, S. Iniyar, E. Sreevalsan, S. Rajapandian, *Renewable and Sustainable Energy Reviews* **2007**, *11*, 1117–1145.
- [5] P. McKendry, *Bioresource Technology* **2002**, *83*, 37–46.
- [6] E. Barbier, *Renewable and Sustainable Energy Reviews* **2002**, *6*, 3–65.
- [7] C. J. Chen, *Physics of Solar Energy*, John Wiley & Sons, Hoboken, **2011**.
- [8] A. Goetzberger, C. Hebling, *Solar Energy Materials and Solar Cells* **2000**, *62*, 1–19.
- [9] Best Research-Cell Efficiencies, *National Renewable Energy Laboratory*, <http://www.nrel.gov/ncpv/images/efficiency_chart.jpg> Accessed 8/19/2013.
- [10] R. M. Swanson, *Progress in Photovoltaics: Research and Applications* **2006**, *14*, 443–453.
- [11] J. L. Sawin, E. Martinot, D. Barnes, A. McCrone, J. Roussell, R. Sims, Sonn, V. Tag-O'Brien, *Renewables 2011 Global Status Report*, Renewable Energy Policy Network for the 21st Century, **2011**.
- [12] A. Shah, P. Torres, R. Tscharnner, N. Wyrsh, H. Keppner, *Science* **1999**, *285*, 692–698.
- [13] G. Li, V. Shrotriya, J. Huang, Y. Yao, T. Moriarty, K. Emery, Y. Yang, *Nature Materials* **2005**, *4*, 864–868.
- [14] M. Jørgensen, K. Norrman, F. C. Krebs, *Solar Energy Materials and Solar Cells* **2008**, *92*, 686–714.
- [15] S. Günes, H. Neugebauer, N. S. Sariciftci, *Chemical Reviews* **2007**, *107*, 1324–1338.
- [16] Y. Liang, Z. Xu, J. Xia, S.-T. Tsai, Y. Wu, G. Li, C. Ray, L. Yu, *Advanced*

- Materials* **2010**, *22*, 135–138.
- [17] Heliatek GmbH, *Heliatek Webiste*, **2012**.
- [18] J. Burschka, N. Pellet, S.-J. Moon, R. Humphry-Baker, P. Gao, M. K. Nazeeruddin, M. Grätzel, *Nature* **2013**, *499*, 316–319.
- [19] B. O'Regan, M. Grätzel, *Nature* **1991**, *353*, 737–740.
- [20] M. Grätzel, *Journal of Photochemistry and Photobiology A: Chemistry* **2004**, *164*, 3–14.
- [21] G. Boschloo, A. Hagfeldt, *Accounts of Chemical Research* **2009**, *42*, 1819–1826.
- [22] A. Hagfeldt, M. Grätzel, *Accounts of Chemical Research* **2000**, *33*, 269–277.
- [23] V. M. Fthenakis, H. C. Kim, E. Alsema, *Environmental Science & Technology* **2008**, *42*, 2168–2174.
- [24] G. D. Barber, P. G. Hoertz, S.-H. A. Lee, N. M. Abrams, J. Mikulca, T. E. Mallouk, P. Liska, S. M. Zakeeruddin, M. Grätzel, A. Ho-Baillie, M. A. Green, *The Journal of Physical Chemistry Letters* **2011**, *2*, 581–585.
- [25] S. Y. Huang, G. Schlichthorl, A. J. Nozik, M. Grätzel, A. J. Frank, *The Journal of Physical Chemistry B* **1997**, *101*, 2576–2582.
- [26] F. Cao, G. Oskam, G. J. Meyer, P. C. Searson, *The Journal of Physical Chemistry* **1996**, *100*, 17021–17027.
- [27] K. Zhu, N. R. Neale, A. Miedaner, A. J. Frank, *Nano Letters* **2007**, *7*, 69–74.
- [28] M. Grätzel, *Journal of Photochemistry and Photobiology C: Photochemistry Reviews* **2003**, *4*, 145–153.
- [29] M. Law, L. E. Greene, J. C. Johnson, R. Saykally, P. Yang, *Nature Materials* **2005**, *4*, 455–459.
- [30] G. K. Mor, K. Shankar, M. Paulose, O. K. Varghese, C. A. Grimes, *Nano Letters* **2006**, *6*, 215–218.
- [31] M. Adachi, Y. Murata, J. Takao, J. Jiu, M. Sakamoto, F. Wang, *Journal of the American Chemical Society* **2004**, *126*, 14943–14949.
- [32] R. Katoh, A. Furube, T. Yoshihara, K. Hara, G. Fujihashi, S. Takano, S. Murata, H. Arakawa, M. Tachiya, *The Journal of Physical Chemistry B* **2004**, *108*, 4818–4822.
- [33] P. Péchy, T. Renouard, S. M. Zakeeruddin, R. Humphry-Baker, P. Comte, P. Liska, L. Cevey, E. Costa, V. Shklover, L. Spiccia, G. B. Deacon, C. A.

- Bignozzi, M. Grätzel, *Journal of the American Chemical Society* **2001**, *123*, 1613–1624.
- [34] Y. Sun, A. C. Onicha, M. Myahkostupov, F. N. Castellano, *Applied Materials & Interfaces* **2010**, *2*, 2039–2045.
- [35] F. Matar, T. H. Ghaddar, K. Walley, T. DosSantos, J. R. Durrant, B. O'Regan, *Journal of Materials Chemistry* **2008**, *18*, 4246–4253.
- [36] S. Ferrere, B. A. Gregg, *Journal of the American Chemical Society* **1998**, *120*, 843–844.
- [37] A. Mishra, M. K. R. Fischer, P. Bauerle, *Angewandte Chemie* **2009**, *48*, 2474–2499.
- [38] X. Yan, X. Cui, B. Li, L.-S. Li, *Nano Letters* **2010**, *10*, 1869–1873.
- [39] A. Yella, H.-W. Lee, H. N. Tsao, C. Yi, A. K. Chandiran, M. K. Nazeeruddin, E. W.-G. Diau, C.-Y. Yeh, S. M. Zakeeruddin, M. Grätzel, *Science* **2011**, *334*, 629–634.
- [40] P. Wang, S. M. Zakeeruddin, J. E. Moser, M. Grätzel, *The Journal of Physical Chemistry B* **2003**, *107*, 13280–13285.
- [41] P. Wang, S. M. Zakeeruddin, J. E. Moser, M. K. Nazeeruddin, T. Sekiguchi, M. Grätzel, *Nature Materials* **2003**, *2*, 402–407.
- [42] S. Hore, C. Vetter, R. Kern, H. Smit, A. Hinsch, *Solar Energy Materials and Solar Cells* **2006**, *90*, 1176–1188.
- [43] M. Dürr, A. Yasuda, G. Nelles, *Applied Physics Letters* **2006**, *89*, 1–3.
- [44] V. Singh, D. Joung, L. Zhai, S. Das, S. I. Khondaker, S. Seal, *Progress in Materials Science* **2011**, *56*, 1178–1271.
- [45] F. J. Luque, J. D. Pasteris, B. Wopenka, M. Rodas, J. F. Barrenechea, *American Journal of Science* **1998**, *298*, 471–498.
- [46] A. K. Geim, K. S. Novoselov, *Nature Materials* **2007**, *6*, 183–191.
- [47] A. Weston, M. Murthy, *Carbon* **1996**, *34*, 1267–1274.
- [48] H. Dai, *Surface Science* **2002**, *500*, 218–241.
- [49] H. Fukushima, L. T. Drzal, B. P. Rook, M. J. Rich, *Journal of Thermal Analysis and Calorimetry* **2006**, *85*, 235–238.
- [50] W. Primak, L. Fuchs, *Physical Review* **1954**, *95*, 22–30.

- [51] Y. Hernandez, V. Nicolosi, M. Lotya, F. M. Blighe, Z. Sun, S. De, I. T. McGovern, B. Holland, M. Byrne, Y. K. Gun'Ko, J. J. Boland, P. Niraj, G. Duesberg, S. Krishnamurthy, R. Goodhue, J. Hutchison, V. Scardaci, A. C. Ferrari, J. N. Coleman, *Nature Nanotechnology* **2008**, *3*, 563–568.
- [52] M. J. McAllister, J.-L. Li, D. H. Adamson, H. C. Schniepp, A. A. Abdala, J. Liu, M. Herrera-Alonso, D. L. Milius, R. Car, R. K. Prud'homme, I. A. Aksay, *Chemistry of Materials* **2007**, *19*, 4396–4404.
- [53] G. Chen, W. Weng, D. Wu, C. Wu, J. Lu, P. Wang, X. Chen, *Carbon* **2004**, *42*, 753–759.
- [54] A. A. Green, M. C. Hersam, *Nano Letters* **2009**, *9*, 4031–4036.
- [55] M. Lotya, Y. Hernandez, P. J. King, R. J. Smith, V. Nicolosi, L. S. Karlsson, F. M. Blighe, S. De, Z. Wang, I. T. McGovern, G. S. Duesberg, J. N. Coleman, *Journal of the American Chemical Society* **2009**, *131*, 3611–3620.
- [56] K. Kalaitzidou, H. Fukushima, L. T. Drzal, *Carbon* **2007**, *45*, 1446–1452.
- [57] K. Zaghib, G. Nadeau, K. Kinoshita, *Journal of The Electrochemical Society* **2000**, *147*, 2110–2115.
- [58] K. Sugihara, *Physical Review B* **1983**, *28*, 2157–2165.
- [59] S. Biswas, L. T. Drzal, *Nano Letters* **2009**, *9*, 167–172.
- [60] H. Wu, L. T. Drzal, *Carbon* **2012**, *50*, 1135–1145.
- [61] J. Lu, I. Do, L. T. Drzal, R. M. Worden, I. Lee, *ACS nano* **2008**, *2*, 1825–1832.

Chapter 2

Platinum-Decorated Catalytic Electrode Fabrication

Background

Whether looking at large-scale industrial processes (such as crude oil refining [1], biomass production [2]), fine chemical processing [3], pollution mitigation [4] or next-generation energy applications [5,6], the common factor is platinum as a catalyst. It has proven to be robust and effective in a diverse array of applications, but its rarity (seven orders of magnitude lower abundance in the earth's crust than iron [7]) makes it a very expensive component, even when incorporated in only trace amounts. For this reason, methods to reduce platinum loading, while maintaining its catalytic effect are highly sought after. Chief among these is the increase in specific area of the catalyst by reducing particle size. Numerous routes have been studied to produce nano-scale particles of platinum, with uniform size. By using surfactants [8], colloidal techniques [9] or sacrificial templates [10], uniform platinum nanoparticle (PtNP) synthesis is possible. In terms of simplicity, however, rapid microwave heating is unrivalled.

Microwave Platinum Nanoparticle Synthesis

As opposed to conventional heating methods, microwave radiation of a highly polar solvent raises the temperature of the reaction medium up to 20 times faster and with greater uniformity [11]. This rapid, uniform heating provides the perfect environment for uniform nucleation, resulting in near monodisperse nanoparticle formation. Using a platinum salt as the precursor and ethylene glycol (EG) as the solvent and reducing agent, microwave heating of just a few minutes brings the system to near reflux temperatures

(~175°C) resulting in the decomposition of the EG and precipitation of nanoparticles [11,12]. Do et al. showed that this method can be used to anchor platinum nanoparticles (PtNPs) to graphene, providing a high surface area of platinum on a conductive substrate [13]. TEM observation of this “platinum-decorated” graphene, shown below in Figure 2.1, shows the uniform coverage of the platelet and discrete nature of the PtNPs.

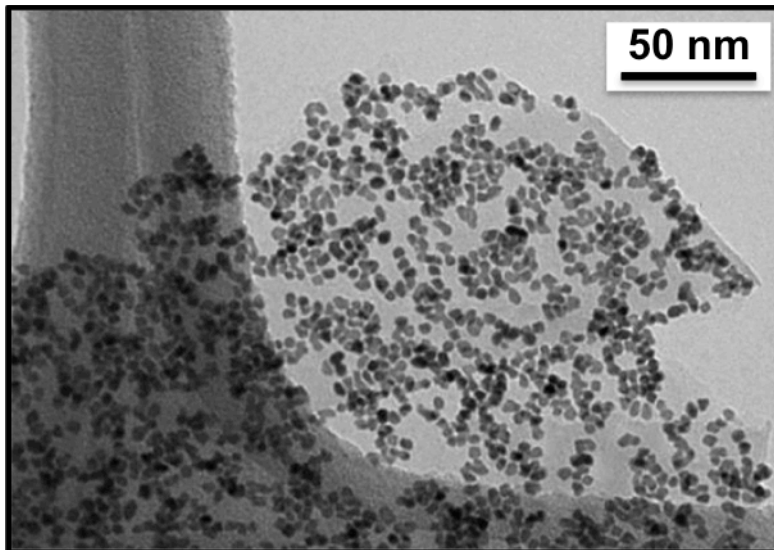


Figure 2.1: Discrete PtNPs seen on GNP, following rapid, microwave heating [13]

Using this scheme, a number of different substrates were prepared and tested for viability as counterelectrodes for DSSCs.

Thin Film Catalytic Layer

The first approach tested for counterelectrode preparation, was a combination of PtNP decoration on graphite nanoplatelets (GNP) and thin layer deposition on glass substrates. GNP can be prepared by starting with graphite-intercalated compound (GIC), a source of millimeter-scale stacks of graphene platelets that has been intercalated with sulfuric acid. Adding 100 mg of GIC to a 600 ml beaker (allowing for material

expansion) and rapidly heated by microwave irradiation (1-minute heating cycles at 1200 W) causes expansion of the GIC into a worm-like material. Within 5 min, the sample is fully expanded, yielding stacks of platelets that can be mechanically exfoliated. Images of graphite worms at the macroscopic level and magnified in an SEM are shown in Figure 2.2.

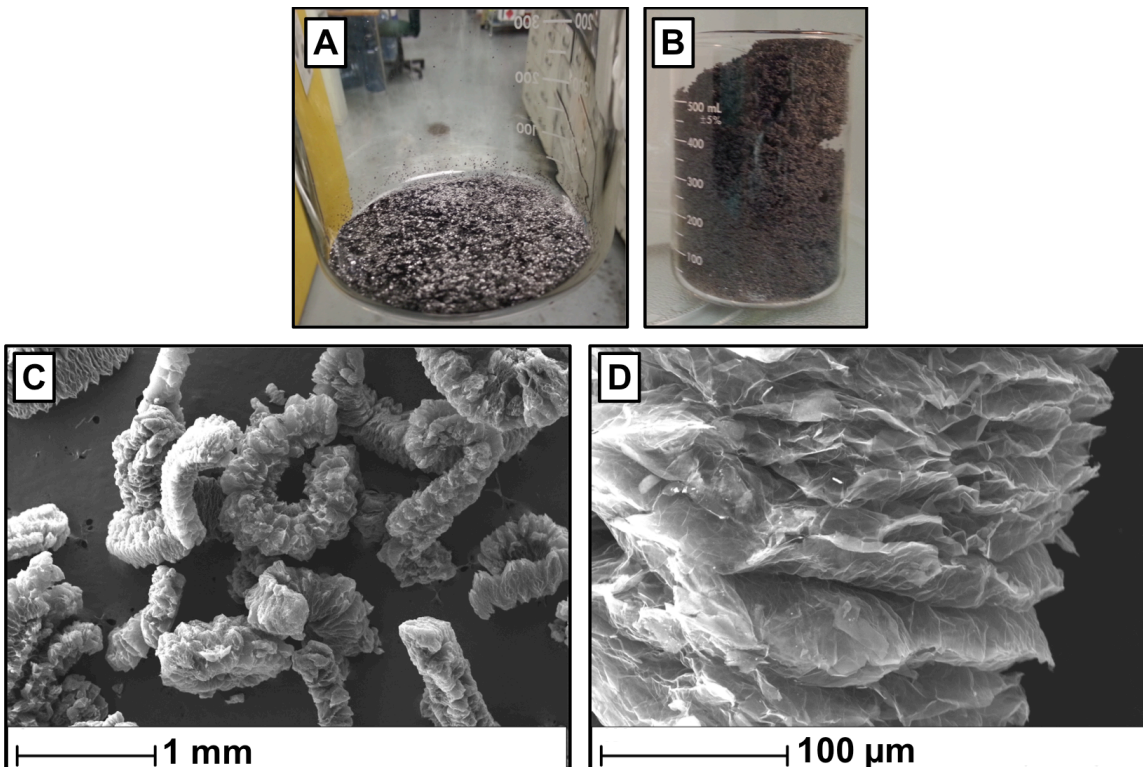


Figure 2.2: Digital images of (A) GIC prior to microwave exfoliation and (B) the highly expanded worms produced by rapid microwave heating. SEM images show (C) low magnification of the worms, showing their elongated shape and (D) higher magnification showing the pleated structure following expansion.

The expanded state of the worms makes them amenable to suspension processing. High-powered sonication (200 W with 1 in diameter horn) of the graphite worms in a suitable solvent (2-propanol, chloroform, 1-methyl-2-pyrrolidone) delaminates the material and reduces particle size, resulting in thin stacks of graphene sheets. These graphite

nanoplatelets (GNP) can be solution-processed in a number of ways, making them valuable for high-throughput, scalable applications.

For production of catalytic counterelectrodes, thin-film formation was the first attempt. By using an interfacial self-assembly process (described in detail in Chapter 4), percolated networks of GNP were deposited on a glass substrate. These electrically conductive coatings would provide the anchor for PtNP-decoration, resulting in catalytic surfaces. These films were immersed in a well containing 3 ml of 0.05 mM chloroplatinic acid hexahydrate (CPA) in EG and heated in 30 second pulses in the microwave (Kenmore Model 721.79202010 - 1200 W irradiation). Quenching and washing in reverse osmosis (RO) water, following by drying in ambient conditions and then under 25 inHg vacuum, provided surfaces that were coated evenly with PtNPs and free of residual solvent and unreacted platinum precursor. Observation of these surfaces by field emission scanning electron microscope (FESEM), showed clearly the presence of PtNPs (small, bright dots on the dark GNP substrate). A sample area can be seen below in Figure 2.3.

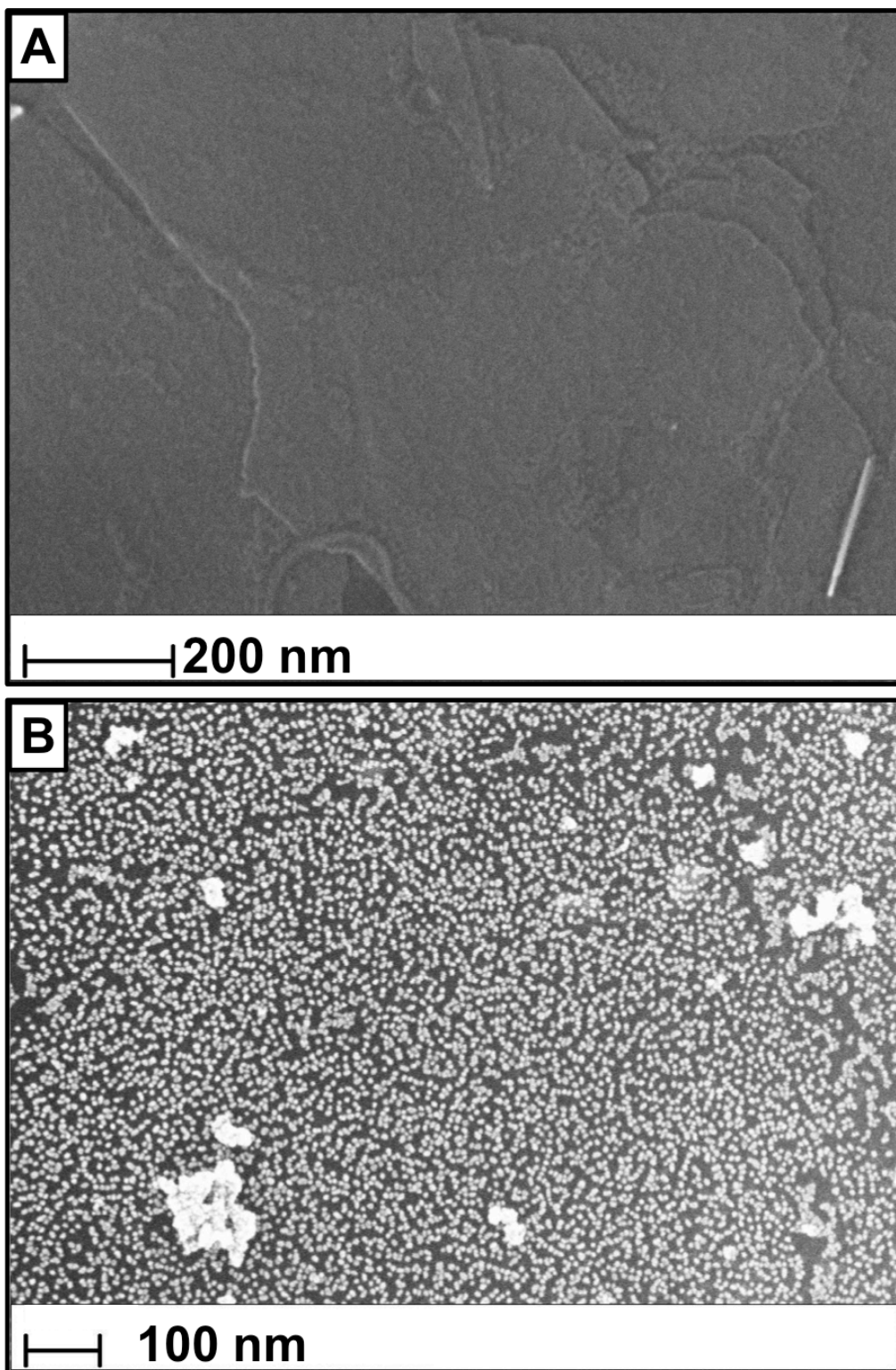


Figure 2.3: FESEM image of (A) control GNP samples without PtNP synthesis treatment and (B) PtNP-decorated GNP particle. With the exception of occasional aggregates, uniform size and coverage of PtNPs is observed.

As opposed to the work of Do, et al., it was found that uniform PtNP decoration could be achieved without the use of surfactant. However, macroscopic observation of these samples showed disruption of the continuous GNP coating, causing a loss of electrical percolation and a substantial drop in electrical conductivity (from $40 \Omega/\square$ to over $900 \Omega/\square$). Evidence of this film disruption can be seen in Figure 2.4.

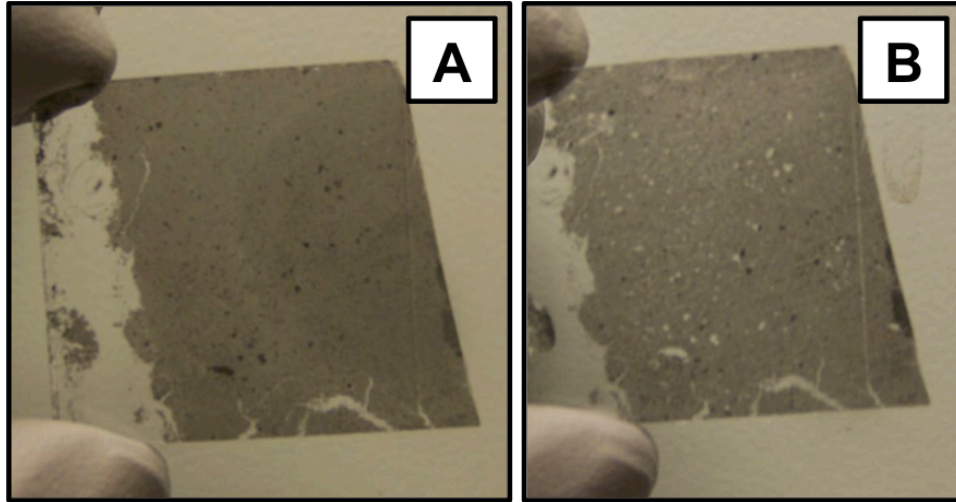


Figure 2.4: Film delamination leading resulting form rapid heating in polar solvent. Stable GNP film (A) prior to microwave heating and (B) after microwave heating

To alleviate the problems due to heating GNP layers with limited adhesion to the glass substrate, PtNP-decoration of GNP was attempted prior to film deposition as well. By heating 50 mg GNP in 50 ml EG for 60 seconds at 1200 W, followed by extensive washing with RO water, then acetone and isolation by centrifugation (5000 rpm for 30 min, repeated three times), PtNP-decorated GNP powder could be characterized and used for subsequent thin film deposition. Both TEM and FESEM confirmed the presence of extensive numbers of PtNPs on the surface (see Figure 2.5).

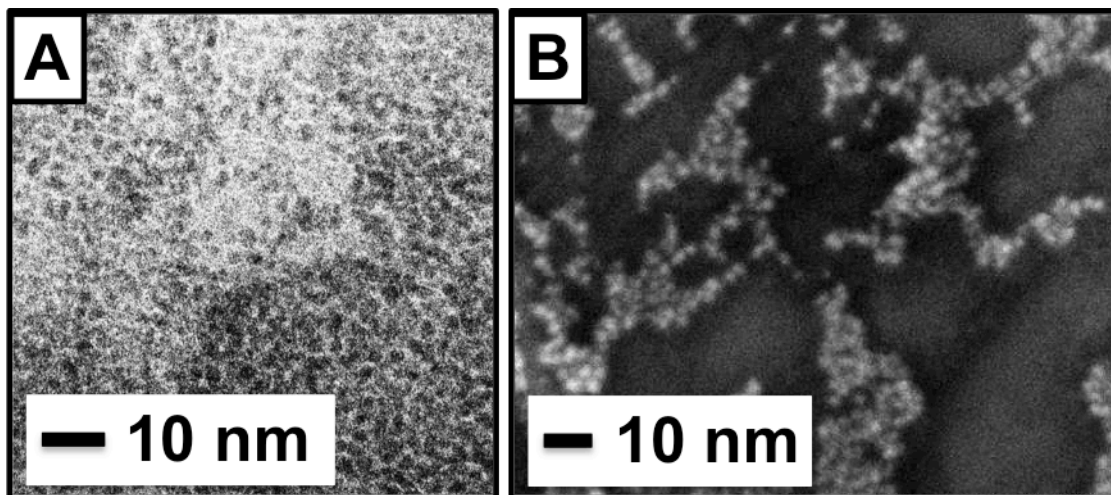


Figure 2.5: TEM and FESEM observation of PtNPs on GNP powder after rapid, microwave synthesis, washing and centrifugation (scalebars at 5 nm and 10 nm respectively)

Using this powder for subsequent dispersion in chloroform and interfacial self-assembly, thin films were deposited on glass substrates, providing continuous layers capable of being made into counterelectrodes for DSSCs. Figure 2.6 shows the GNP/PtNP coatings on glass substrates.

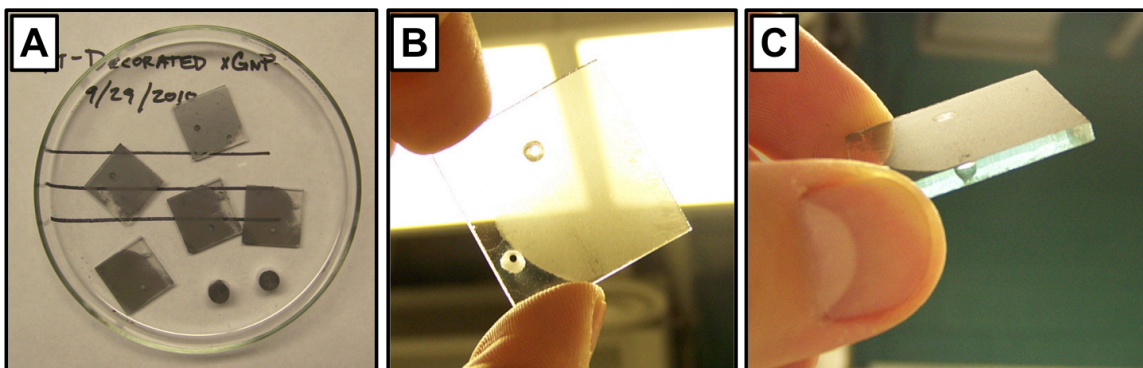


Figure 2.6: Continuous PtNP-decorated GNP coatings on glass substrates seen on (A) white background, (B) back-lit and (C) tilted to show minimal topology of film.

Though these coatings showed great potential for catalytic substrates, they proved to be susceptible to surface abrasion and delamination in the presence of polar solvents. The

search for more robust and highly electrical conductive counterelectrode material led to a different fabrication scheme entirely.

Platinum-Decorated GNP Paper

Based on the work of Wu et al. [14], an alternative method for catalytic electrode fabrication was examined. The downfall of thin films of GNP on glass substrates was stability. A process of assembling GNP into papers, by filtration and compression, would allow for improved mechanical stability compared to thin films, as well as providing improved electrical conductivity.

Again, GIC was taken as the starting material and exfoliated with rapid microwave heating (100 mg GIC sample size heated 5 min at 1200 W in 1 min cycles). Worms were then dispersed in an aqueous environment with a polycationic species (branched polyethyleneimine – PEI). Keeping a 1000:1:1 ratio of RO water:GNP:PEI, batches of up to 1L were prepared by ultrasonication at high power (200 W). Rigorous stirring for an additional 12 hours ensured full coating of the newly-exposed GNP surface with PEI surfactant, maximizing the stability of the suspension.

Following stirring, 50 ml aliquots were filtered through a porous, polar medium (Durapore DVPP filter paper – 0.67 μm pore size) to rapidly precipitate the GNP, creating highly-aligned papers of near-uniform thickness. Drying in ambient conditions (up to 12 hours) and under vacuum (2 hour, -25 inHg) removed enough water to allow platelet percolation, resulting in a self-supporting film that could be removed from the filter media. A two-stage, heating process (100°C for 1 hour, followed by 340°C for 1 hour) was necessary to (a) remove residual moisture in the papers and (b) thermally decompose the remaining PEI surfactant. Following the two-stage heating, porous papers

were pressed at 7 MPa to reduce porosity between GNP particles and create as much platelet contact as possible (thereby improving mechanical stability and electrical conductivity). Figure 2.7, below, shows the appearance of GNP papers after filtration, pressing and mounting the cross-section of the sample in epoxy.

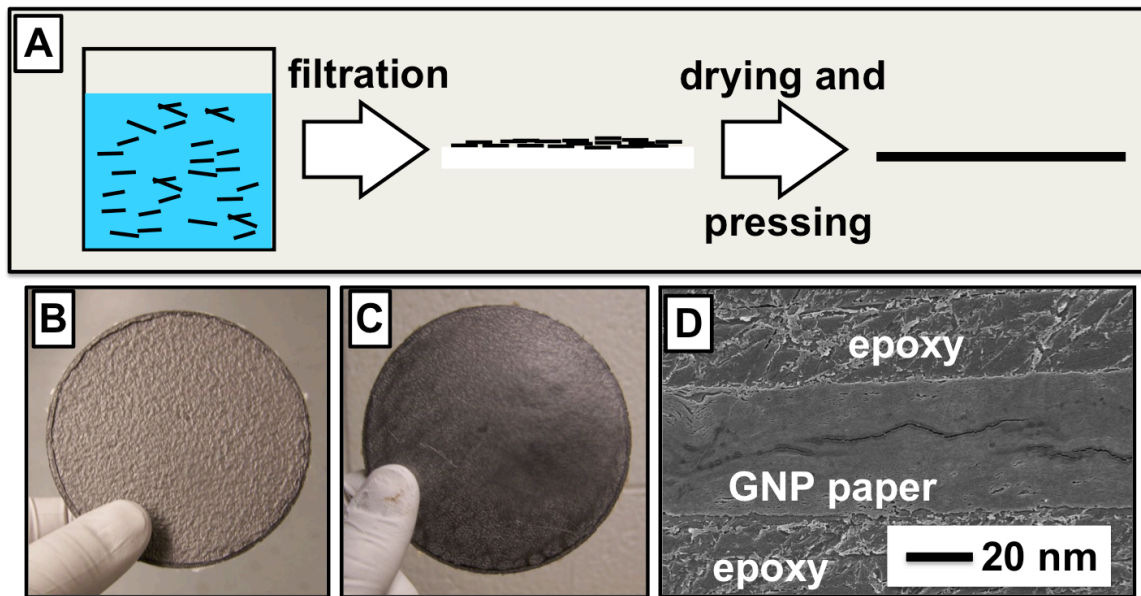


Figure 2.7: (A) Schematic for GNP paper formation and digital images (B) before and (C) after pressing and annealing. Image (D) shows a cross-sectional view of the paper embedded in epoxy, polished, gold-coated and mounted for SEM observation.

SEM imaging of the cross-section shows clearly the low porosity and uniform thickness of the film. Thermal gravimetric analysis (TGA) of these papers shows the purity and thermal stability of the papers, showing no degradation peak until the decomposition of graphite at $>500^{\circ}\text{C}$ (see Figure 2.8).

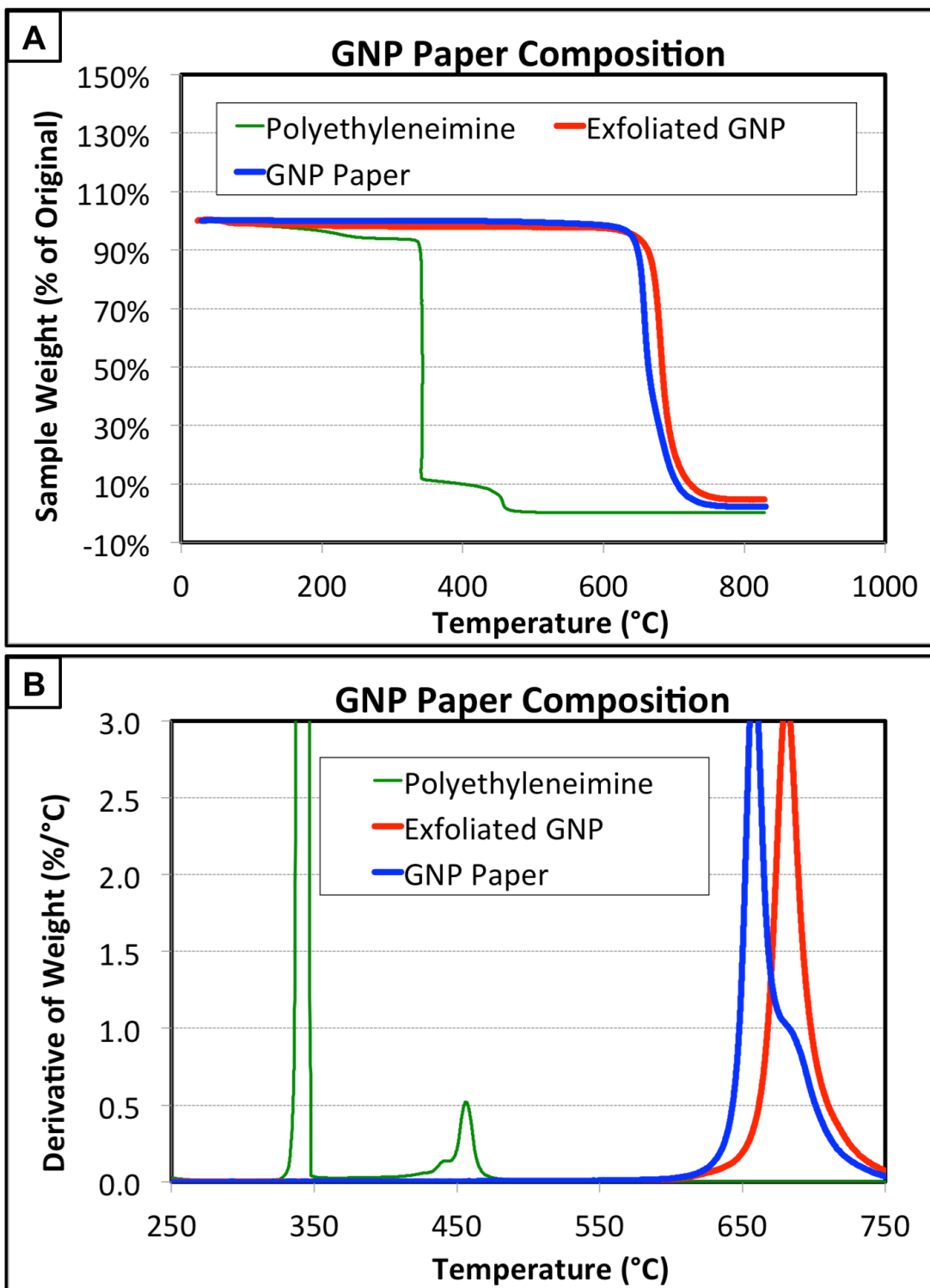


Figure 2.8: Thermogravimetric analysis of GNP paper (run at 10°C/min in air). (A) shows the negligible weight loss of the GNP paper up to the onset of graphite degradation at around 600°C and (B) shows the comparison of the derivative of weight loss percentage, notably the lack of the PEI degradation peak around 450°C, indicating high purity of the material.

The high purity of the GNP, high alignment of the platelets and limited porosity provided substrates with superlative electrical conductivity. Samples measuring 30-60 μm thick ranged from 1000-1300 S/cm (as measured by 4-point probe with a Keithley 4ZA4 Potentiostat), corresponding to a sheet resistance on the order of $0.08 \Omega/\square$.

PtNP-decoration of these surfaces was accomplished by immersion and rapid microwave heating. Much like the preparation of PtNP-decorated GNP platelets, these papers were submerged (and weighted down with a glass ring to prevent surfacing from convective currents during heating) in 40 ml EG with a predetermined loading of platinum precursor (again, CPA was chosen, at concentrations of 20 μM – 1 mM). Heating of these submerged papers for 60 seconds at 1200 W raised the temperature of the solvent to near-boiling (as evidenced by dense vapors above the solvent), causing reduction of the CPA and formation of PtNPs. Discoloration of the solvent itself suggested PtNP formation, but surface coverage on the papers was verified by FESEM (after quenching and soaking in RO water for 1-2 hours, followed by drying in ambient conditions and vacuum drying at -25 inHg). Figure 2.9, below, shows the clear presence of PtNPs on the surface of the GNP paper after heating (200 μM CPA in EG), washing and drying.

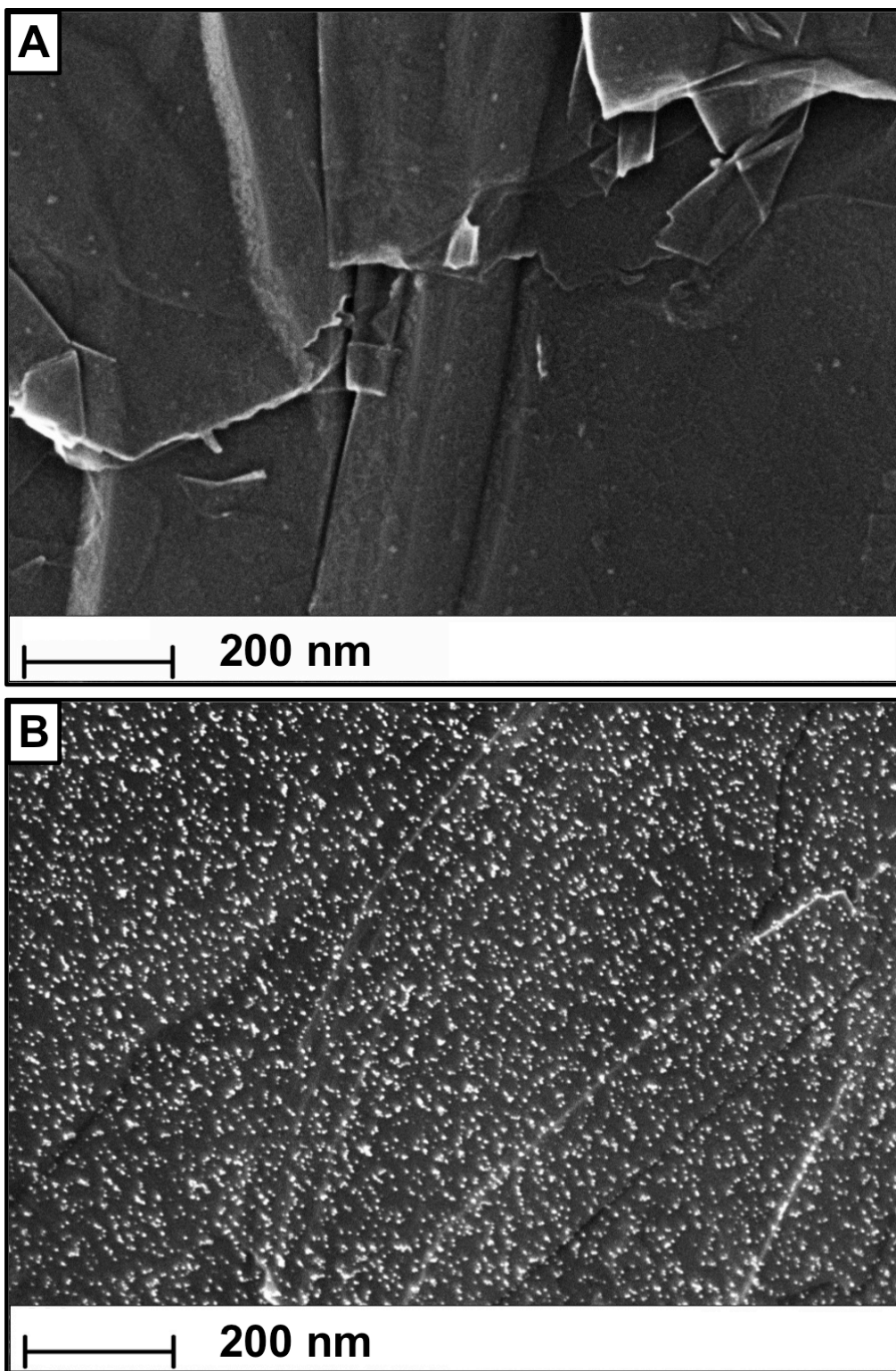


Figure 2.9: (A) Control untreated GNP paper sample in comparison to (B) GNP/PtNP paper after nanoparticle synthesis, washing and drying. Uniform coverage of discrete nanoparticles is seen, similar to thin-film GNP/PtNP samples.

The high areal density of PtNPs was promising, but mechanical stability of GNP paper for use in DSSCs was a challenge. While the papers were self-standing and maintained their integrity during sample preparation, the thin nature of the paper would allow flexing and shorting of cell if used without a rigid backing. For this reason, thin (1 mm thick) microscope glass was chosen as a rigid backing and Surlyn ionomer (a standard sealant in DSSC fabrication) was chosen as the adhesive.

Rigid GNP/PtNP substrates were constructed by laying 1 in by 1 in strips of Surlyn on microscope slides, followed by de-gassing in a vacuum oven (to remove residual moisture from the hygroscopic adhesive), followed by heating in a circulating oven to 120-130°C to render the Surlyn molten. Pieces of GNP/PtNP paper were cut to 1 in x 1 in sections with a razor and then pressed onto the molten Surlyn by hand and firm pressure was applied to minimize wrinkling and buckling of the paper. While the PtNPs are vulnerable to abrasion, it was found that using a thin (0.005" thick) poly(tetrafluoroethylene) (PTFE) film as a mask between the PtNP surface and the surface applying pressure virtually eliminated PtNP loss during processing. FESEM was used to verify PtNP presence on the surface after rigorous pressing.

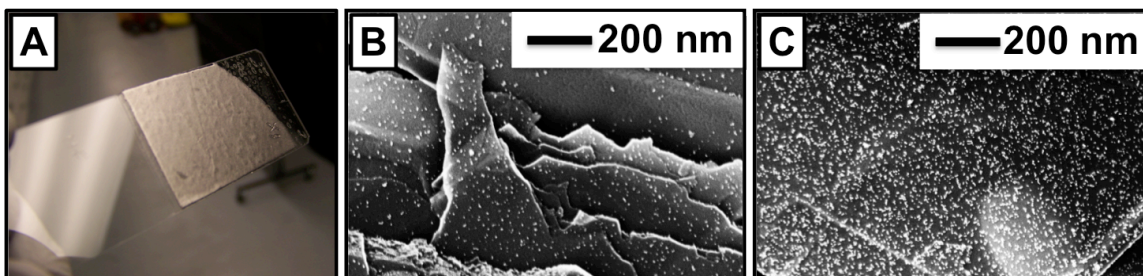


Figure 2.10: (A) GNP/Pt electrode after pressing onto molten Surlyn on glass. FESEM imaging of (B) 20 μ M and (C) 200 μ M CPA-treated samples show presence of numerous PtNPs even *after* rigorous pressing.

The presence of PtNPs on the GNP paper surface after processing opened up the possibility of adhering to any suitable backing (glass or polymer, rigid or flexible) while preserving the catalytic nature of the surface. Similar pressing without the PTFE masked resulted in drastic reduction of the PtNP coverage of the surface, suggesting the contact of the surface must be avoided or limited to low surface energy materials (such as PTFE) only.

Subsequent repetition of this process showed that the PtNP-decoration process was repeatable and consistent. Image analysis software (Image-Pro Plus by Origin) was used to count particle size on samples from future batches by observing pixel coloration. Samples histograms of heating 20 μ M solution can be seen in Figure 2.11.

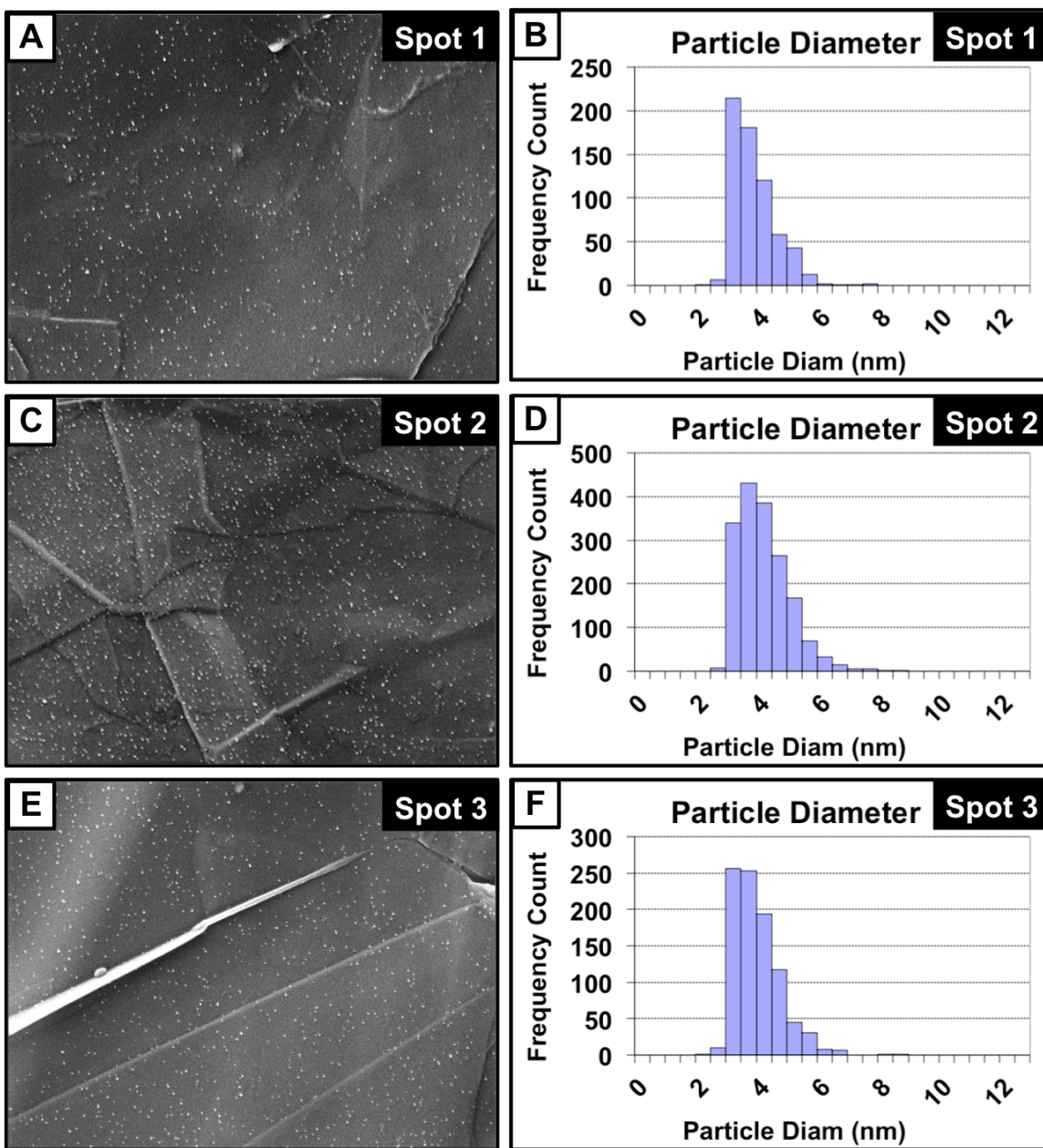


Figure 2.11: Representative images from multiple locations on 20 μM CPA-treated GNP paper. FESEM images (A, C and E) were imported to image analysis software to calculate their particle size distributions (B, D and F, respectively).

The histograms all show PtNP size to have narrow distributions and all are centered near 4 nm, confirming the consistency and repeatability of the process. By increasing the precursor concentration to 200 μM , it was found that the PtNP size distribution varied

quite little, while the overall coverage of the surface increased. Images and histograms of the 200 μM samples can be seen below in Figure 2.12.

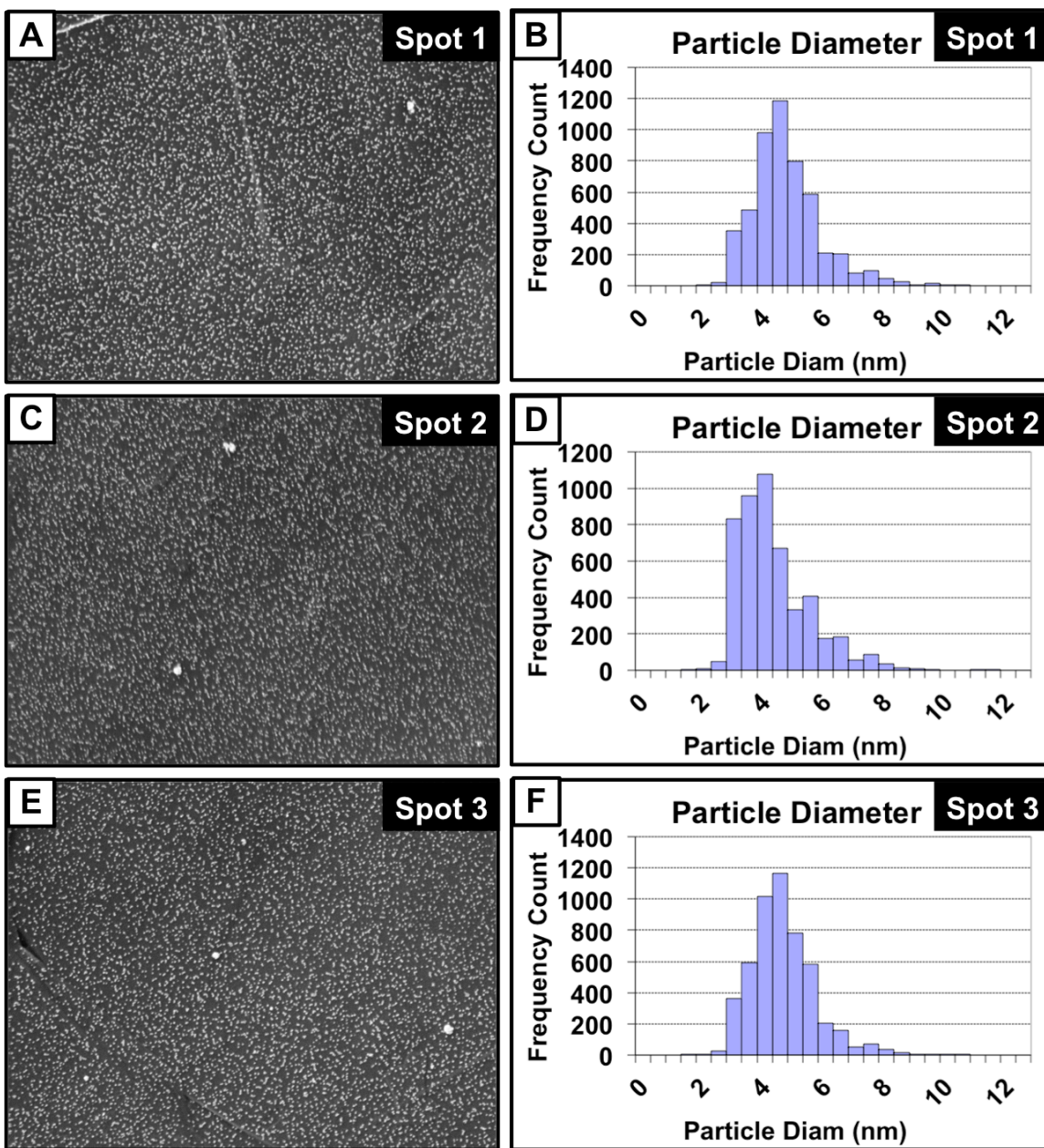


Figure 2.12: Representative images from multiple locations on 200 μM CPA-treated GNP paper. FESEM images (A, C and E) were imported to image analysis software to calculate their particle size distributions (B, D and F, respectively).

Figure 2.11 and Figure 2.12 were chosen for PtNP distribution analysis because the limited amount of GNP folds and edges provided fewer artifacts that would lead to

miscalculations by the software, but numerous other spots of the GNP/PtNP papers were imaged as well and Pt coverage appeared to be consistent throughout. The process of GNP paper fabrication and PtNP-decoration proved to be ideal for forming catalytic surfaces because of its consistency and the ability to control PtNP loading with precursor concentration.

Platinum-Decorated Composite Paper

While GNP papers provided a unique substrate for PtNP decoration, applications that demand mechanical toughness, flexibility and limited porosity (to prevent electrolyte leakage) require a different system. As Wu [15] and Jiang [16] had investigated, addition of a polymer binder and toughener to the GNP assembly greatly improved its mechanical properties. Polypropylene was chosen as a binder for this system because of (a) its low cost, (b) its low processing temperature, (c) its chemical stability in numerous common organic solvents and (d) its known effectiveness in forming composites with GNP [17].

Several methods of composite fabrication were examined (including polymer solution infiltration and melt mixing), but it was determined that the best distribution of polymer within the pores of the GNP assembly would be caused by co-filtration. Again, a GNP suspension was made by high-powered sonication (200 W for 15 min) of a 1 L suspension of water, GNP worms and PEI. The same 1000:1:1 weight ratio of water:GNP:PEI was used and again, 12 hours of vigorous stirring ensured that GNP was properly coated with surfactant and a stable suspension was formed. Next, polypropylene (PP) (Equistar-FP 809-00) was introduced to a 200 ml aliquot of the water/GNP/PEI suspension as a dry powder (20 μm particle size) and dispersed by an additional 1 minute

of high power (200 W) sonication. The amount of powder was varied, but optimum loading was found to be 1:1 with respect to the weight of graphite in suspension. Immediately after dispersing the PP powder (to prevent separation based on PP buoyancy), vacuum-assisted filtration of the water/GNP/PEI/PP suspensions through 0.67 μm pore size filter media (Durapore DVPP membrane) resulted in well-mixed sample cakes the were subsequently dried at ambient pressure (2 hr) and then under vacuum (-25 inHg, 2hr) to allow GNP percolation, aiding in removal from the filter paper. In contrast to pure GNP samples, or those with highly thermally stable polymer binders, these GNP/PP samples could not be exposed to the 340°C annealing step to remove the PEI. TGA of pure PP samples showed the onset of degradation to be just over 300°C (as seen in Figure 2.13), requiring an alternative method of removal from the graphite/polymer system.

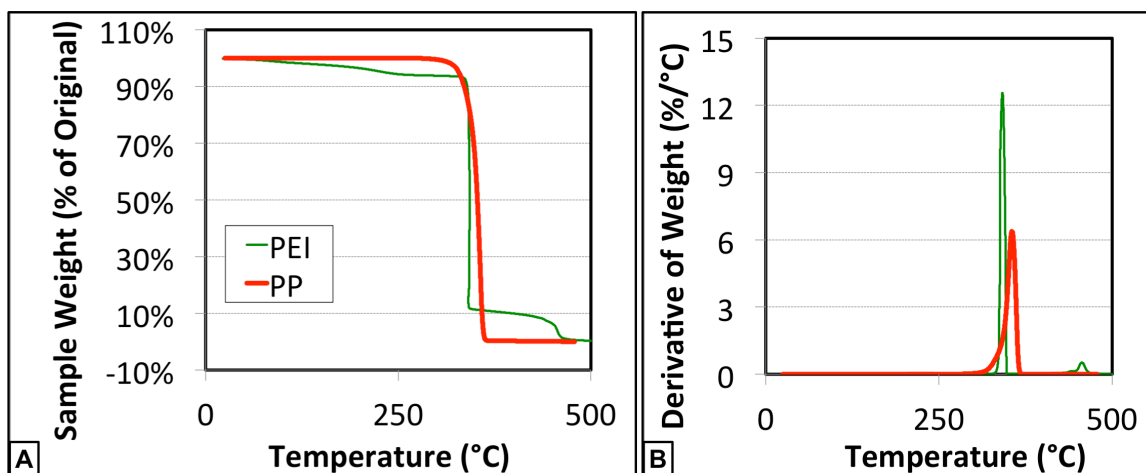


Figure 2.13: TGA analysis of pure PP degradation in air (10°C/min ramp rate)

A leaching process was developed to remove the polar, hydrophilic, PEI surfactant from the non-polar components of the system by a room-temperature water bath with extensive stirring. Figure 2.14 illustrates the use of a sandwich of porous PTFE film to hold the

porous and buoyant papers in place, allowing for penetration of water through the papers, facilitating the leeching.



Figure 2.14: Leeching process to remove PEI consisting of (A) placing dried GNP/PP papers onto a porous PTFE cloth (B) covering with a second porous PTFE cloth and (C) filling with water and stirring at room temperature for over 12 hours

Removal of these leached papers, followed again by a two stage drying process (2 hrs ambient, 2 hrs under vacuum) and TGA characterization showed them to be free of PEI consistent in composition from batch to batch. Figure 2.15 shows numerous leached and dried GNP/PP samples, each lacking the characteristic PEI decomposition peak at 340°C and all maintaining a polymer content similar to the original 50wt% loading (suggesting minimal loss during leeching).

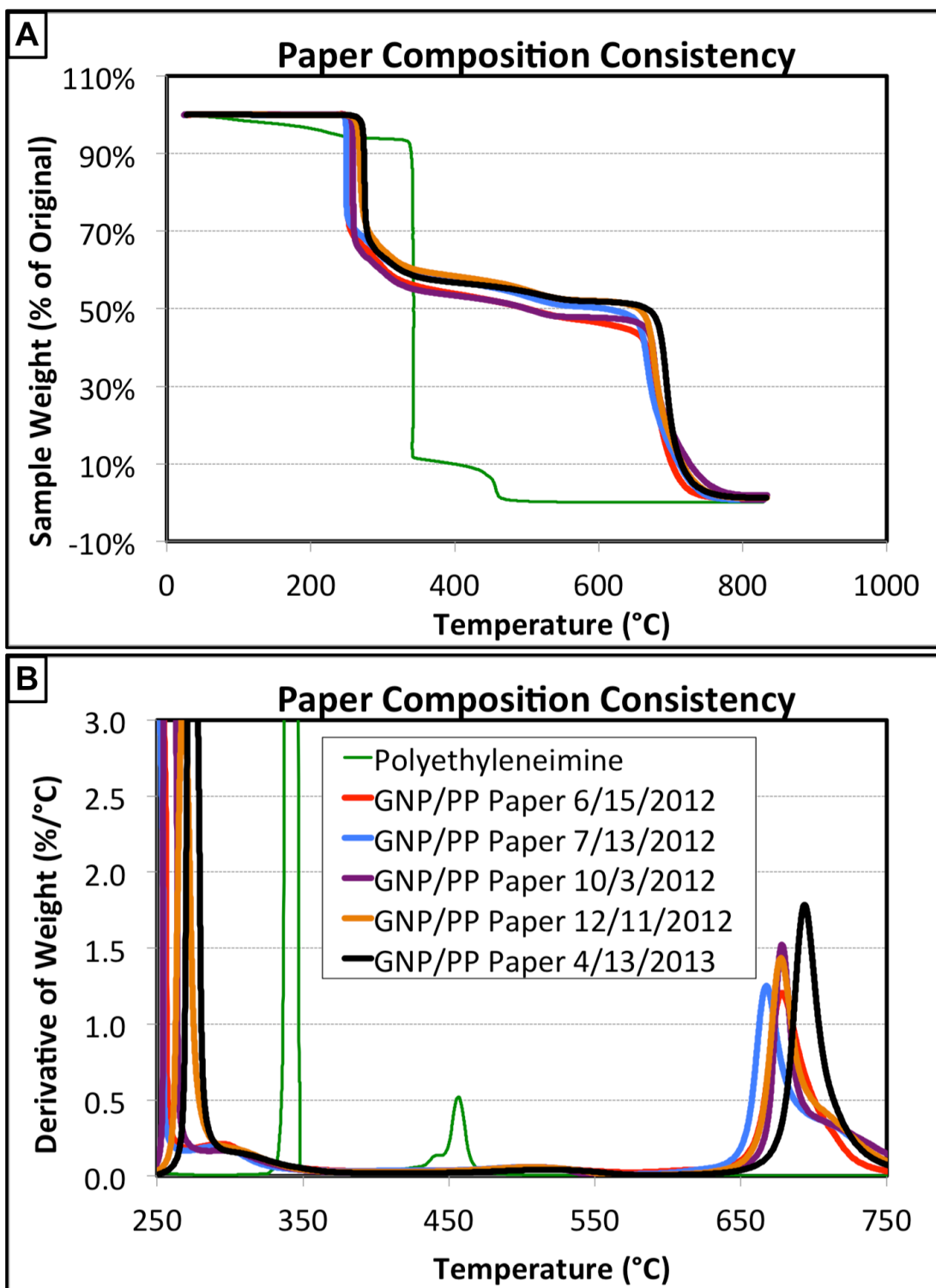


Figure 2.15: Thermogravimetric analysis of GNP/PP papers (run at 10°C/min in air). The leached papers show (A) ~50wt% mass loss at the onset of GNP degradation above 600°C. The derivative of wt% loss (B) shows a sharp peak for PEI decomposition that is seen in none of the leached papers, indicating complete removal.

These leached and dried samples were then compression molded at to allow flow of the PP into the pores between graphite platelets, eliminating porosity and acting as a binder. GNP/PP samples were placed between 125 μm thick aluminum foil in contact with the samples (chosen because of its mirror finish and for its ease of removal after molding), which was placed between polished, steel plates. This assembly was brought into contact with cold platens then heated to 180°C and held at that temperature for 10 minutes to allow equilibration of the sample at mold temperature. A 7 MPa pressure was then applied and held for 10 minutes, allowing flow of the polymer into the pores and compressing the graphite platelets into highly aligned, percolated networks. The sample was then rapidly decreased to room temperature by the flow of cooling water through the platens and then removed from the plates and the foil was peeled away.

Characterization of the electrical properties of the paper by four point probe showed that the pure GNP papers were superior, with addition of PP leading to an 88% drop in electrical conductivity. However, because the papers are thick compared to sub-micron coatings typically used in conductive glass, the papers give a sheet resistance that is still a factor of fifteen better than FTO (as seen in Figure 2.16).

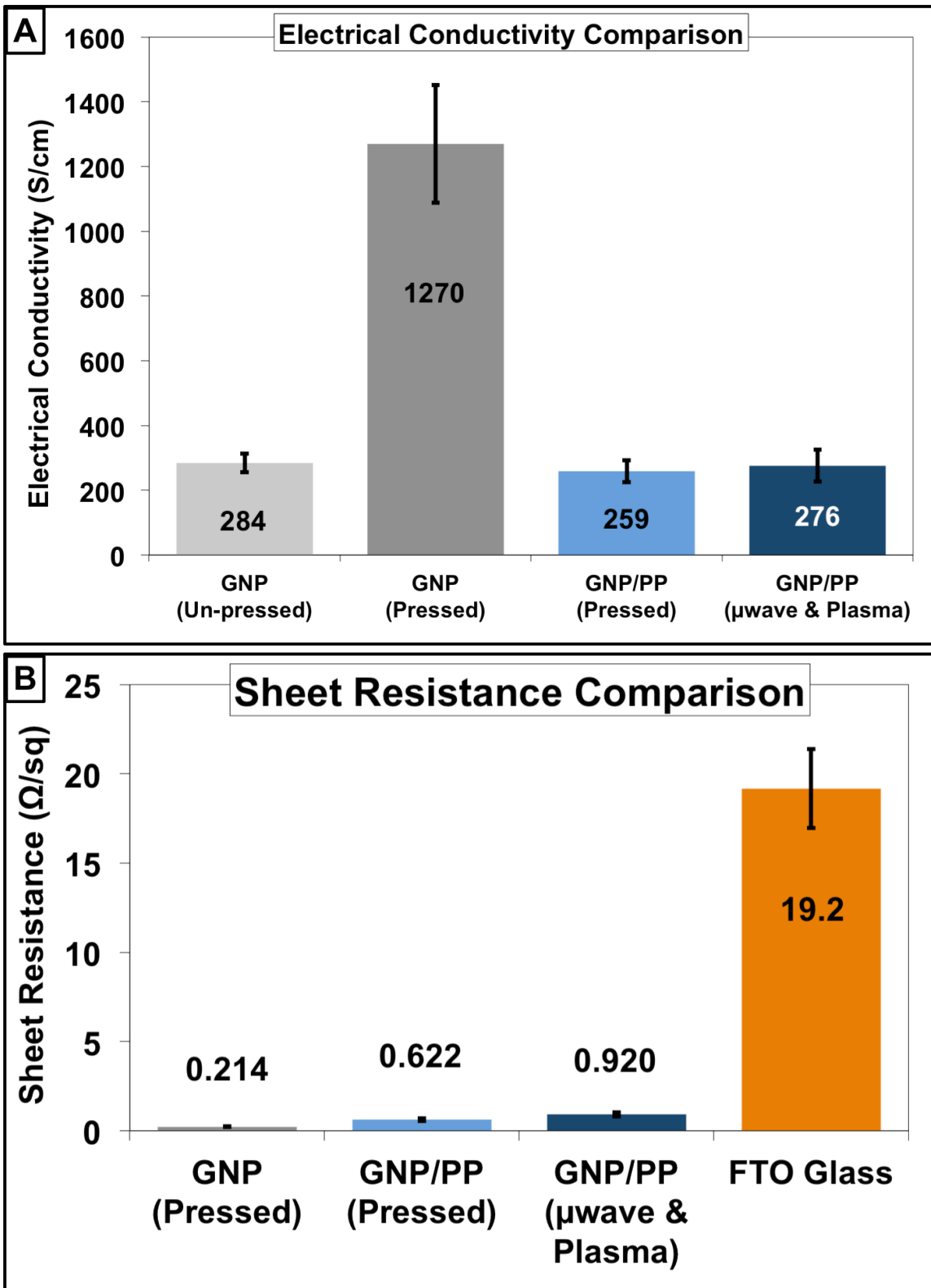


Figure 2.16: Comparison of (A) electrical conductivity and (B) sheet resistance of GNP, GNP/PP and FTO samples at various stages of processing.

However, the tradeoff for reduced electrical conductivity is greatly improved robustness. Pure GNP papers are subject to wrinkles, tears, delamination and other destructive events that can limit their application. GNP/PP papers, on the other hand, prove to be quite stable, even when curled, pressed or abraded.

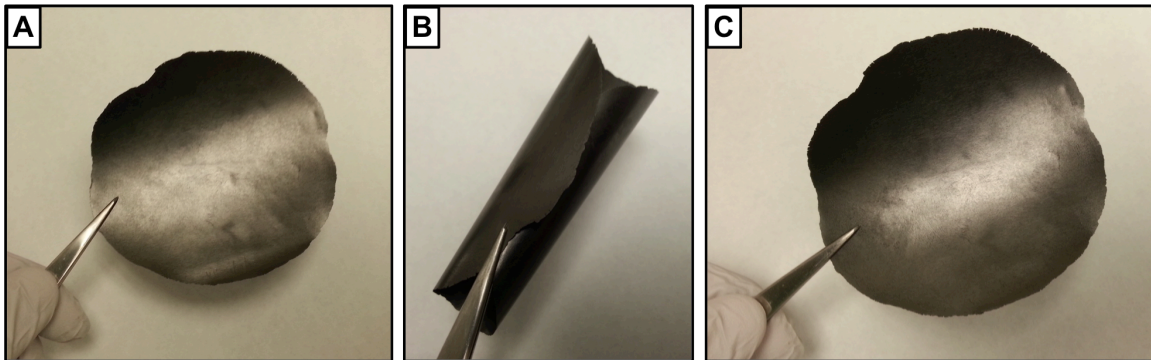


Figure 2.17: GNP/PP paper after pressing (A) showing great flexibility. Sample is able to be curled up to a small radius (B) and then uncurled (C) showing no wrinkles, creases or tears.

Additionally, specimens of the GNP/PP composite papers were cut and subjected to tensile measurements on a dynamic mechanical analyzer (TA Instruments model DMA 800). Stress-strain curves (shown in Figure 2.18) show the higher yield stress in the composite papers compared to the binder-free, pressed GNP papers. Additionally, all pure GNP papers failed well below 0.7% strain, while GNP/PP papers all exceeded 1.5% strain without failure.

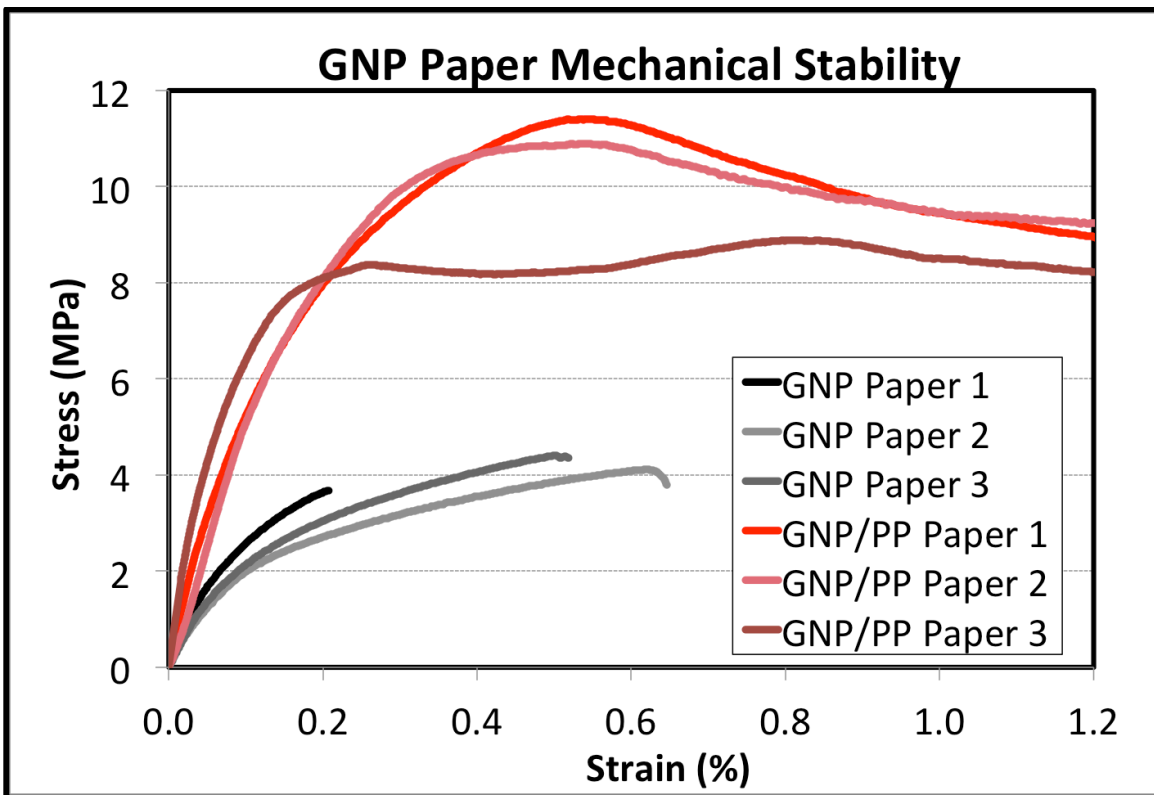


Figure 2.18: Stress-strain curves for pure GNP papers and composite papers made from 50/50wt% GNP and PP. Strain rate of 0.1%/min was used.

The improvements in the composite papers' mechanical stability resulted in better processing. Fewer samples were lost to disintegration of the GNP paper during PtNP decoration or tears and creases from pressing to a substrate.

Perhaps more important than improvements in strength and extensibility, is the negligible porosity and improved transverse stability of the GNP/PP composite papers, compared to their pure GNP counterparts. During sealing experiments, to test the feasibility of these papers in sealed cells with liquid electrolyte, pure GNP papers often leaked or suffered from delamination, causing cell failure. GNP/PP composite papers, on the other hand, performed quite well. Confirmation of pore filling was provided by cross sectional analysis. Specimens of the papers (roughly 1 cm by 1 cm) were cut, mounted in

fluorescent epoxy and polished to a mirror finish. Confocal microscopy, with laser excitation of the fluorescent dye, provides a map of voids within the papers that would provide paths for electrolyte to leak in a sealed cell. As shown in Figure 2.9, GNP/PP papers show no fluorescence within the paper, as opposed to the pure GNP counterparts.

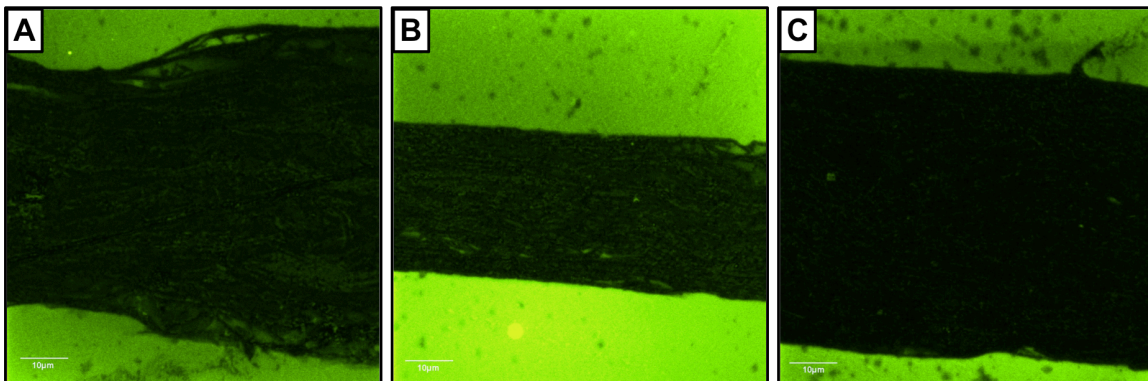


Figure 2.19: Confocal microscopy images of (A) unpressed GNP paper (B) pressed GNP paper and (C) pressed GNP/PP paper. All images taken with fluorescein isothiocyanate dye in Leco mounting epoxy (~ 0.25 $\mu\text{g/ml}$) with excitation by 488 nm Ar laser, 505 nm long-pass emission filter and U-Plan Apo 40X oil objective (NA 1.3).

Additionally, cross section specimens were oxygen plasma treated (450 W, 265 mtorr O_2) for 40 min to expose the GNP morphology. A 4 nm thick tungsten coating was sputter-coated onto the surface to render the epoxy samples conductive for imaging with FESEM. Figure 2.20 shows the high alignment of GNP platelets obtained after pressing, as well as the highly percolated network that remains in the GNP/PP sample, even with 50wt% polymer loading.

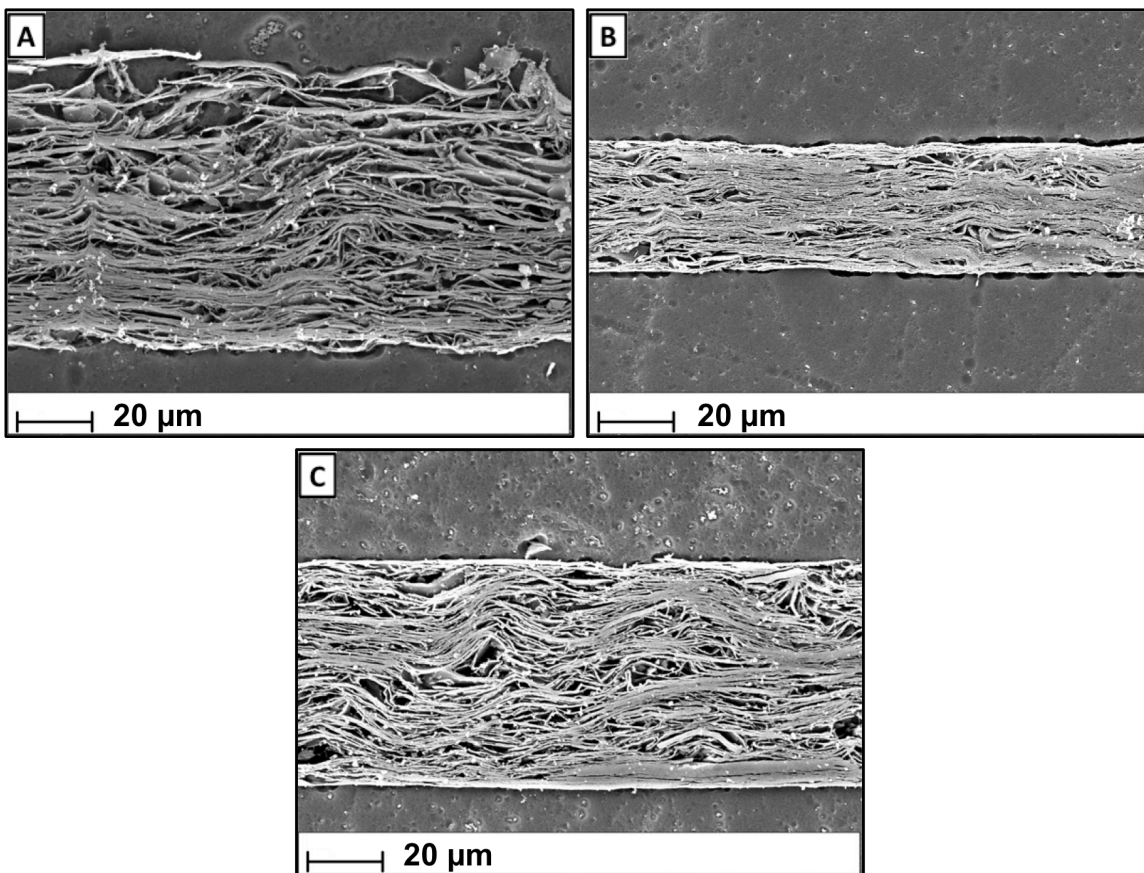


Figure 2.20: FESEM images of (A) un-pressed GNP paper (B) pressed GNP paper and (C) pressed GNP/PP paper.

Exhaustive characterization of GNP/PP papers' physical, thermal, electrical and morphological properties showed them to be valuable systems for electrode fabrication.

In order to anchor PtNPs to the surface of this GNP/PP paper, however, the surface had to be cleared of polymer to expose the graphite surface to Pt precursor in solution. To accomplish this, an oxygen plasma-treatment regime was optimized, ensuring as much exposed GNP surface as possible, without causing unnecessary damage to the platelets (which would reduce electrical conductivity and possibly disrupt formation of PtNPs on the surface. Preliminary work showed that a 450 W ionization power with a 265 mtorr O₂ environment successfully etched away PP from the surface. Treatment was

varied from 1-40 minutes and XPS was used to characterize the nature of the treated surface. The rapid spike in oxygen on the surface is ascribed to the rapid oxidation of polymer on the surface and the subsequent reduction in attribute to decomposition of the oxidized polymer leveling off to a baseline value. XPS quantification of oxygen at the surface of paper specimens can be seen below in Figure 2.21.

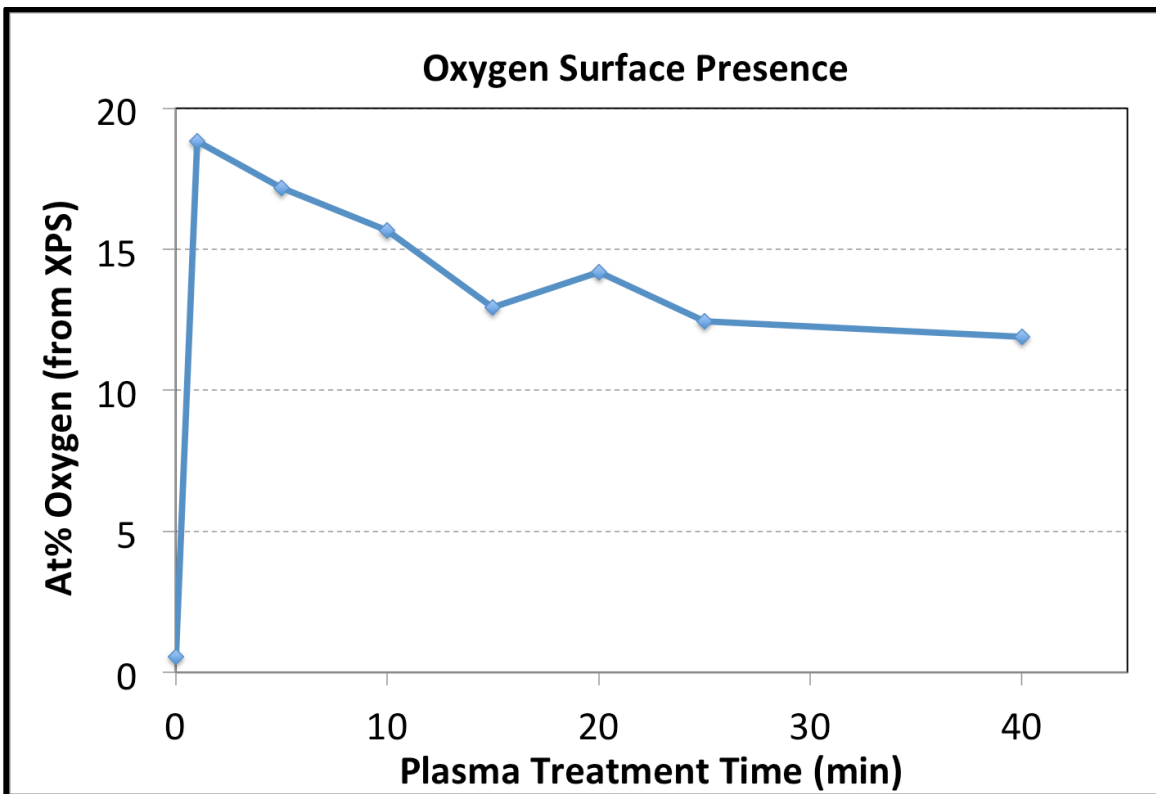


Figure 2.21: XPS characterization of oxygen plasma-treated GNP/PP paper surface.

Observation of the oxygen-plasma treated surface with FESEM shows the effect of extensive plasma treatment. While papers only exposed for short times (1-5 min) show numerous “pools” of residual polymer on the surface, those exposed to the full 40 min appear virtually free of polymer. Figure 2.22, below, shows this sequential reduction in surface polymer presence.

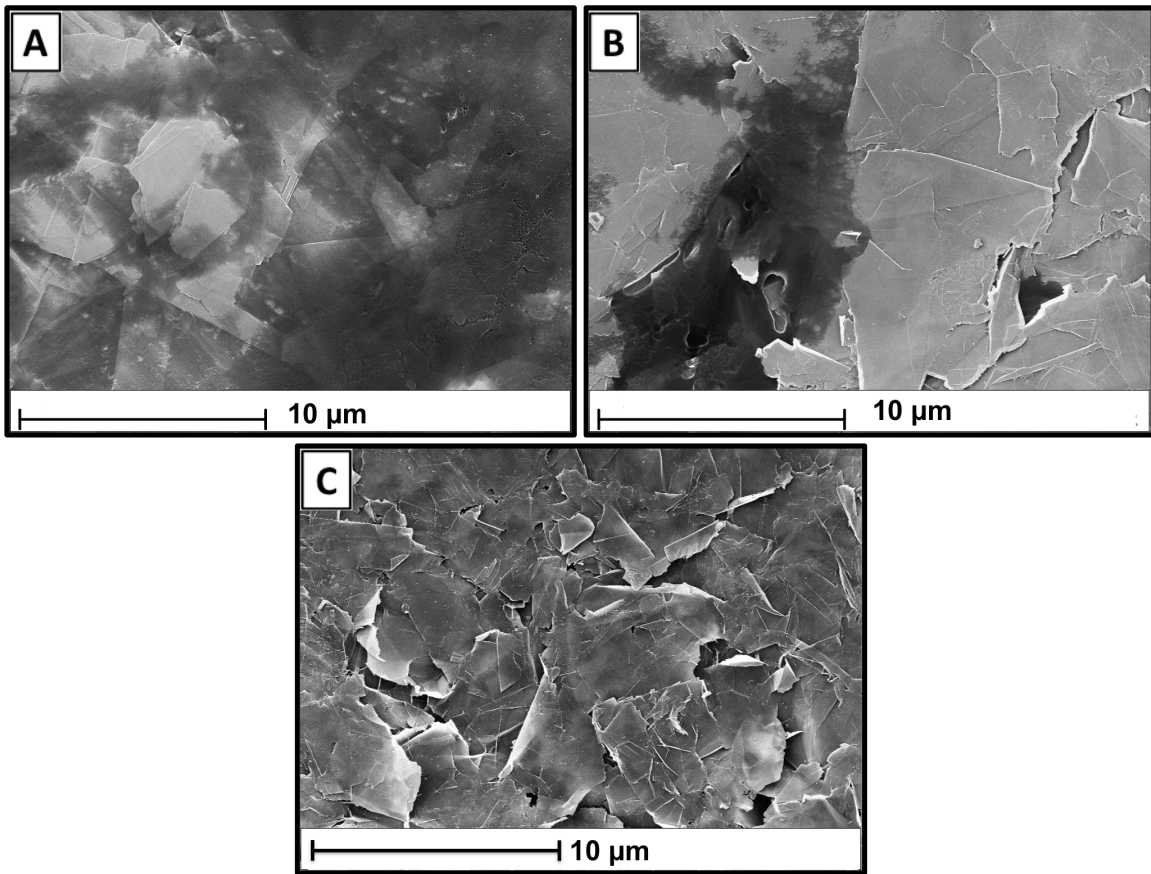


Figure 2.22: FESEM observation of GNP/PP surfaces after (A) 1 minute (B) 5 minutes and (C) 40 minutes of oxygen plasma treatment.

While the GNP platelets appeared to be generally undamaged from the plasma treatment process, few locations do show evidence of platelet deterioration. Additionally, small pools of etched polymer are visible in a small percentage of the surface as well. Figure 2.23, below, illustrates the oxidized GNP and residual polymer, which likely accounts for the increased oxygen content on the paper surface compared to untreated samples.

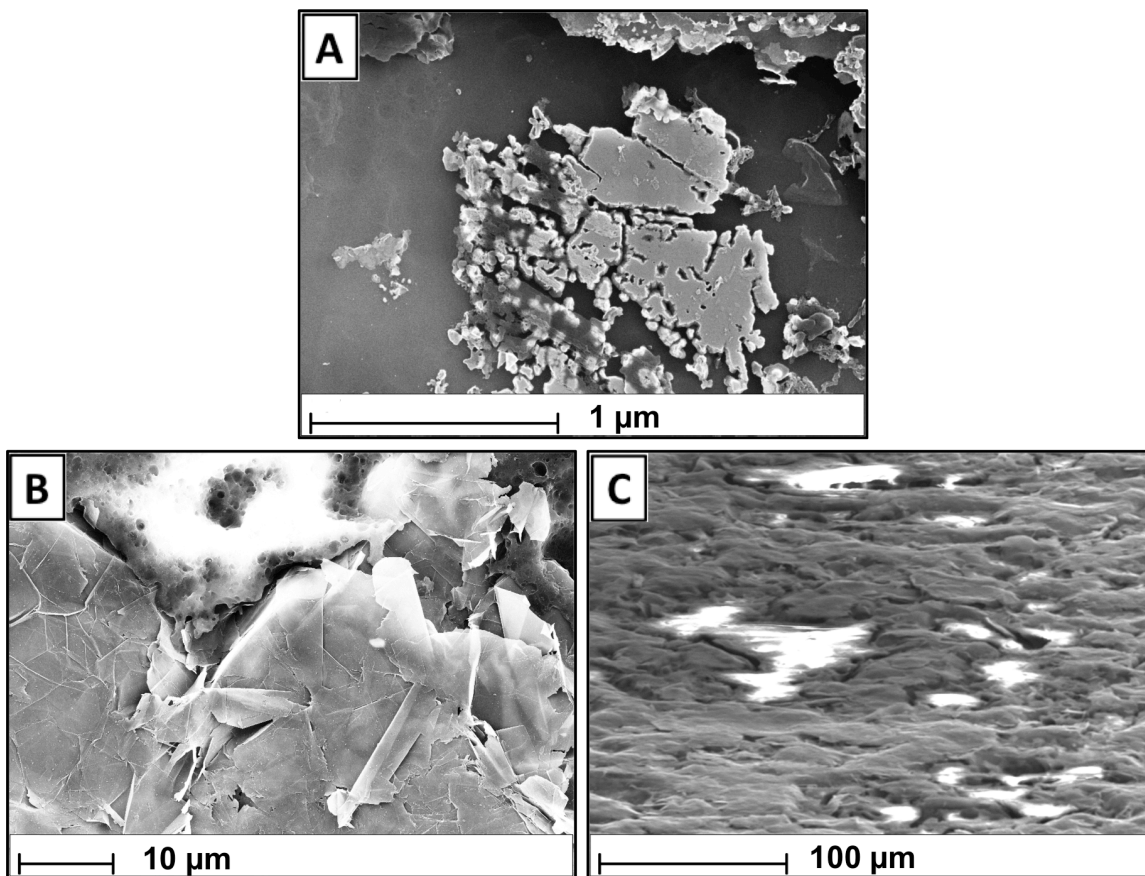


Figure 2.23: FESEM observation of GNP/PP surface after 40 min oxygen plasma treatment. Some regions show (A) noticeable degradation of GNP particles while others (B,C) show residual polymer presence pooling in depressions in the surface.

Modification of the plasma treatment by inverting papers during the etching reduced the presence of etched GNP and residual polymer on the surface, compared to standard, “face up” placement of the papers. The configuration of the papers in the plasma environment and the resulting reduction in the presence of surface artifacts can be seen in Figure 2.24.

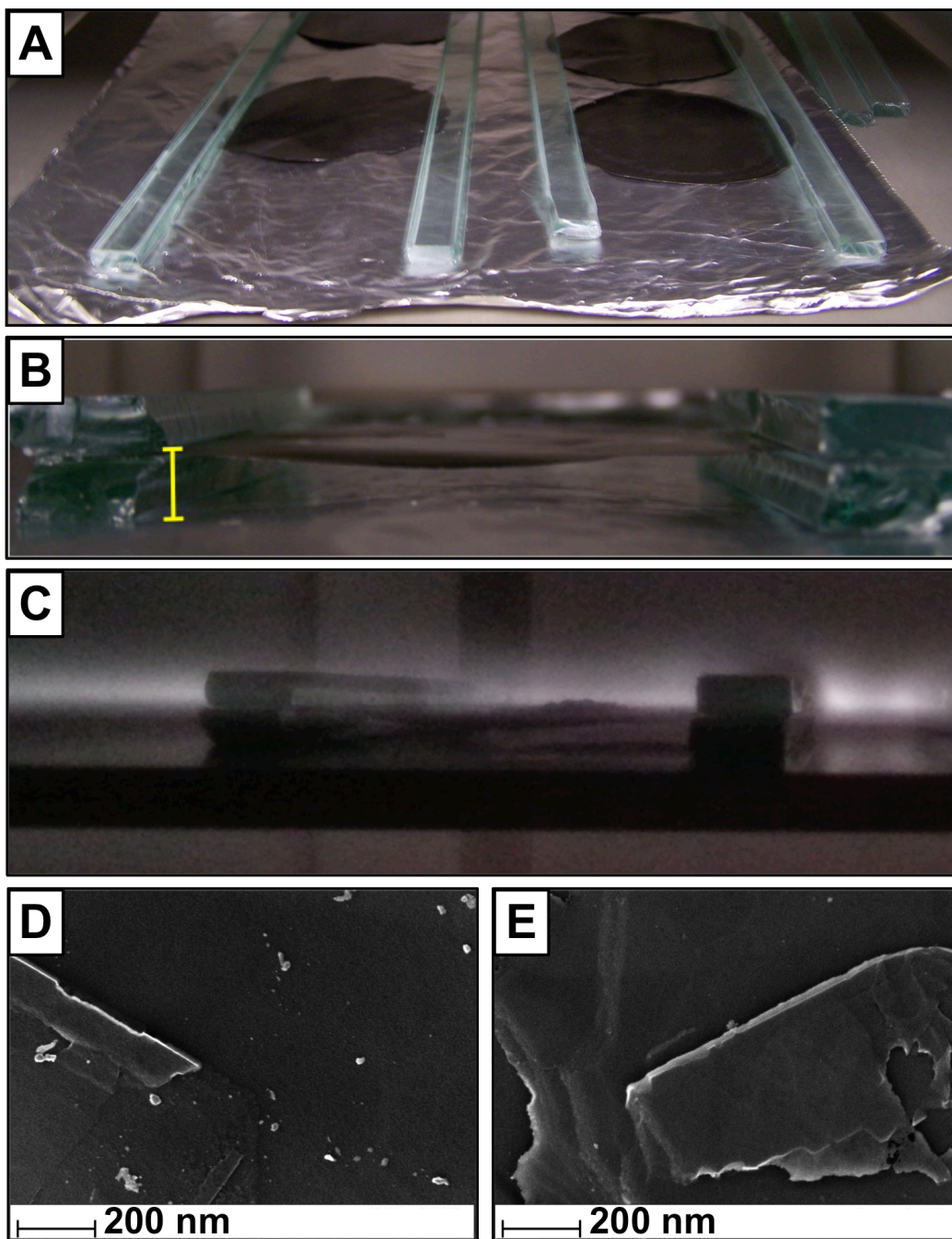


Figure 2.24: Placement of GNP/PP papers in plasma reactor in (A) standard orientation and (B) inverted orientation, 5 mm above the chamber surface. Image (C) shows inverted papers to be well within the range of the ionization of the oxygen. Image (D) is a representative region of the treated GNP/PP paper surface, showing regions that includes *small* fractions of oxidized and crumpled graphene platelets and (E) is representative of areas that are clear of oxidized species, showing a clean GNP surface for PtNP decoration.

Repeated trials of the oxygen plasma treatment showed the effect to be uniform and consistent. XPS characterization of these surfaces confirmed the same trend as those prepared in the standard, non-inverted orientation.

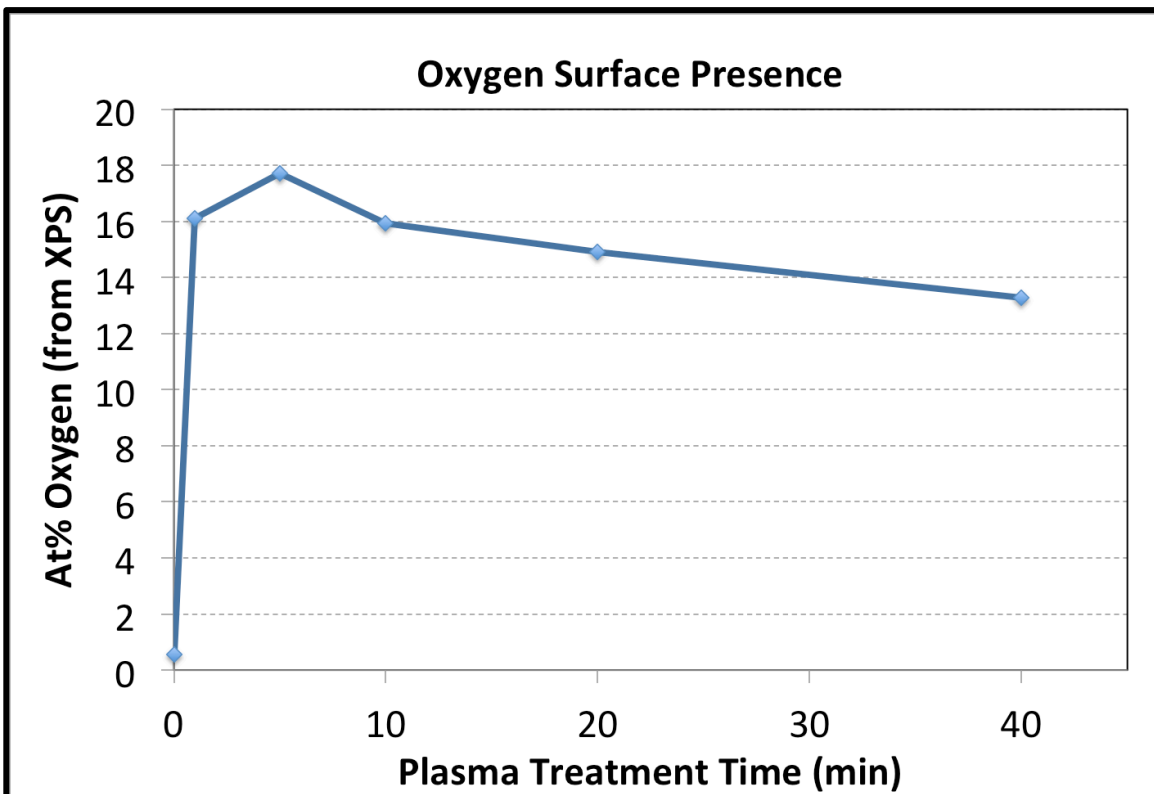


Figure 2.25: Surface presence of oxygen on GNP/PP papers as a function of plasma treatment time.

Additionally, de-convolution of the C peaks provides information on the type of carbon exposed by plasma treatment. Untreated and short (1-5 min) treated samples show minimal presence of the low-binding energy peak indicative of graphite. However, as plasma treatment time increase, this peak became quite prominent and, by 40 min, has become the predominant type of C present on the surface (compared to the higher binding energy peak indicative of sp^3 -bonded carbon).

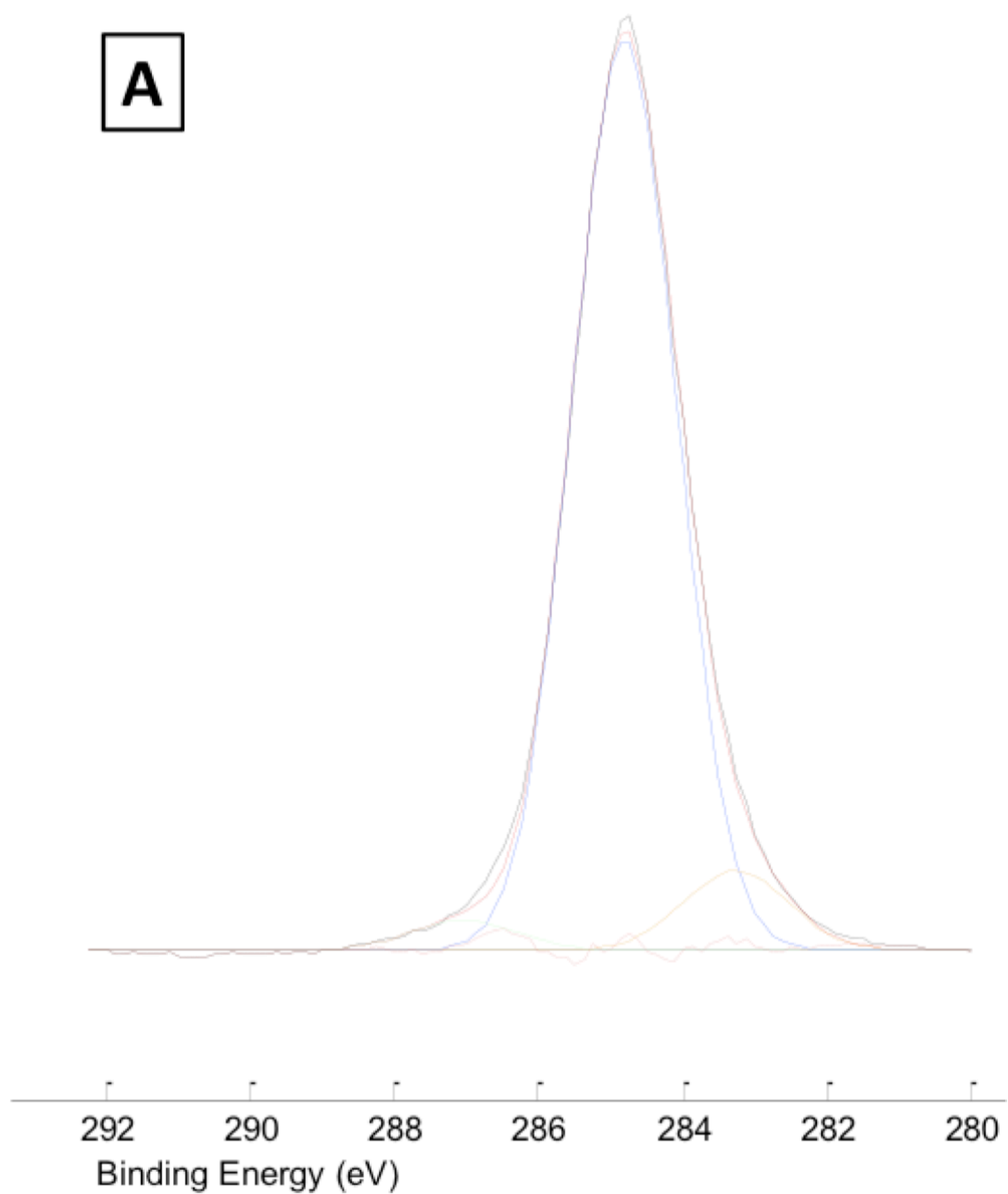


Figure 2.26: Deconvolution of the C-peak in XPS signal. Samples show an increase in the signal attributed to graphite as treatment times increase from (A) 0 min to (B) 1 min (C) 5 min (D) 10 min (E) 20 min and (F) 40 min.

Figure 2.26 (cont'd)

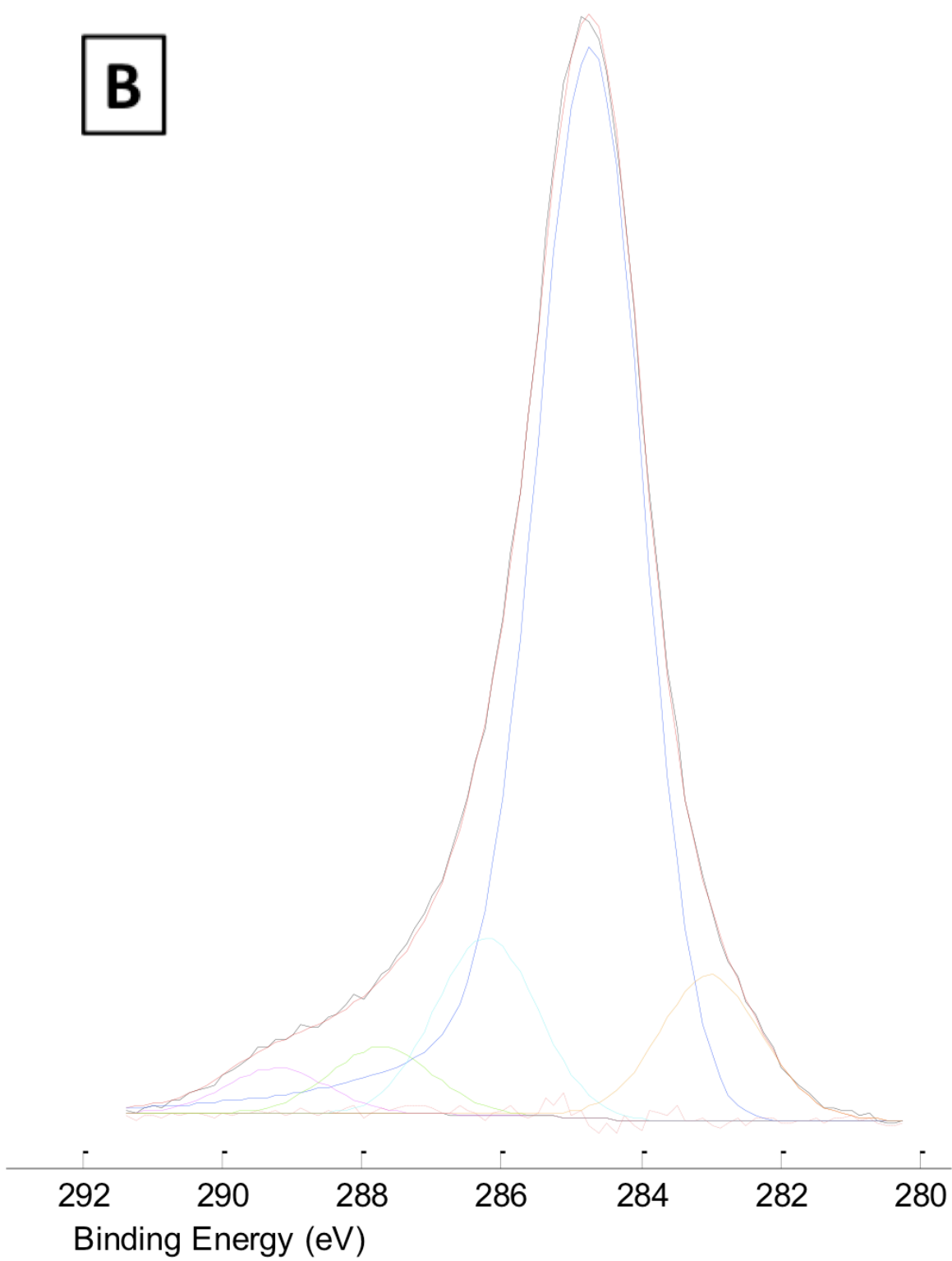


Figure 2.26 (cont'd)

C

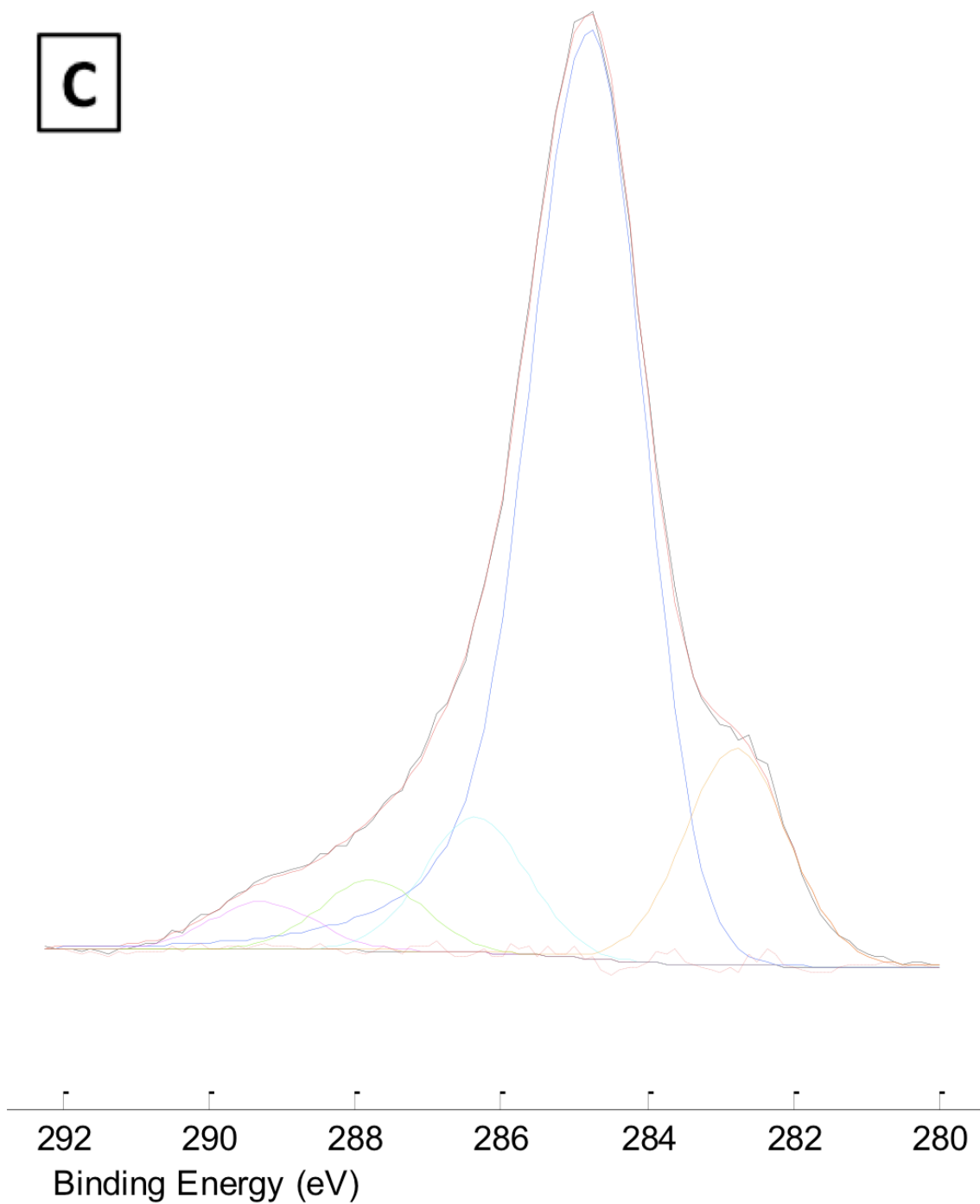


Figure 2.26 (cont'd)

D

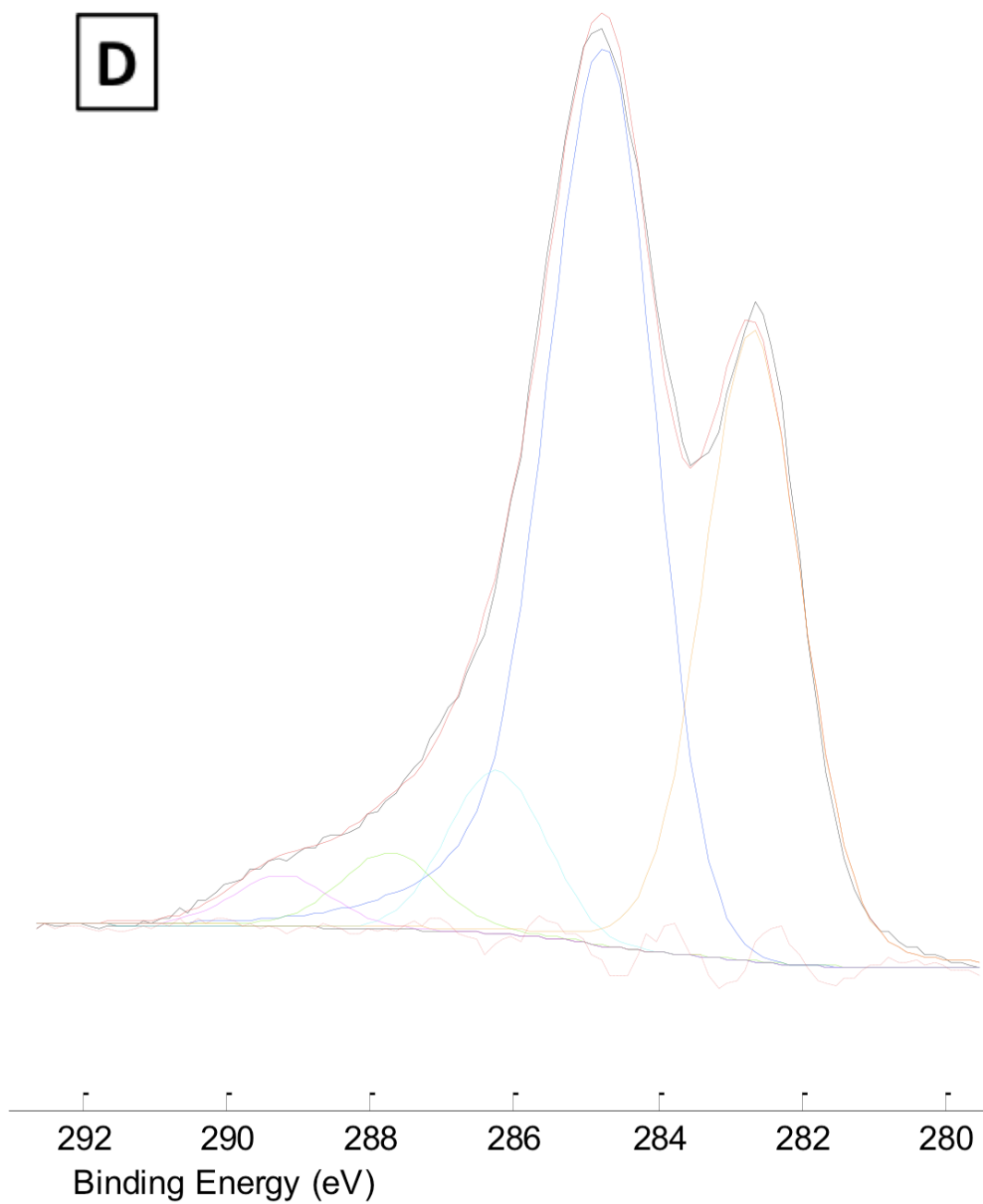


Figure 2.26 (cont'd)

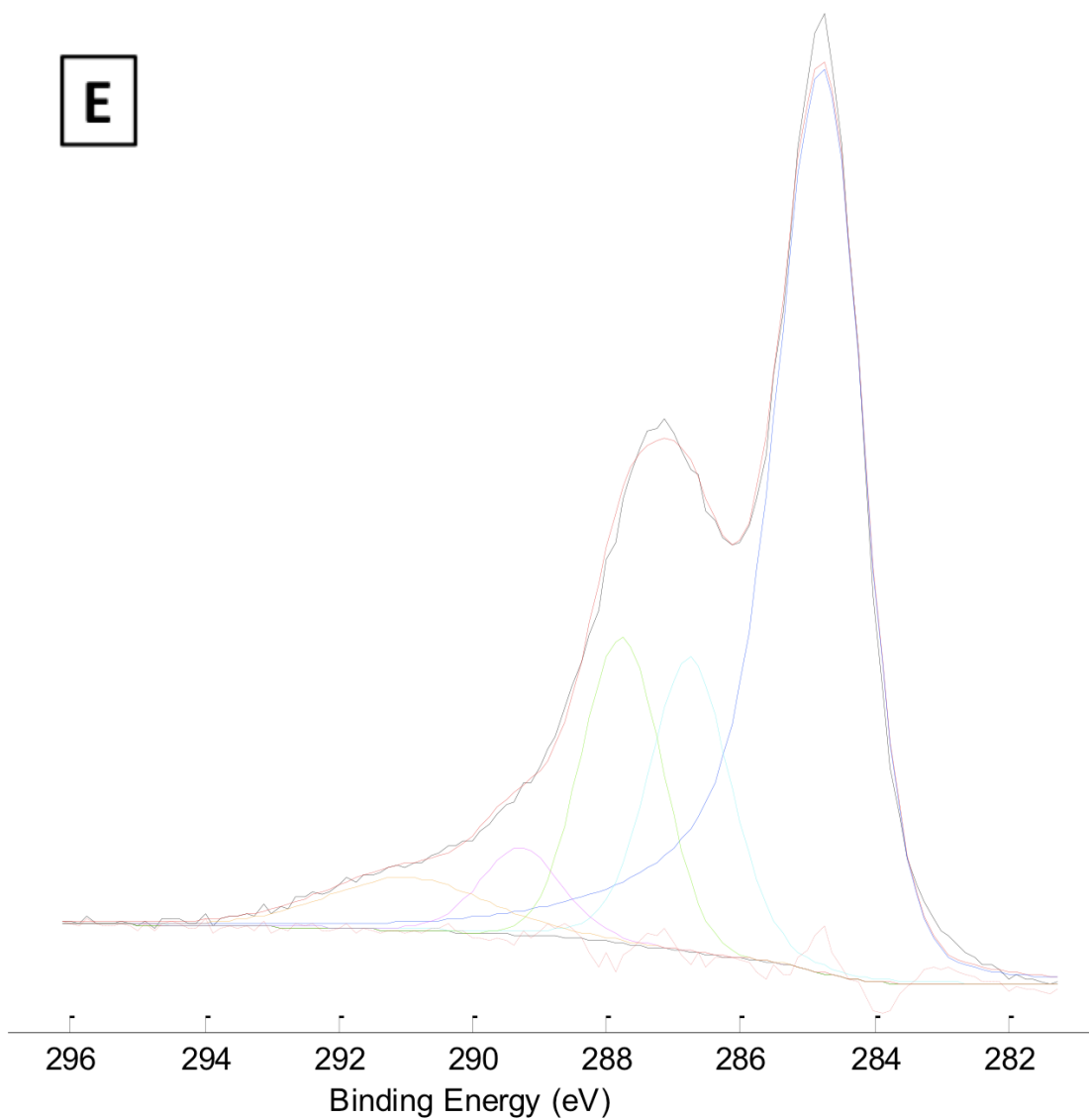
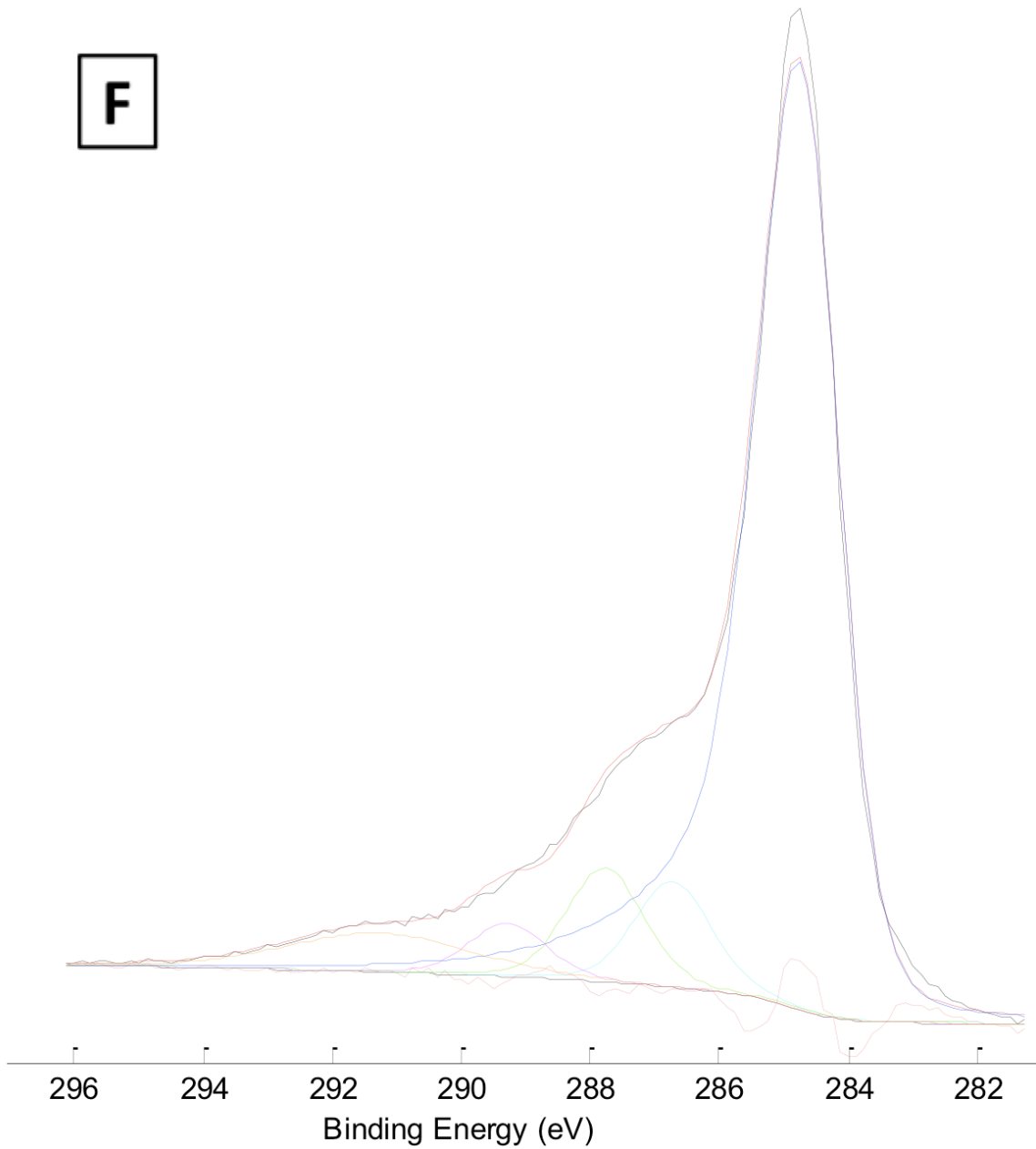


Figure 2.26 (cont'd)



When considering the full complement of information about these GNP/PP surfaces, it becomes clear that they are well-suited for use as substrates for PtNP decoration. They are electrically conductive, chemically stable, mechanically robust and, after oxygen plasma treatment, have a clean, graphitic surface.

PtNP-decoration was conducted in the same way as with pure GNP papers. Platinum precursor (CPA) was dissolved in polar, high-boiling point solvent (EG) at various concentrations (20, 200 and 1000 μM). Papers were placed in glass petri dishes and weighted down with a glass ring to eliminate movement from convection currents in the solvent during heating. Each paper (approximately 80 mm in diameter) was immersed in 40 ml of CPA/EG solvent and exposed to 45 seconds of 1200 W irradiation. Heating to near-boiling was observed, as evidenced by dense vapor and slight solvent volume loss. Samples were quenched in an (RO) water bath to prevent polymer flow and allowed to soak for 2 hours to clear residual solvent and unreacted CPA from the surface. Two-stage drying (2 hrs ambient conditions, 2 hrs under -25 inHg vacuum) produced dry papers that could be observed by FESEM.

As was seen in pure GNP papers, PtNP coverage over the whole surface of the paper was achieved. Small, discrete nanoparticles could be observed with minimal aggregation. Additionally, changes in precursor concentration led to changes in the number density of PtNPs on the surface. Figure 2.27 shows the increase in the extent of PtNP decoration as [CPA] is increased from 20 to 1000 μM .

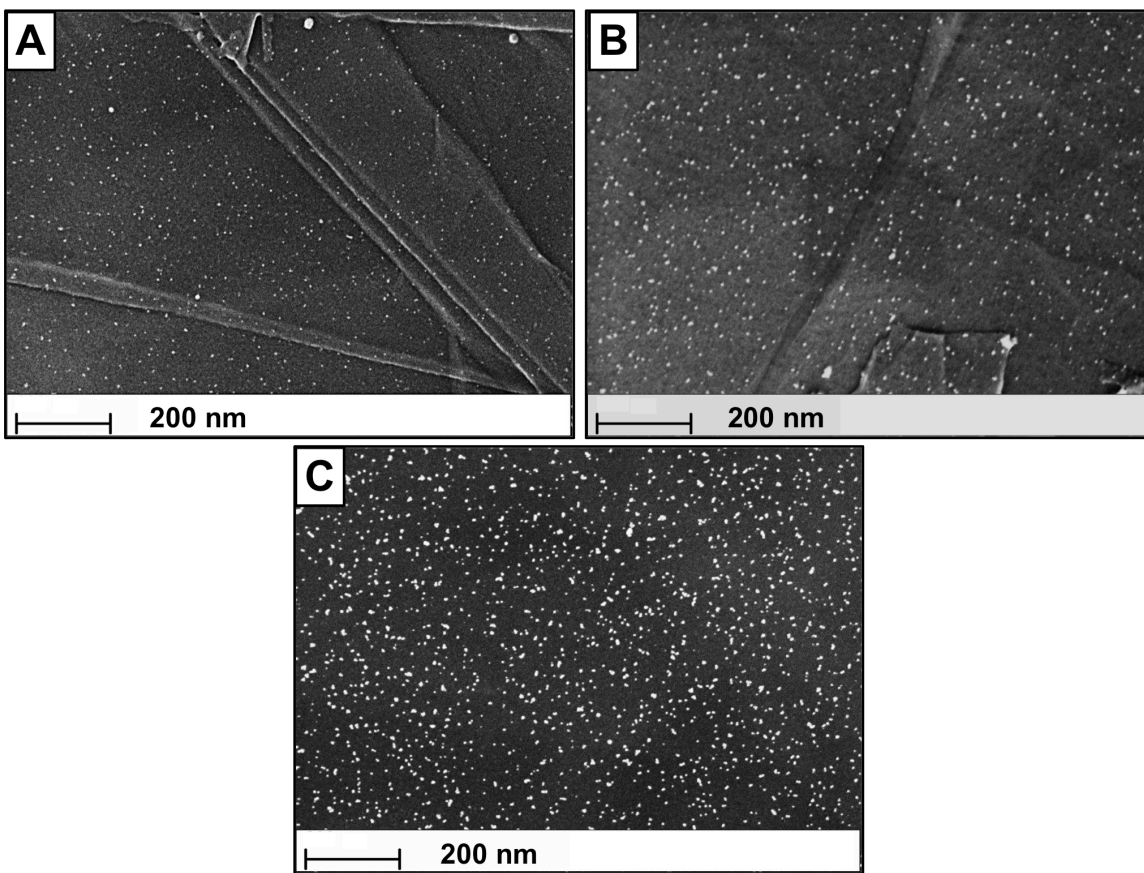


Figure 2.27: Representative images showing PtNP coverage of plasma-treated GNP/PP surfaces made by rapid microwave heating in (A) 20 (B) 200 and (C) 1000 μM CPA solutions. The increase in number density of PtNPs from low to high [CPA] can be clearly seen as well as the monodispersity of particle size and lack of aggregates.

Variation in number density within samples was observed on occasion, but in the center of the paper, where heating appears to be most uniform, PtNP coverage was very consistent both within and between samples.

Conclusions

As both films and papers, GNP proved to be a versatile and effective substrate for PtNP decoration. As thin films on glass substrates, PtNP-decorated GNP showed its capability as a coating. This method required minimal material usage and provided uniform coating of PtNPs. Despite problems with delamination, this method has great

potential for uniform deposition of catalytic and electrically conductive surfaces on varied substrates. Improvements in adhesion of the graphite material to the surface (by chemical bonding or matching of surface energies) could lead to facile production of low-cost, catalytic material with minimal inputs in terms of reagents and process energy.

As a paper, GNP showed great potential as well. For applications that are not limited by the internal porosity of the paper or the fragility of the material during processing or use, it has many advantages. The filtration process is rapid and scaleable and the highest processing temperature the system observes is 340°C (which could be avoided if a leaching process was chosen to remove the residual surfactant). The final material shows excellent PtNP coverage as well, providing a high surface area of Pt, while the substrate is easily cut to shape and adhered to rigid or flexible backing.

Perhaps the most promising assembly, however, is that of the GNP/PP composite papers. These materials showed improved durability during processing and, after a short surface treatment with oxygen plasma, show the same affinity for anchoring PtNPs as polymer-free papers. Though electrical properties drop off somewhat compared to pure GNP papers, their improved durability greatly expands their potential areas of application, to those where processing or use would tear or delaminate the binder-less papers. In addition to acting as a binder, the PP functions as a pore-filler, eliminating the problems of leaking or wicking electrolyte or solvent that would limit the effectiveness of porous, binder-free papers. These factors, along with the ability to control the number density of PtNPs deposited on the surface, make GNP/PP/PtNP systems the most intriguing of the systems studied, and will be further investigated in the following chapter.

REFERENCES

REFERENCES

- [1] R. J. Davis, E. G. Derouane, *Nature* **1991**, *349*, 313–315.
- [2] G. W. Huber, S. Iborra, A. Corma, *Chemical Reviews* **2006**, *106*, 4044–4098.
- [3] R. A. Sheldon, *Studies in Surface Science and Catalysis* **1991**, *59*, 33–54.
- [4] A. K. Santra, D. W. Goodman, *Electrochimica Acta* **2002**, *47*, 3595–3609.
- [5] H. Liu, C. Song, L. Zhang, J. Zhang, H. Wang, D. P. Wilkinson, *Journal of Power Sources* **2006**, *155*, 95–110.
- [6] N. Papageorgiou, W. F. Maier, M. Grätzel, *Journal of The Electrochemical Society* **1997**, *144*, 876–884.
- [7] J. Emsley, *The Elements*, Oxford University Press, Oxford, **1998**.
- [8] H. Song, R. M. Rioux, J. D. Hoefelmeyer, R. Komor, K. Niesz, M. Grass, P. Yang, G. A. Somorjai, *Journal of the American Chemical Society* **2006**, *128*, 3027–3037.
- [9] N. Semagina, L. Kiwi Minsker, *Catalysis Reviews* **2009**, *51*, 147–217.
- [10] A. Fukuoka, H. Araki, Y. Sakamoto, N. Sugimoto, H. Tsukada, Y. Kumai, Y. Akimoto, M. Ichikawa, *Nano Letters* **2002**, *2*, 793–795.
- [11] W. Tu, H. Liu, *Journal of Materials Chemistry* **2000**, *10*, 2207–2211.
- [12] W. X. Chen, J. Y. Lee, Z. Liu, *Materials Letters* **2004**, *58*, 3166–3169.
- [13] J. Lu, I. Do, L. T. Drzal, R. M. Worden, I. Lee, *ACS nano* **2008**, *2*, 1825–1832.
- [14] H. Wu, L. T. Drzal, *Carbon* **2012**, *50*, 1135–1145.
- [15] H. Wu, Multifunctional Nanocomposite Reinforced by Graphite Nanoplatelets, Michigan State University, **2011**.
- [16] X. Jiang, Multifunctional Polymeric Nanocomposites Fabricated by Incorporation of Exfoliated Graphite Nanoplatelets and Their Application in Bipolar Plates for Polymer Electrolyte Membrane Fuel Cells, Michigan State University, **2012**.
- [17] K. Kalaitzidou, Exfoliated Graphite Nanoplatelets as Reinforcements for Multifunctional Polypropylene Nanocomposites, Michigan State University, **2013**.

Chapter 3

Platinum-Decorated Composite Papers for Dye-Sensitized Solar Cell Counterelectrodes

Background

As mentioned in the introduction, photovoltaic power generation is a rapidly expanding industry and there is intense interest in developing a number of next-generation devices to improve performance compared to the silicon-based devices that currently dominate the market [1,2]. One of the leading candidates, DSSCs, have potential to reduce production cost greatly. Though the current configurations have reached a maximum of 15.0% efficiency (for hybrid organic/inorganic devices [3] and 13.1% for organic sensitizers [4]), continued dye engineering, photoanode construction and electrolyte development hold the potential to improve cell efficiency and close the performance gap between DSSCs and commercial, silicon devices.

In addition to continued performance enhancement, economics must be considered as well. As a proof of concept, DSSCs with FTO-glass substrates and thermalized platinum catalytic electrodes have performed admirably, but for commercialization, changes are necessary. The standard, thermalized catalytic electrode is fabricated by spin-coating or drop casting a Pt precursor in volatile solvent, followed by heating at temperatures around 400°C [5]. Pt loading in these standard systems typically range from 30-60 $\mu\text{g}/\text{in}^2$ [5-7], a non-trivial cost [8-10]. In Chapter 2, a GNP/PP/PtNP electrode material was developed that has the potential to replace the conductive oxide

and reduce the Pt loading, removing two of the biggest cost barriers in DSSC production [11].

Morphological observation of the two types of catalytic electrodes makes it clear that GNP/PP/PtNP can greatly reduce Pt loading. Top-down and tilted views of the thermalized, FTO/Pt surface shows the presence of numerous aggregates on the surface (see Figure 3.1 and Figure 3.2).

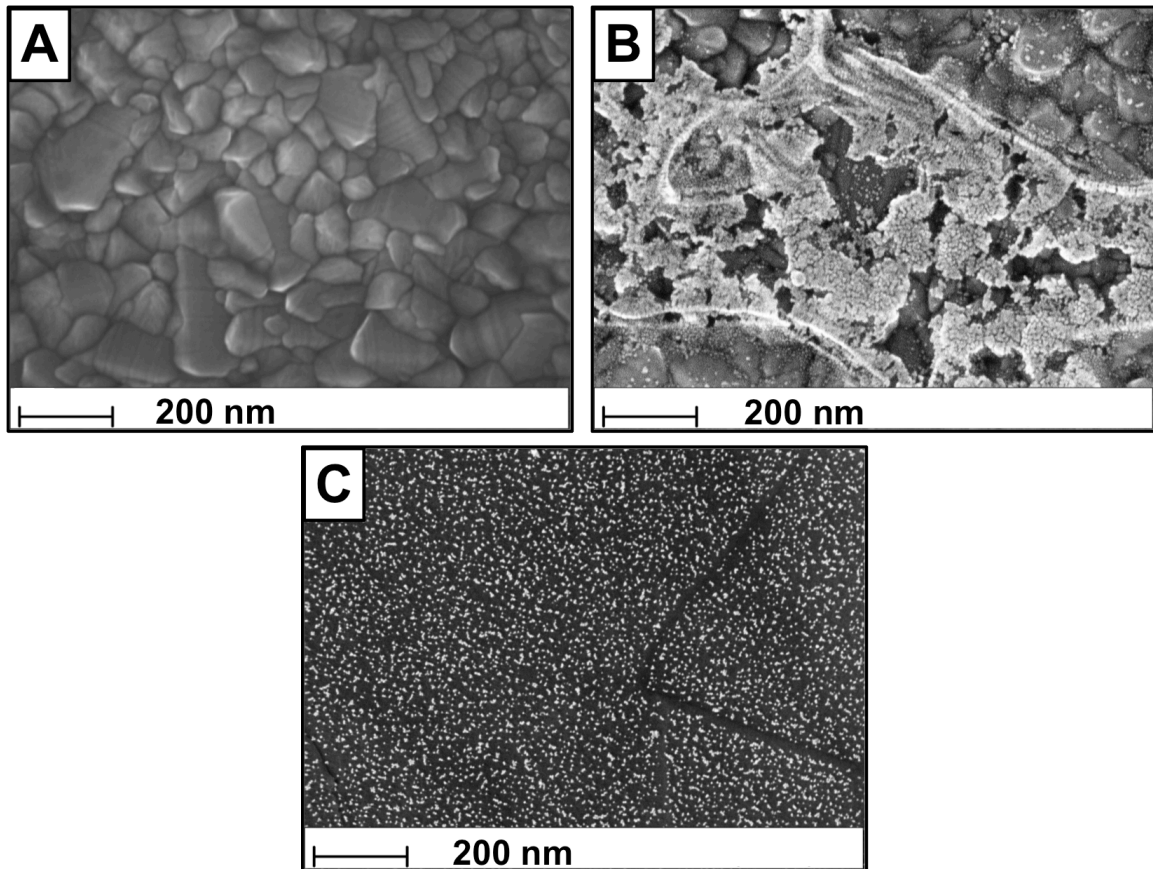


Figure 3.1: Top-down view of FTO surface (A) before and (B) after Pt coating by thermal decomposition of precursor at 400°C for 15 min. Large aggregates seen over whole surface of sample, a sharp contrast to the discrete PtNP coverage seen in (C) GNP/PP/PtNP samples prepared by rapid microwave irradiation. All images are at identical magnification.

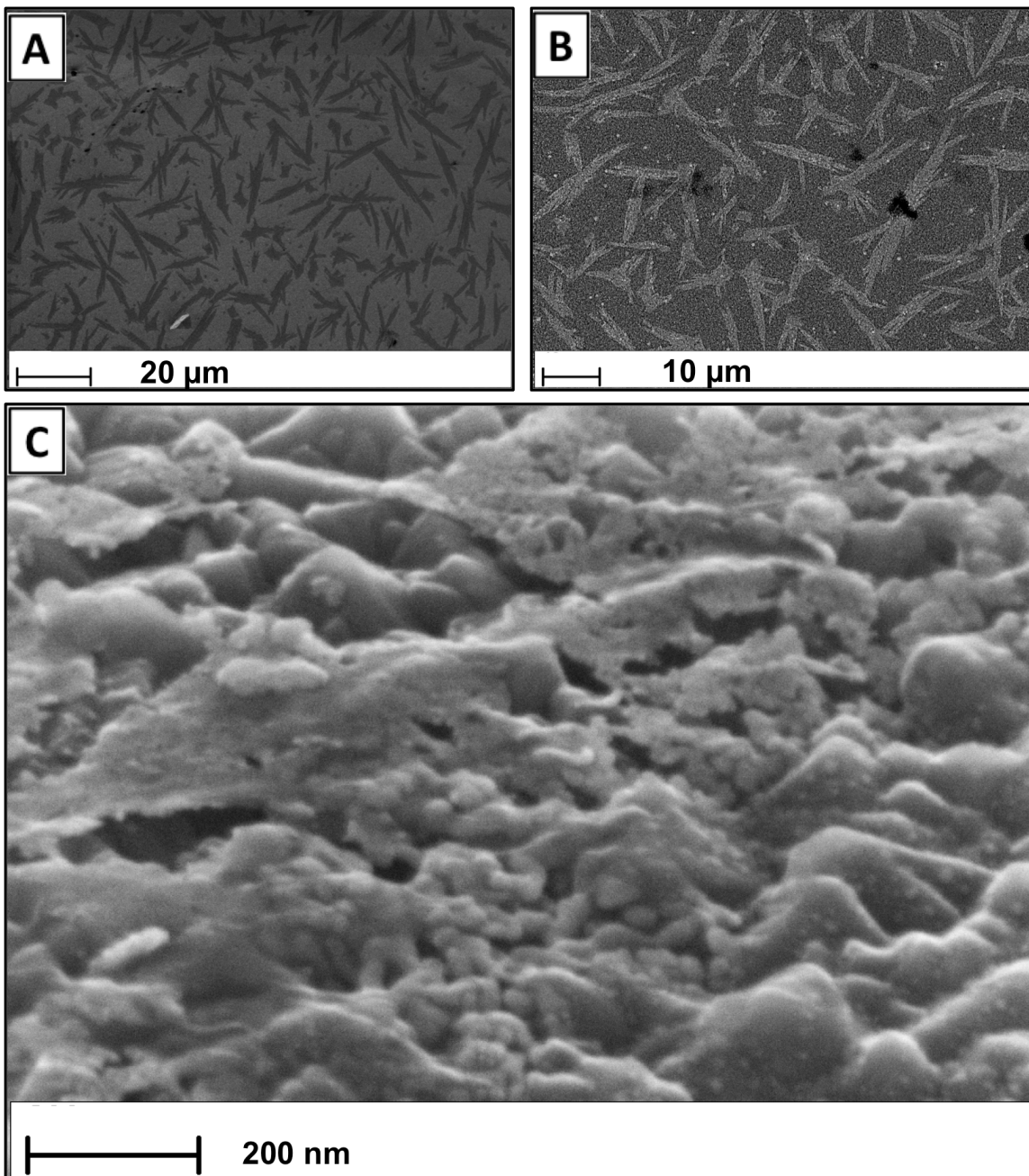


Figure 3.2: Top-down view of thermalized FTO system at low magnification with (A) secondary electron (SE) detector and (B) back-scatter electron detector. Using a high tilt angle of 60° and the SE detector illustrates the large size of Pt aggregates on top of the FTO crystallites

The presence of discrete nanoparticles in the GNP/PP/PtNP system provides higher surface area per unit mass than the highly-aggregated Pt structures seen in the FTO/Pt

system. To quantify Pt loading in the two catalytic surfaces, samples were examined by XPS and inductively coupled plasma mass spectroscopy (ICP-MS).

XPS is a surface sensitive technique, observing electrons emitted from the top layers of atoms (on the order of 50 Å sampling depth [12]) after X-ray illumination. Because only surface Pt (that is exposed to electrolyte) can provide a catalytic effect, XPS provides a unique measure of the amount of Pt likely to participate in catalysis. Samples were cut from the GNP/PP/PtNP paper with a razor and FTO/Pt samples were prepared by scoring with a diamond scribe and fracturing (a PTFE cover was used when fracturing FTO/Pt substrates to prevent abrasion of surface material). As seen in Figure 3.3, all three GNP/PP/PtNP samples (prepared from 20, 200 and 1000 μM CPA/EG solutions) showed significantly lower Pt loading than the FTO/Pt samples.

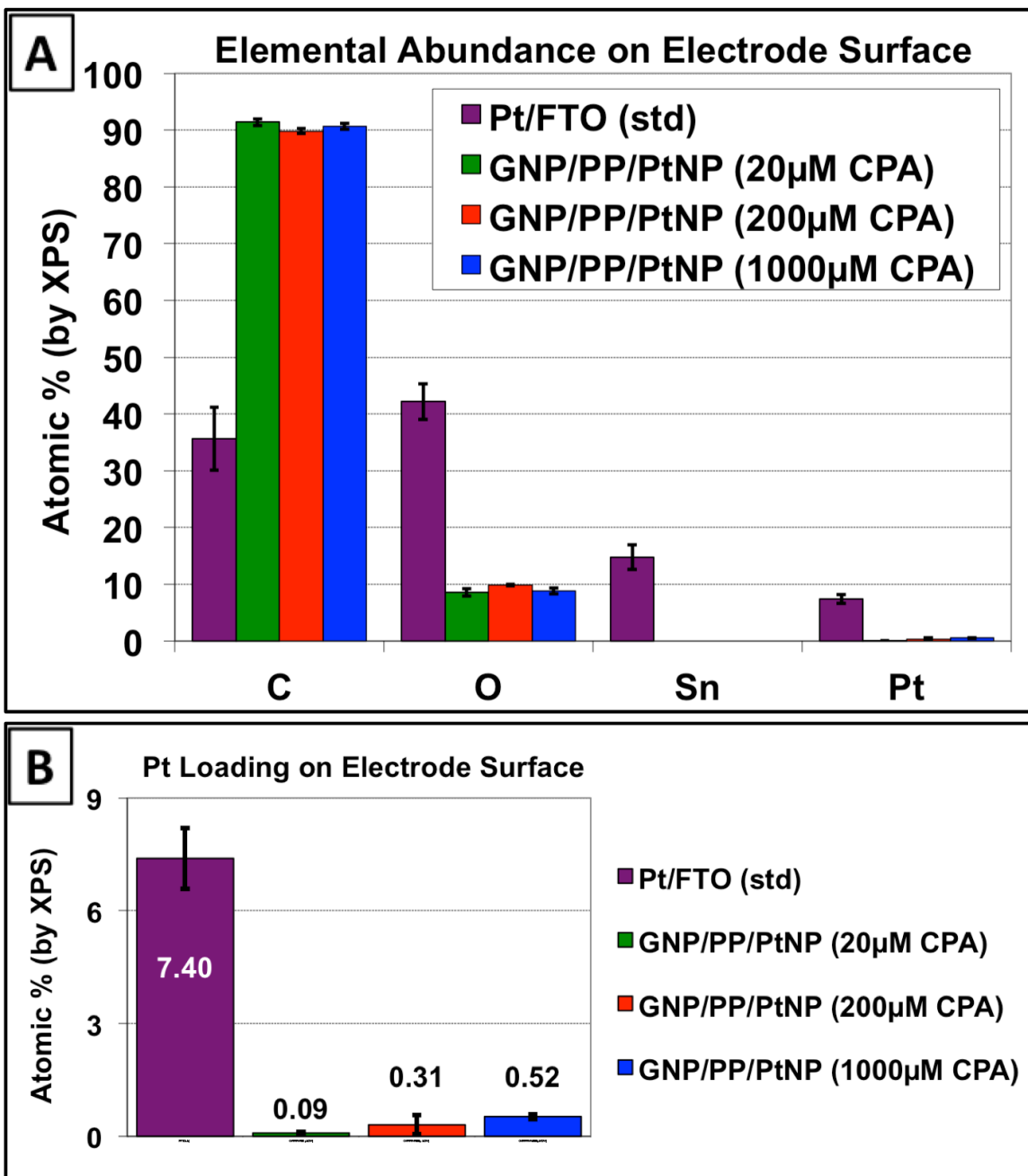


Figure 3.3: (A) Elemental abundance and (B) Pt loading at surface of GNP/PP/PtNP and FTO/Pt samples as measured by XPS. Measurements were made on a Perkin Elmer Phi 5400 ESCA system with a magnesium $K\alpha$ X-ray source. Samples were analyzed at pressures between 10^{-9} and 10^{-8} torr with a pass energy of 29.35 eV and a take-off angle of 45° . The spot size is roughly $250 \mu\text{m}^2$. Atomic concentrations were determined using previously determined sensitivity factors. All peaks were referenced to the signature C1s peak for adventitious carbon at 284.6 eV.

The XPS data indicate clearly that, despite dense surface coverage with PtNPs, the Pt loading after rapid microwave heating is at least a an order of magnitude lower than surfaces prepared by the conventional thermalization technique.

While XPS provides valuable information of the nature of the catalytic surface, in terms of economics, the absolute Pt loading in the catalytic material is the key metric. To find the total Pt loading, acid digestion and ICP-MS were performed. From each type of surface, 1 in by 1 in samples were prepared (GNP/PP/PtNP samples were cut with a razor blade, FTO/Pt samples were scored with a glass cutter and fractured to size). Samples were then exposed to a concentrated aqua regia solution, boiled at 300°C to dissolve Pt, diluted and measured by ICP-MS. Figure 3.4 shows the results of the quantification and a comparison to XPS data.

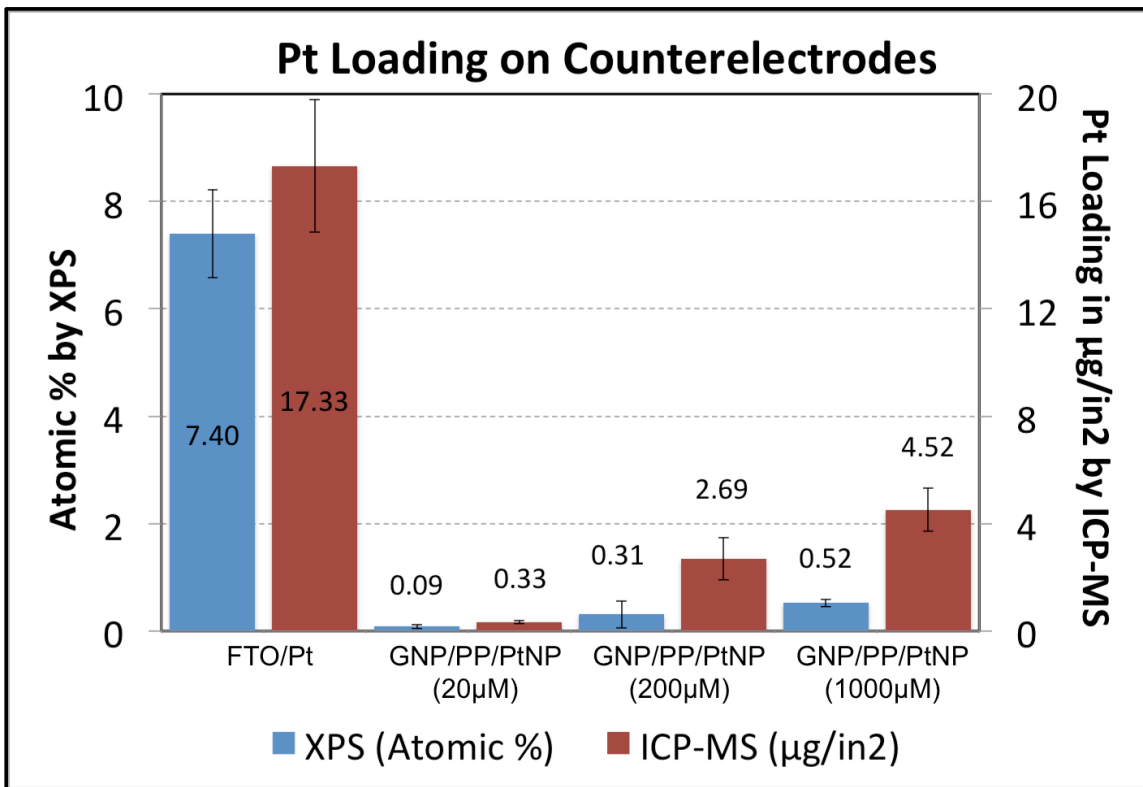


Figure 3.4: Quantification of Pt loading by XPS and ICP-MS.

Both characterization techniques show Pt loading to be lower in GNP/PP/PtNP samples than in the FTO/Pt standard. Additionally, both techniques show that for rapid microwave heating, CPA concentration can be used to control final Pt loading on the sample (within the range of concentrations studied). Though the trends are the same in both types of measurement, the relative amount of Pt detected in the samples differs by a significant amount. Comparing the FTO/Pt standard with the GNP/PP/PtNP samples with the highest loading, XPS suggests Pt has been reduced by a factor of 14, while ICP-MS suggests the reduction is only a factor of 3.8. This discrepancy can be explained by a few observations.

The standard thermalization technique makes use of drop-casting and slow evaporation of solvent before high temperature treatment [5,7]. No reagent should be lost during the formation of metallic Pt at the surface, meaning the final loading should be equal to the amount initially used in solution. ICP-MS measurements, therefore, appear to be an underestimate. The $5 \mu\text{L}/\text{cm}^2$ of 5 mM CPA solution used would yield $31.5 \mu\text{g}/\text{in}^2$ Pt loading. It is possible that the aqua regia dissolution step was too mild to fully dissolve the Pt aggregates or that material was abraded away during cutting, resulting in an ICP-MS value 45% lower than the theoretical loading.

Additionally, XPS is a surface-sensitive technique, measuring only tens of angstroms from the surface. PtNP presence below this sampling depth would appear in ICP-MS measurements, but not XPS. However, cross sectional analysis suggests this is not likely the case. The use of PP as a binder blocks off pores between graphite platelets, making penetration of the CPA/EG solvent into the depth of the paper unlikely (especially considering the viscous and polar nature of the solvent, which would wet the non-polar

GNP and PP surfaces quite poorly). Recall from Chapter 2, that confocal microscopy observation of GNP/PP paper cross sections mounted in a fluorescent epoxy showed negligible porosity (see Figure 2.19).

To verify that no PtNP decoration had occurred below the surface of the GNP/PP paper, adhesive tape was applied to the top and peeled away, delaminating of the top few layers of graphite, exposing the surface below. The exposed surface was then observed by FESEM. Figure 3.5 shows the delamination process and FESEM images of the surface.

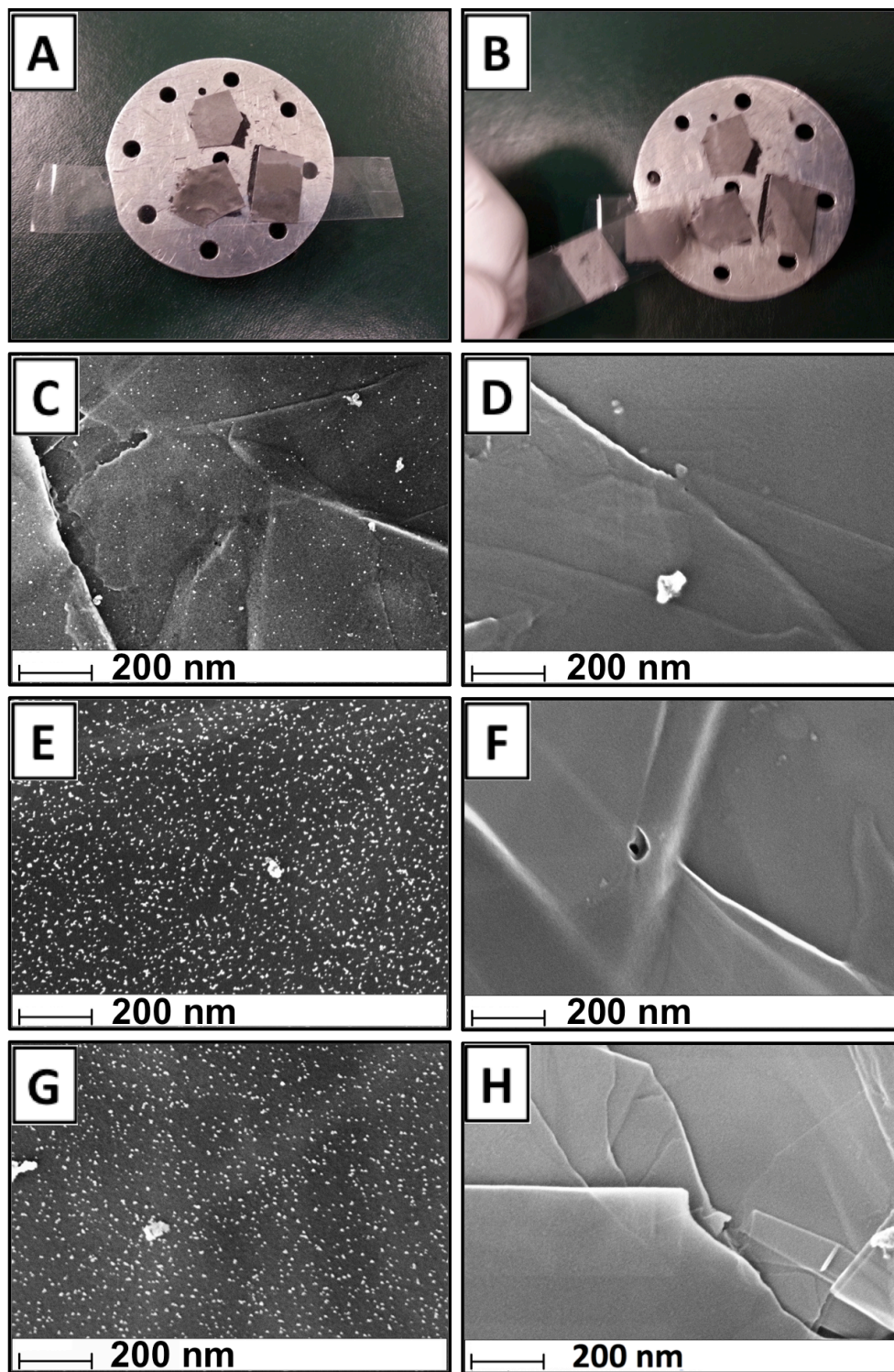


Figure 3.5: Top images show GNP/PP/PtNP samples adhered to FESEM mount (A) before and (B) after delamination with adhesive tape. Below, images show 20 μM CPA-treated GNP/PP/PtNP sample (C) before and (D) after delamination experiment. 200 μM CPA sample (D) before and (E) after and 1000 μM CPA sample (F) before and (G) after.

FESEM images show clearly that PtNP growth is not present throughout the paper. To better gauge the distribution of PtNP throughout the paper thickness, a separate system was observed, with nanoparticle decoration occurring in suspension instead of at the surface of a paper. A small suspension of GNP platelets was made by sonicating 25 mg of GNP worms in 50 ml EG for 10 min at 10 W. CPA was added to the suspension to make the concentration 200 μ M. This suspension was stirred vigorously for 30 min then microwaved for 90 sec at 1200 W. After washing, centrifuging (5000 rpm for 15 min) and decanting 3X with RO water, the PtNP-decorated suspension was then drop-cast on aluminum stubs and observed with FESEM. Careful imaging of the surface showed that nanoparticles present on layers of graphite below the surface could be easily seen because of the sampling depth of the high voltage electron beam (15 kV accelerating voltage). Figure 3.6 shows the presence of nanoparticles both at the surface and on the layers below.

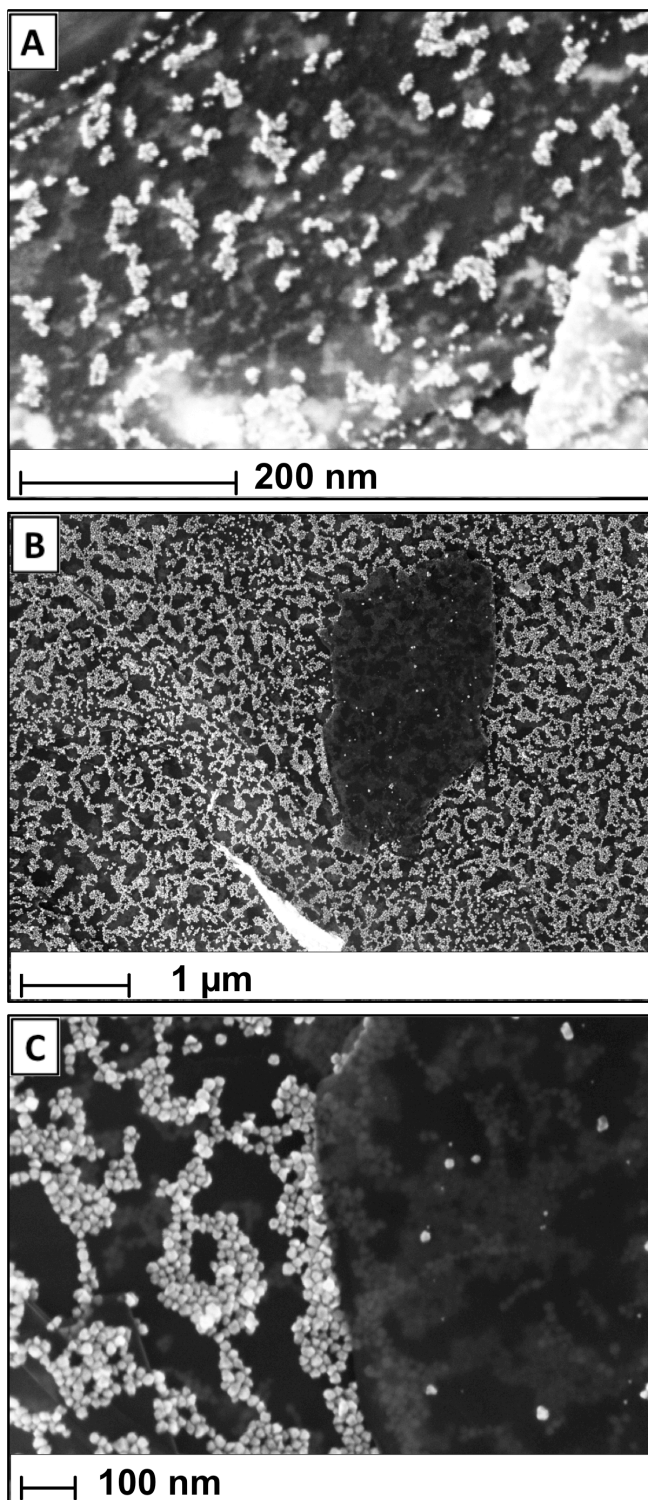


Figure 3.6: FESEM imaging of the surface of the suspension-processed, nanoparticle-decorated GNP. Image (A) shows a single GNP particle with brightly visible PtNPs on top and faint PtNPs visible on the bottom of the platelet. Image (B) shows a single, uncoated GNP particle sitting on top of one that is nanoparticle-decorated. Image (C) is a 5X zoom of image (B).

GNP that is decorated individually, in a suspension, clearly shows nanoparticle coverage over the first few layers. The GNP/PP/PtNP system, which is decorated as a paper, with only the surface exposed, shows no indication of covered PtNPs below the top layer. Together, observation of delaminated papers and suspension decorated platelets show that PtNP appears to be confined to the paper surface.

Few possibilities are left to explain the higher Pt loading reported by ICP-MS (compared to XPS). It seems most likely that the “bottom” side of the GNP paper (which was in contact with the glass petri dish during PtNP-decoration) and was completely submerged in the solution. FESEM imaging the bottom surfaces shows non-uniform Pt-coating. Occasionally large aggregates can be found, but most often the paper appears to be very sparsely covered with PtNPs. Figure 3.7 shows the high variation in Pt coverage at the bottom of the paper samples.

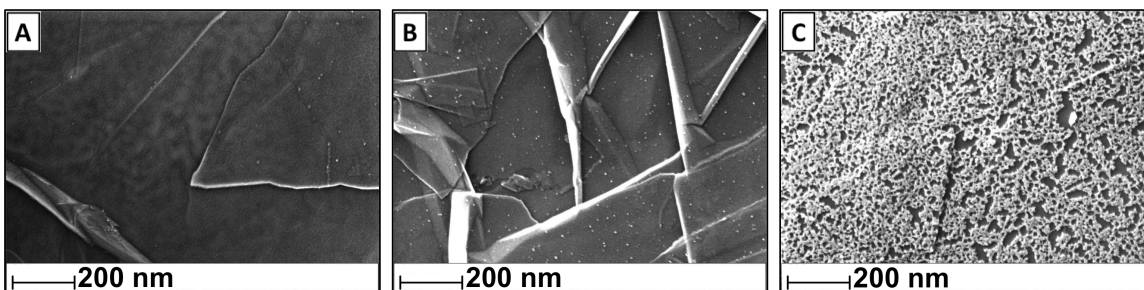


Figure 3.7: Bottom of GNP/PP/PtNP paper showing (A) no PtNP coverage over most of the imaged area (B) sparse PtNP coverage in some areas and (C) very infrequent dense coverage of PtNPs and large aggregates.

This variation was the reason for using the top of the paper for the catalytic surface, which was consistently uniform in particle size and spatial distribution. In preparation for ICP-MS characterization the bottom surfaces of GNP/PP/PtNP papers were abraded with a paper towel to limit the measurement of Pt loading to the top surface. However, the PtNP removal process was not optimized and the higher Pt loading seen by ICP-MS,

compared to XPS, seems most likely to be due to residual Pt coverage on the bottom of the paper.

Despite minor disagreement in Pt loading measurements, the GNP/PP/PtNP system appears to be a significant improvement in Pt morphology. Extensive FESEM imaging and multiple characterization techniques show that PtNP loading on GNP/PP papers can be controlled and provide a surface with significant reductions in PtNP loading compared to the standard FTO/Pt system used in DSSCs. To gauge the value of these papers as counterelectrodes, however, electrochemical analysis was necessary to verify that the high surface area PtNPs would indeed provide the catalytic performance of the standard system.

Catalytic Activity

Standard methods [13,14] for analyzing electrochemically active area by hydrogen adsorption in dilute, aqueous, sulfuric acid were investigated, but the non-polar GNP surface wet poorly and showed minimal signal. Instead, electrochemical measurements were conducted in an electrolyte system commonly used in DSSCs, iodide (I_2)/triiodide (I_3^-) in acetonitrile [15-17]. A solution of 5 mM LiI, 0.5 mM I_2 and 0.1 M $LiClO_4$ in acetonitrile was prepared. A three-electrode configuration was used, with a Pt foil as the counterelectrode and leak-free Ag/AgCl as the reference. To check for proper system function a second, Pt foil electrode was used as the working electrode and cyclic voltammetry (CV) measurements were made. Sweeping from -0.25 up to 1.25 V (with respect the Ag/AgCl reference) at 50 mV/s provided a number of peaks, all characteristic of the electrolyte system. Figure 3.8 shows the reduction of I_3^- to I^- occurring at ~ 0.1 V

and the reduction of I_2 to I_3^- at ~ 0.6 V [15-17]. The corresponding oxidation peaks (from I^- to I_3^- and I_3^- to I_2) can be seen at ~ 0.3 and 0.7 V respectively [15-17].

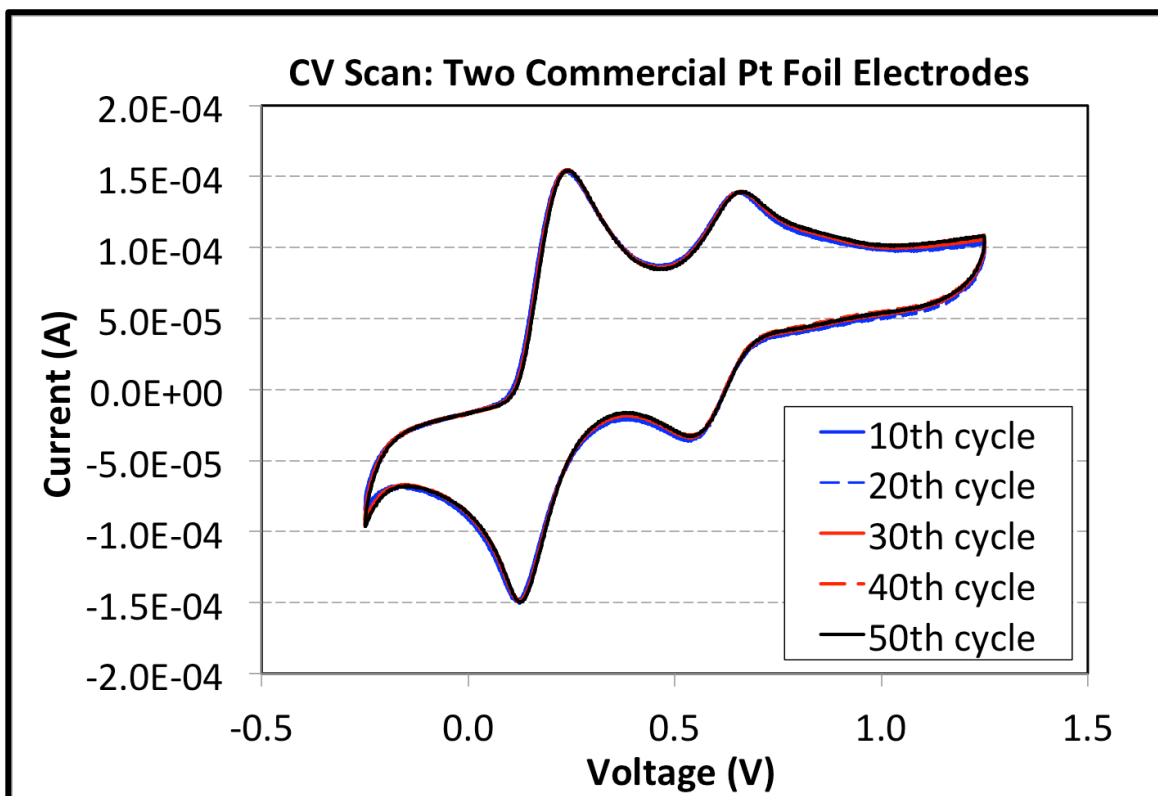


Figure 3.8: Cyclic voltammery baseline measurements of commercial Pt foil working electrode. Three electrode cell with Pt foil counterelectrode and Ag/AgCl reference electrode. Electrolyte was 5 mM LiI, 0.5 mM I_2 and 0.1 M $LiClO_4$. Scan rate was 50 mV/s.

With the two Pt foil electrodes showing peak shapes and locations comparable to those in literature, specimens were prepared from both the GNP/PP/PtNP paper system and the thermalized FTO/Pt system. Small (~ 5 mm by 5 mm) sections were cut and copper tape leads were attached with a fast-drying, silver conductive paste. The copper leads and a rigid, polystyrene backing were wrapped in PTFE film (tested and proven to be stable in acetonitrile) to eliminate electrolyte exposure to the copper tape. The area of the exposed

catalytic surface was then measured by reflected light microscopy. Examples of the assembled electrodes and images for nominal area measurements can be seen in Figure 3.9.

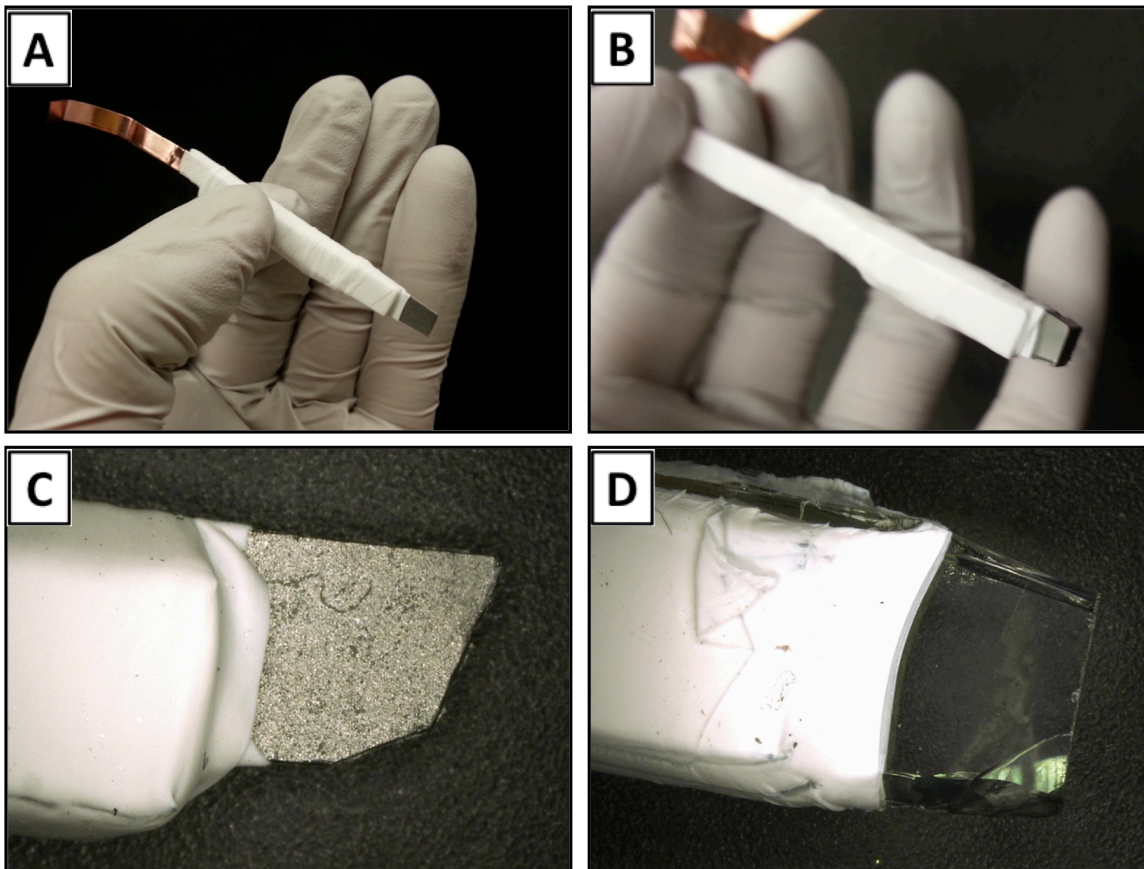


Figure 3.9: Images showing (A) GNP/PP/PtNP and (B) FTO/Pt electrode assembly and reflected light microscope images used for area measurement of (C) GNP/PP/PtNP and (D) FTO/Pt catalytic surfaces.

These assembled electrodes were then inserted into fresh electrolyte (5 mM LiI, 0.05 mM I_2 , 0.1 M $LiClO_4$ in acetonitrile) and cycled to the same voltage limits as the commercial Pt foil had been. The experimental setup for the CV measurements can be seen in Figure 3.10.

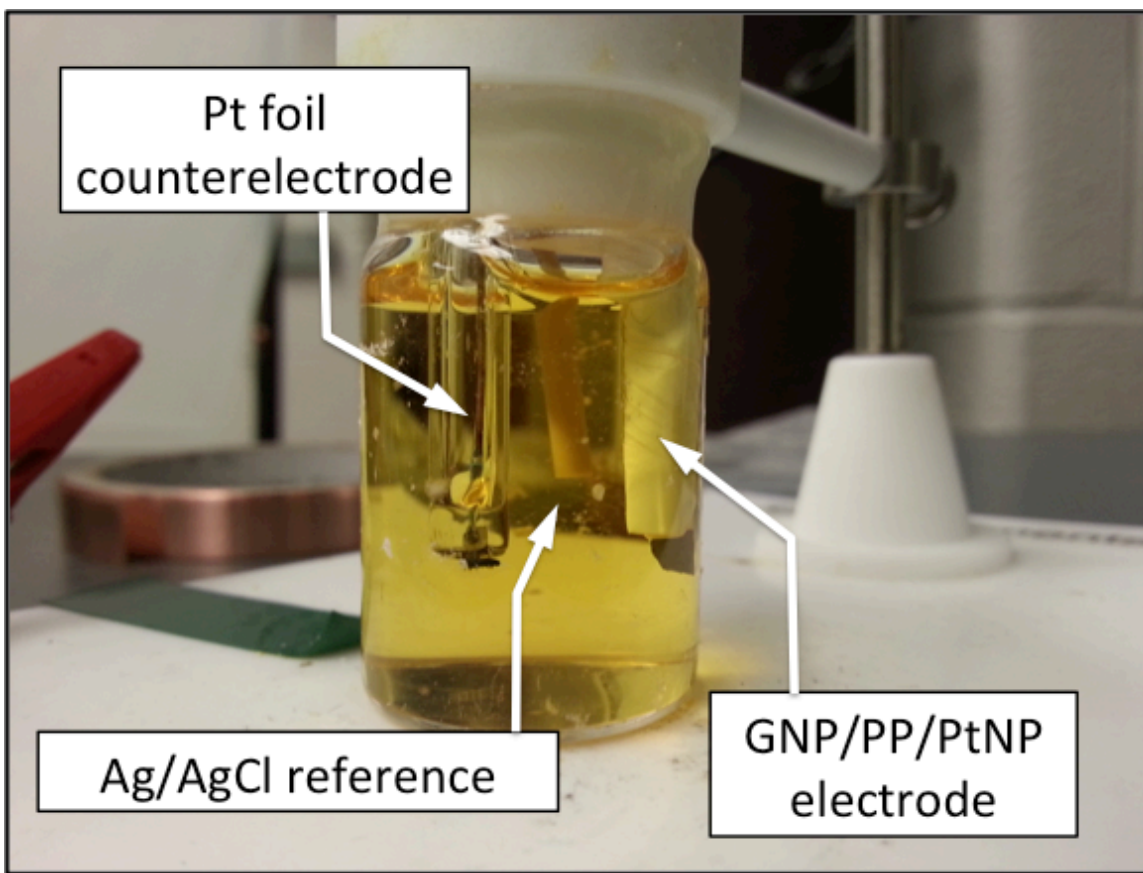


Figure 3.10: Three-cell configuration for measuring catalytic activity of GNP/PP/PtNP and FTO/Pt surfaces.

Values were compared at the tenth cycle (allowing the system to reach equilibrium) and normalized to the electrode area (as measured by optical microscopy). Figure 3.11 compares CV scans for the FTO/Pt standard, each GNP/PP/PtNP sample as well as a control sample of GNP/PP (which had been microwaved in pure EG in the absence of Pt precursor).

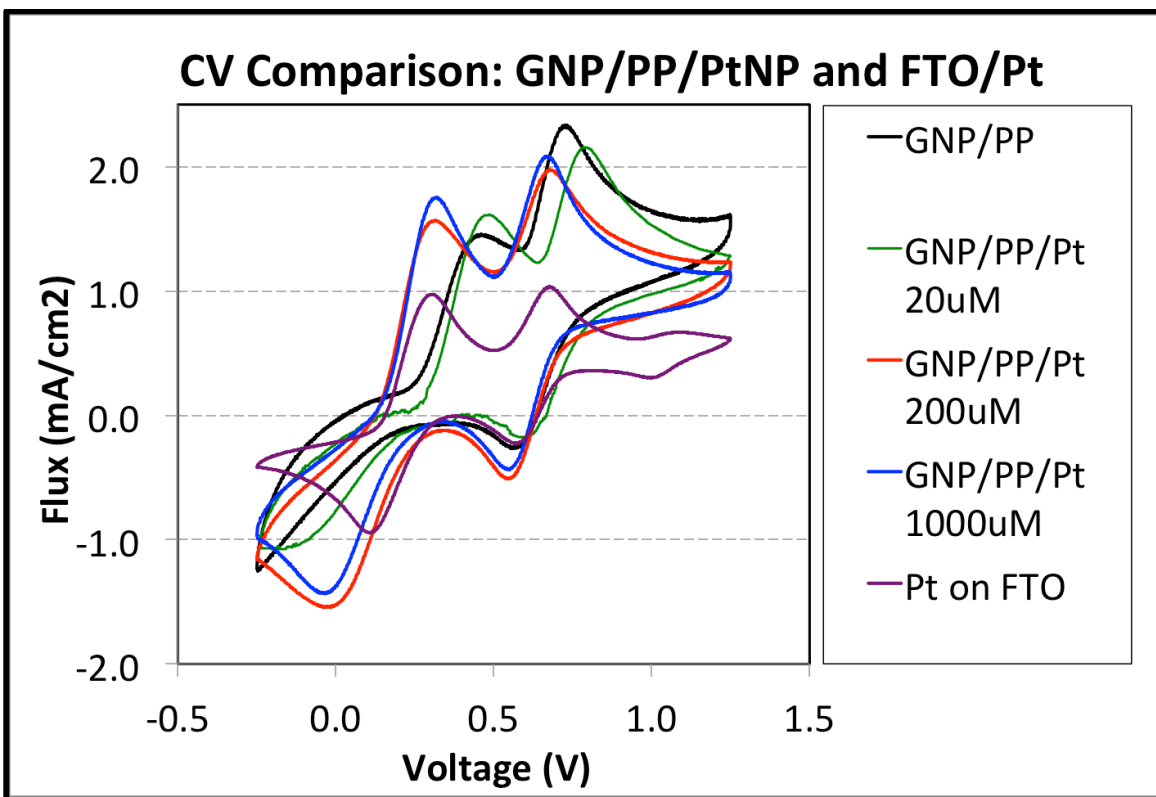


Figure 3.11: CV comparison of catalytic activity on the 10th cycle of GNP/PP/PtNP and FTO/Pt samples. Electrolyte was 5 mM LiI, 0.5 mM I_2^- and 0.1 M $LiClO_4^-$. Scan rate was 50 mV/s.

As the CV scans show, despite having *at least* a 3.8-fold *lower* amount of Pt present, GNP/PP/PtNP samples show *higher* current than FTO/Pt at the peak corresponding to I_3^- reduction, the key reaction at the DSSC counterelectrode. The control, microwave-treated GNP/PP sample, which lacks an I_3^- reduction peak, shows that this catalytic effect is due to the high surface area PtNP coating, rather than a chemical modification of GNP by microwave heating. Additionally, the 200 and 1000 μ M CPA-treated samples show noticeably higher reduction peaks than the 20 μ M CPA sample, which was believed to be caused by the higher Pt loading. The similarity in the 200 and 1000 μ M curves is likely caused by sample variation (notice the overlap in error bars for Pt loading of the 200 and

1000 μM samples in Figure 3.4). A simplified comparison of the two systems can be seen in Figure 3.12.

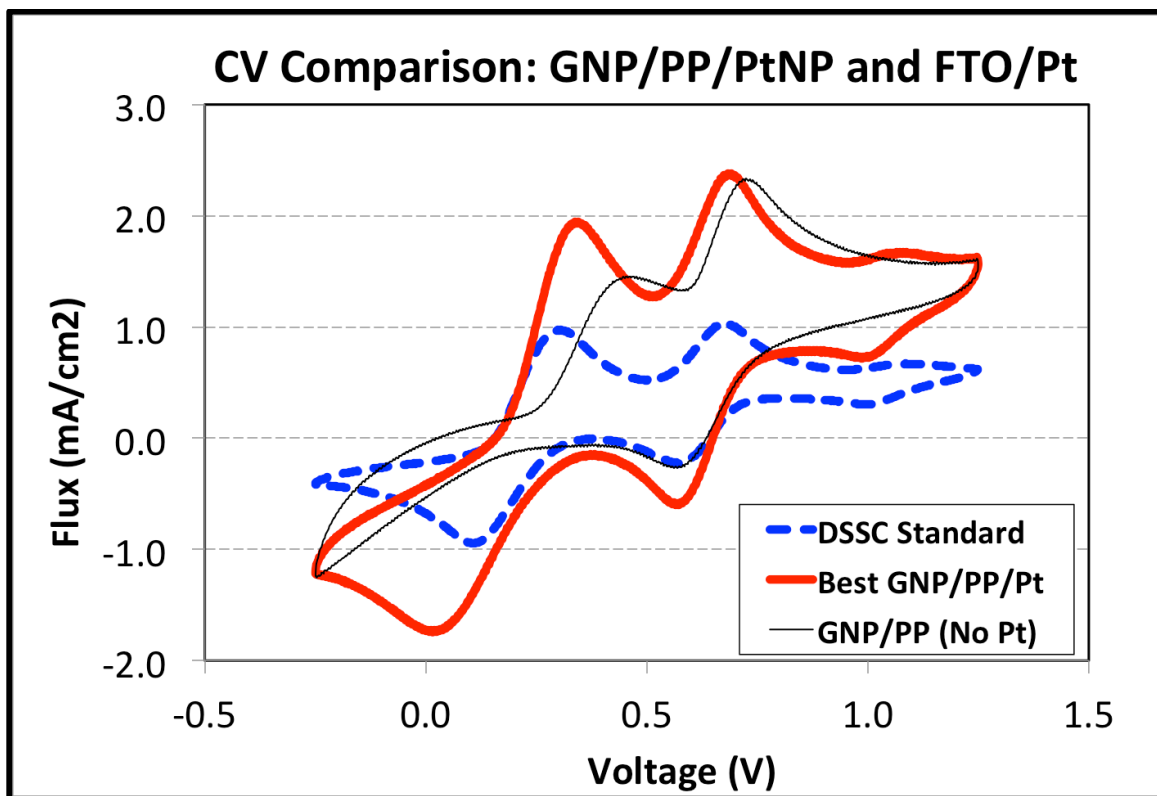


Figure 3.12: CV comparison (10th cycle) of GNP/PP/PtNP, GNP/PP control and thermalized Pt electrodes. Electrolyte was 5 mM LiI, 0.5 mM I_2 and 0.1 M LiClO_4 . Scan rate was 50 mV/s.

Voltammetry experiments were repeated and longer runs, up to 50 cycles, were done.

Loss of the I_3^- reduction peak and variability in peak height were concerns, but subsequent deconstruction of cells, washing of the electrode surface and examination with XPS showed that noticeable ClO_4^- adsorption had occurred. FESEM examination of the surfaces after 50 cycles showed clear PtNP presence, suggesting the loss in current after CV cycling was due to adsorption of ions from the electrolyte, rather than Pt dissolution. Figure 3.13 shows the clear Pt presence after CV.

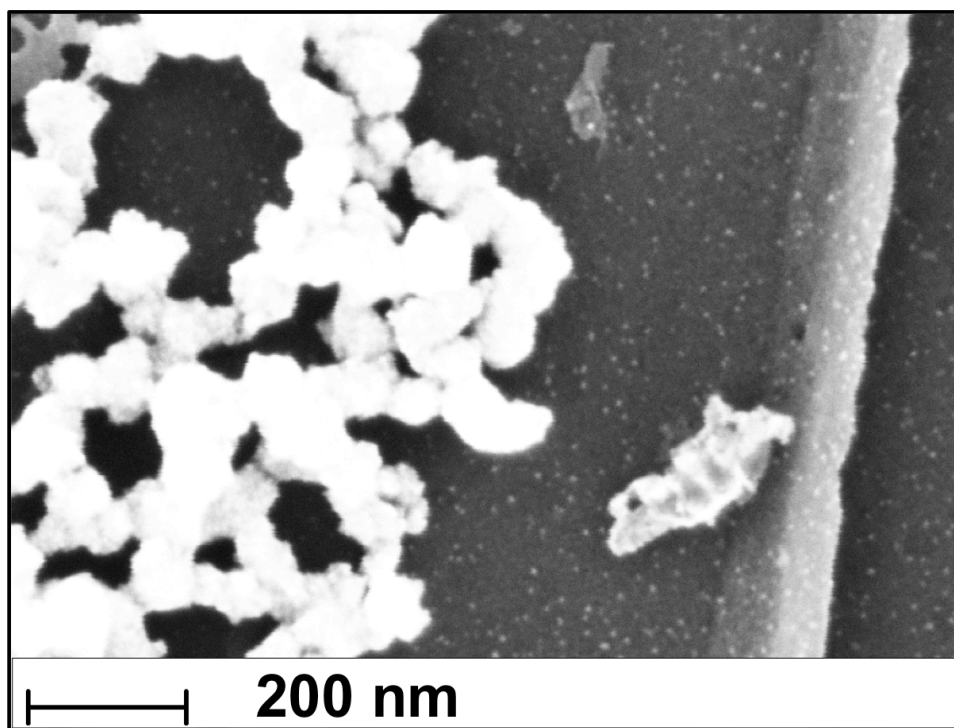


Figure 3.13: FESEM images of a GNP/PP/PtNP paper (1000 μM CPA) after CV cycling, acetonitrile soaking and drying.

In addition to the small, discrete PtNPs normally seen, a few large Pt aggregates (left half of image) could be seen as well, indicating the Pt appears to be very stable in the electrolyte system chosen.

With GNP/PP/PtNP surfaces found to (a) significantly reduce Pt loading and (b) effectively catalyze I_3^- reduction, they passed the two major qualifications for DSSC counterelectrode function. Full cell construction was undertaken to evaluate their effectiveness in that role.

DSSC Fabrication

For GNP/PP/PtNP characterization, much of the samples were prepared as free-standing papers. For electrochemical analysis and DSSC fabrication, however, samples had to be firmly adhered to rigid substrates to minimize topography (which could bridge

the gap to the anode and cause shorts) and allow proper sealing. As mentioned in Chapter 2, use of a PTFE mask during pressing prevented abrasion of PtNPs from the surface. An illustration of paper-cutting, pressing and final counterelectrode appearance is found in Figure 3.14.

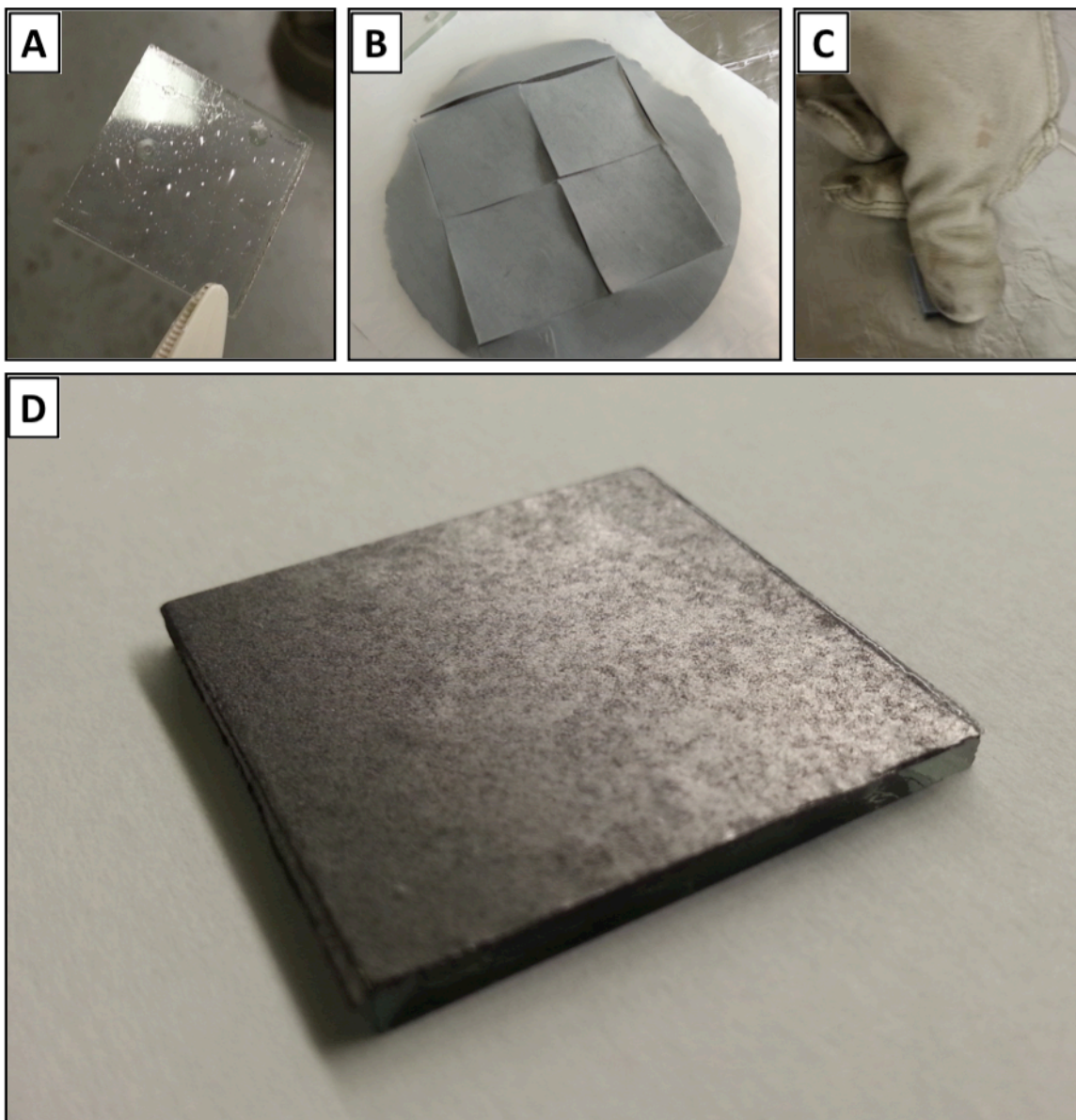


Figure 3.14: Counterelectrode fabrication process including (A) heating of Surlyn to molten state (B) cutting GNP/PP/PtNP paper to fit glass substrate and (C) pressing GNP/PP/PtNP onto molten Surlyn with PTFE mask to prevent abrasion. Image (D) shows the completed counterelectrode.

After pressing, FESEM was used to examine the sample surface and verify that PtNP coverage was unaffected. Numerous samples were made with virtually no abrasion effects detected so long as the PTFE mask was placed over the sample surface during pressing.

Prior to optimizing composite paper fabrication, DSSCs were built from GNP thin films and binder-free papers. Despite having substantial PtNP coverage, the devices failed because of electrolyte leakage. In contrast, the GNP/PP papers performed quite well holding electrolyte in preliminary tests. Figure 3.15 shows the comparison between a seal made with by pressing molten Surlyn between pure GNP paper versus pressing between GNP/PP paper.

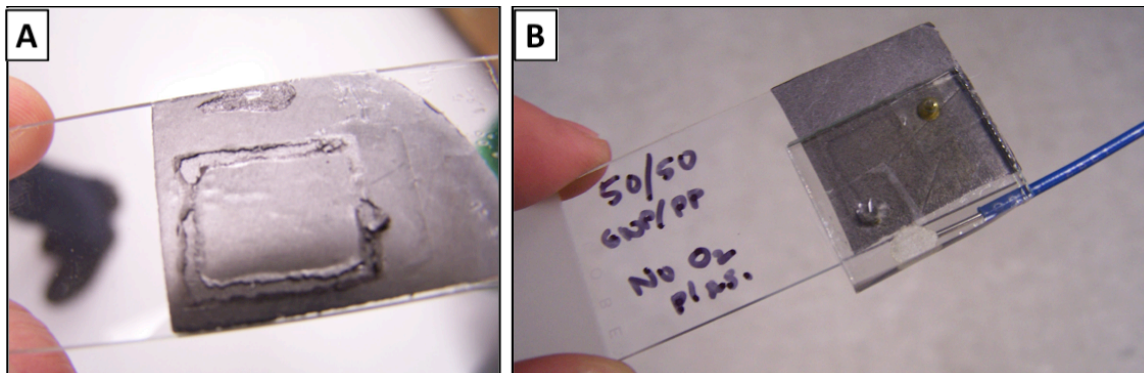


Figure 3.15: Comparison of sealing efficacy of (A) pure GNP paper and (B) GNP/PP paper.

Without PP binder, the GNP easily delaminates when exposed to any transverse or shear loading. In contrast, the GNP/PP sample holds up to sealing and handling and, as shown in Figure 3.15B, still shows the yellow coloration indicating electrolyte presence several days after loading.

Despite reasonable success with the Surlyn seal, difficulty applying enough heat and pressure to properly adhere the molten polymer and the GNP/PP became significant

challenges. The Surlyn seals easily when heated to $>100^{\circ}\text{C}$, however, heating the substrates beyond 70°C can lead to problems of dye desorption during cell construction. Adding pressure can alleviate this problem, but the fragile glass substrates can end up cracking if too much pressure is applied.

Though cells performs best with thin gaps between anode and cathode layers (ideal in the $10\text{-}20\ \mu\text{m}$ created by the Surlyn seal), using larger separators is possible because of the low viscosity and high conductivity of the electrolyte. Rubber gasket material was chosen as the replacement to Surlyn sealing, allowing liquid-tight contact between GNP/PP surfaces by applying mechanical pressure. EPDM sheeting with a $1/32$ in ($800\ \mu\text{m}$) thickness was cut into a window shape and placed between anode and cathode. Two thin-gauge syringes (23.5 G) were placed between the two layers, one for filling with electrolyte, the other to allow passage of air during filling to eliminate bubbles. An illustration of the sealing process can be seen in Figure 3.16.

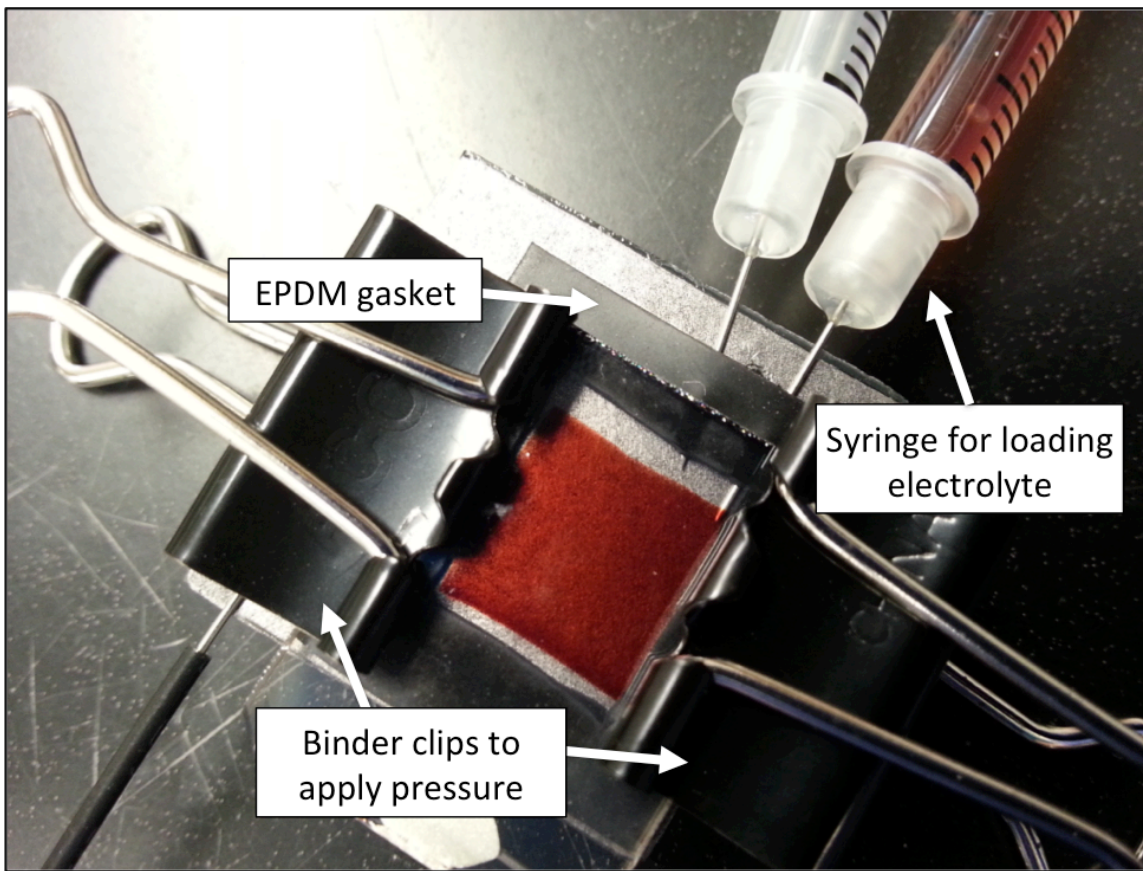


Figure 3.16: Full cell assembly, including photoanode, counterelectrode, EPDM rubber gasket, binder clips to provide pressure for seal and syringes for loading electrolyte.

This configuration was tested on “dummy” cells (with no Pt loading on counterelectrode nor semiconductor nor dye on anode) and electrolyte was found to remain sealed for up to a week with minimal solvent loss.

For full cell characterization, photoanodes were prepared according to common procedures reported in literature [7,18]. Commercial TiO_2 paste (Ti-Nanoxide HT/SP from Solaronix) was doctor-bladed on a $15 \Omega/\square$ FTO-glass substrate to form a 7-10 μm -thick film measuring 1 cm in length and width. Samples were then sintered by a four-stage heating process (325°C for 5 min, 375°C for 5 min, 450°C for 5 min and 500°C for 15 min). This TiO_2 layer was then soaked in a dye solution (“N3” dye at 0.3 mM in

ethanol) for 24 hours. Anodes were then rinsed with acetonitrile to remove loose dye and then dried under nitrogen flow for 20 minutes.

Electrolyte-filling, described above, was performed slowly to minimize bubble formation and leaking through the gaps near the syringe needles. Samples were filled with 0.3 M LiI, 0.03 M I₂, 0.2 M tert-butylpyridine in spectral grade acetonitrile. After 5 to 10 min allowing electrolyte to absorb into the porous semiconductor layer and reach equilibrium, electrochemical characterization began.

To compare the effectiveness of GNP/PP/PtNP counterelectrodes with standard counterelectrodes, thermalized Pt layers were prepared on 15 Ω/□ FTO-glass as well. A 5 mM solution (CPA in anhydrous 2-propanol) was drop cast on surfaces at a loading of 5 μl/cm². Solvent was then evaporated slowly for 20 minutes under ambient conditions, followed by heating to 400°C for 15 min.

DSSC Characterization

Sets of (4) complete cells were prepared for each type of sample. GNP/PP/PtNP papers from 20, 200 and 1000 μM CPA treatment were made, as well as control GNP/PP samples that had been plasma treated and exposed to rapid microwave heating in pure EG. FTO/Pt samples were used as the baseline to gauge the effectiveness of GNP/PP/PtNP-based devices. Current and voltage characteristics of the cells were measured on a CH Instruments (Model 650D) potentiostat under illumination from a 450 W Xenon arc lamp (Horiba Jobin Yvon FL 1039/40). An AM1.5 filter was used and intensity was set to 100 mW/cm². Figure 3.17 shows the JV curves of each of the cells

tested, Table 3.1 lists averages of cell parameters and Figure 3.18 shows the power conversion efficiency averages.

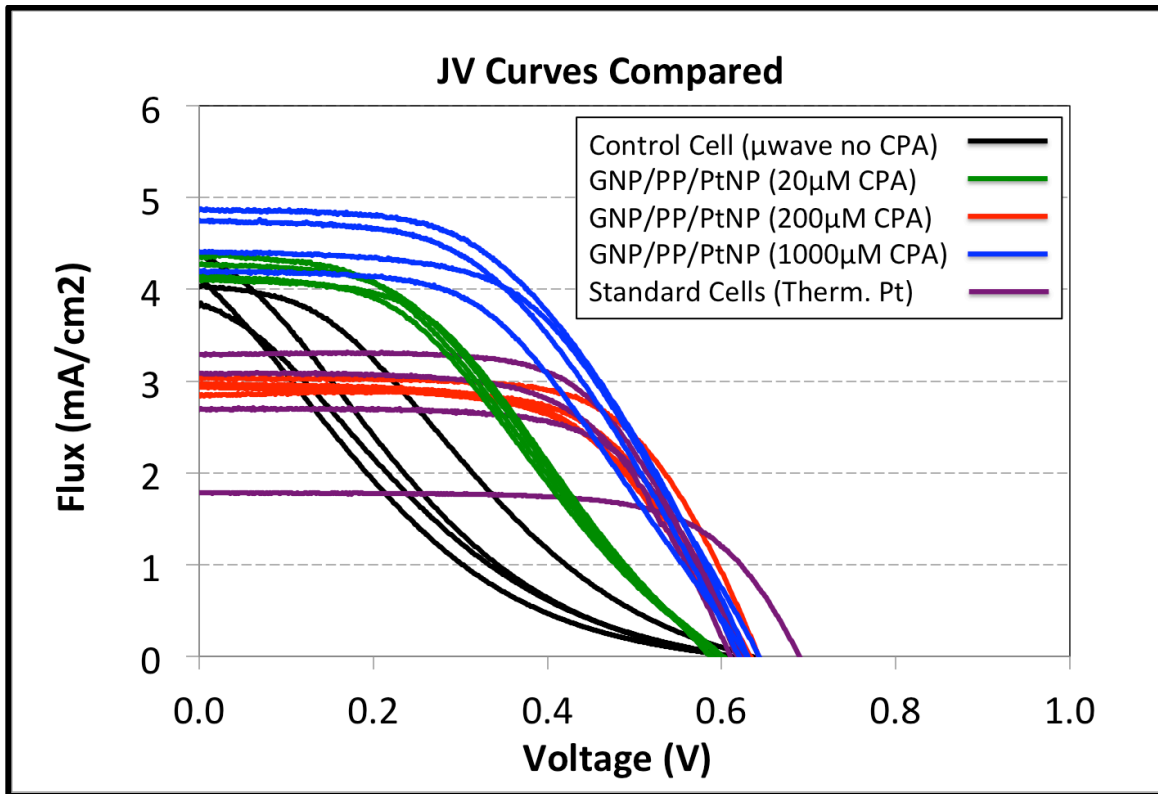


Figure 3.17: All JV curves measured for FTO/Pt standards and GNP/PP/PtNP-based cells.

Table 3.1: Cell Parameter Averages

Cell Type	J_{SC} (mA/cm ²)	V_{OC} (V)	η (%)	ff
GNP/PP Control	4.08	0.62	0.49	0.20
GNP/PP/PtNP (20 μ M CPA)	4.22	0.59	0.98	0.39
GNP/PP/PtNP (200 μ M CPA)	2.95	0.63	1.13	0.61
GNP/PP/PtNP (1000 μ M CPA)	4.55	0.63	1.41	0.49
FTO/Pt	2.71	0.64	1.08	0.64

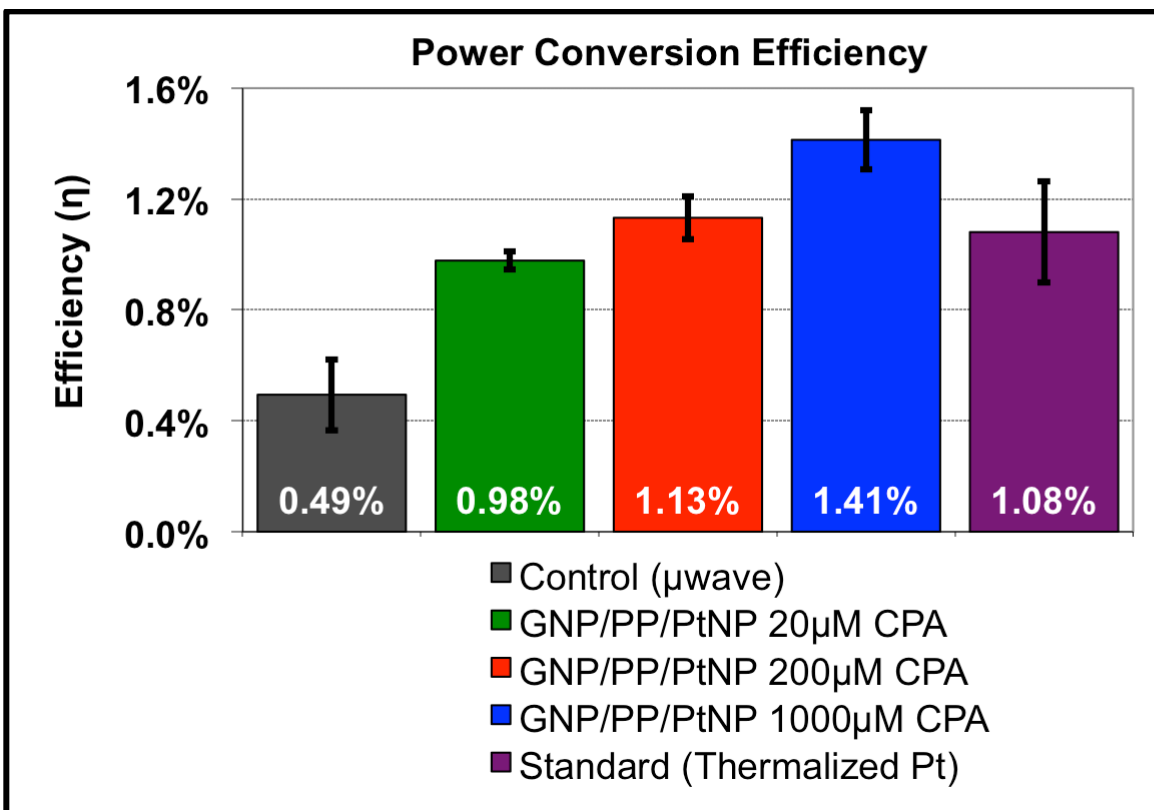


Figure 3.18: Power conversion efficiency averaged for each group of (4) cells.

Looking at the full set of curves, a few trends emerge. First, it is quite clear that the best performance comes from the GNP/PP/PtNP cells from the 1000 μ M CPA treatment. They show the highest current and match the open circuit voltages of the other categories as well. Their average efficiency of 1.41% bests that of the thermalized Pt standards by 31%, a remarkable result considering their Pt loading is lower by at least 74%. These values confirm the claim that increasing Pt surface area by controlling morphology can improve cell performance while simultaneously reducing Pt loading.

Secondly, each batch of cells appears quite consistent from sample to sample in terms of curve shape and current values. To simplify the comparison, Figure 3.19 shows a representative curve from each sample group (the sample whose conversion efficiency most closely matches the group average).

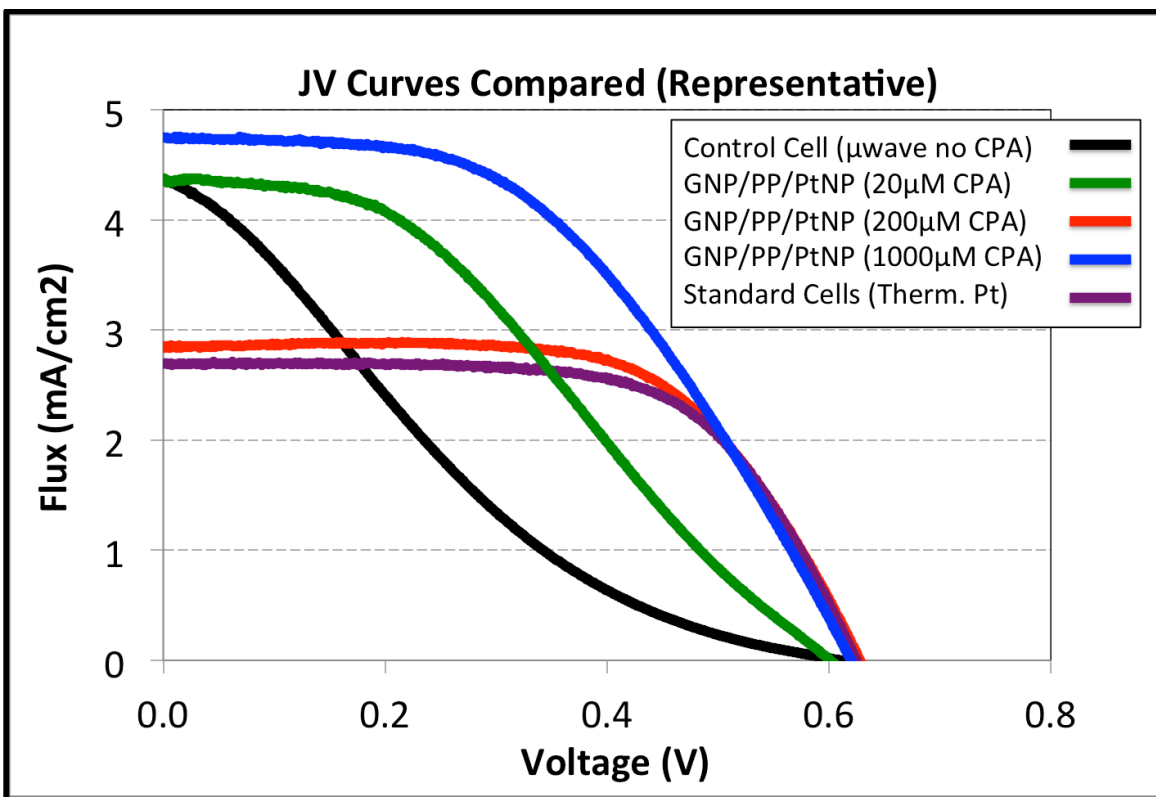


Figure 3.19: Comparison of representative JV curve from each sample group.

Samples from the 200 μM GNP/PP/PtNP group appear nearly identical to the FTO/Pt standard in terms of both curve shape and efficiency. It is safe to assume that in this range of PtNP loading, the available surface area of Pt is comparable to that the FTO/Pt standard (despite being a factor of 6.4 lower in absolute Pt loading) and reducing PtNP coverage any further is detrimental to cell performance.

The two remaining sets of samples, 20 μM CPA-treated GNP/PP/PtNP samples and GNP/PP controls show very interesting results. They both show high J_{SC} values, low fill factors and V_{OC} values comparable to other groups. Their low efficiency is not surprising, in that Pt loading is reduced so far it would be expected that \bar{I} conversion was inadequate to regenerate the oxidized dye. The “S” shape of the curve is interesting as

well. In bulk heterojunction devices, this shape can be found when charge transfer between the two junction is limited, resulting in increased recombination [19]. Jeong et al. note a similar behavior in DSSC devices with novel, Pt-free counterelectrodes, citing “large internal series resistance” as the culprit [20]. Regardless of the mechanism, the effect of reducing Pt beyond a necessary threshold is clear: poor cell performance.

A comparison of JV curves run without illumination verify the cells function as diodes. The samples (20 μM and Pt-free control) that showed the S-shaped curves under illumination show no such artifact on their dark curves (see Figure 3.20).

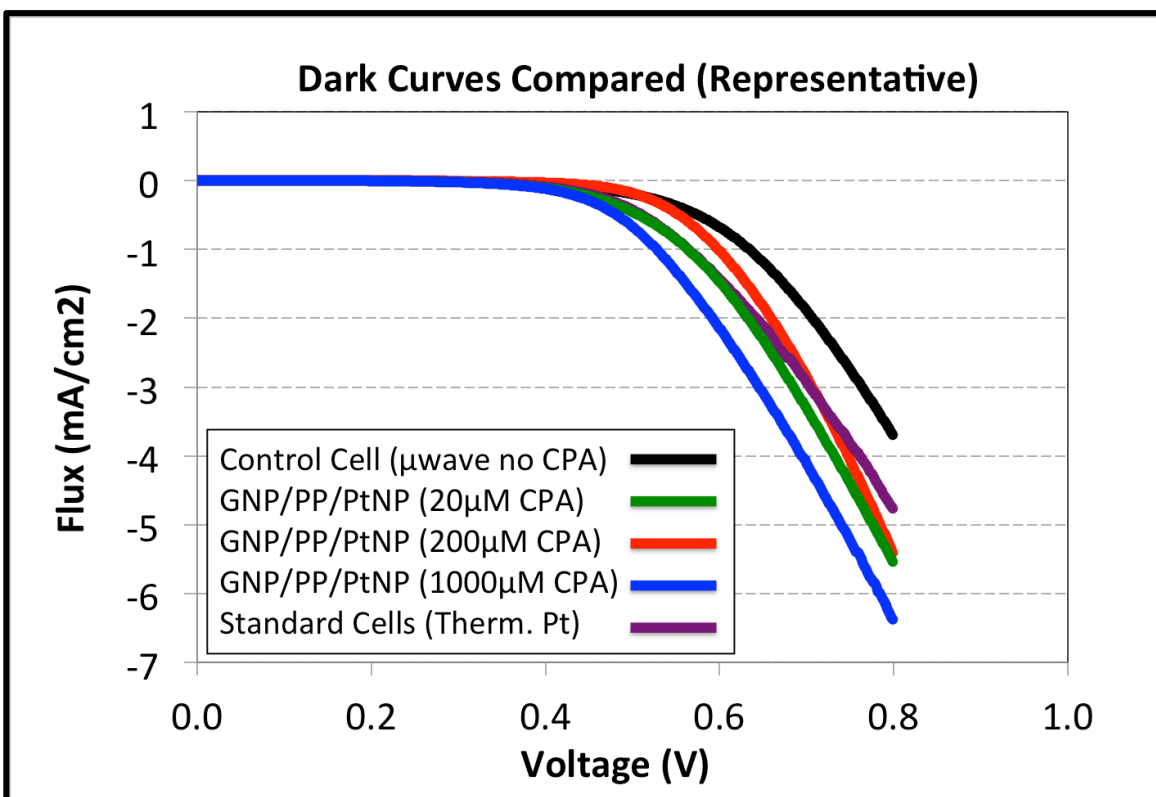


Figure 3.20: Representative JV curves without illumination

This suggests the lower levels of performance in those cells when illuminated was caused by limitations in regenerating \bar{I} at the electrode surface, rather than poor electrical connectivity between components.

Impedance Characterization

The JV curves of GNP/PP/PtNP-based solar cells suggested excellent catalytic performance but a more direct measure is electrochemical impedance spectroscopy (EIS). By using a low-amplitude alternating current and sweeping from high to low frequencies, information on electron transfer at the counterelectrode-electrolyte interface can be gathered, as well as information on resistance due to diffusion in the electrolyte [21]. Symmetrical cells were prepared with 1 in by 1 in catalytic electrode specimens made identically to those prepared for solar cells. These two counterelectrode surfaces were clamped together with an EPDM rubber gasket spacer and binder clips to provide pressure. Electrolyte filling was again performed with a two-syringe system to prevent air bubbles distorting electrochemical data. A solution of 0.3 M LiI and 0.03 M I₂ in spectral grade acetonitrile was used as electrolyte. Conductive silver epoxy was used to fix copper leads to the catalytic surfaces, which were then connected to a CH Instruments potentiostat (Model 650D), forming a two-cell configuration. A bias of ±10 mV was applied (around a 0 V setpoint) and the frequency was swept from of 50 kHz to 0.1 Hz. With FTO/Pt standards, it was found that after a -1 V to 1 V sweep to condition the electrode surfaces, consistent data was obtained.

Numerous samples of each cell type (FTO/Pt, GNP/Pt and GNP/PP) were run and Nyquist plots were compared to calculate a charge transfer resistance. Figure 3.21A shows the consistently low charge transfer resistance (R_{CT}) values obtained for FTO/Pt samples (obtained by taking half the width of the hemisphere).

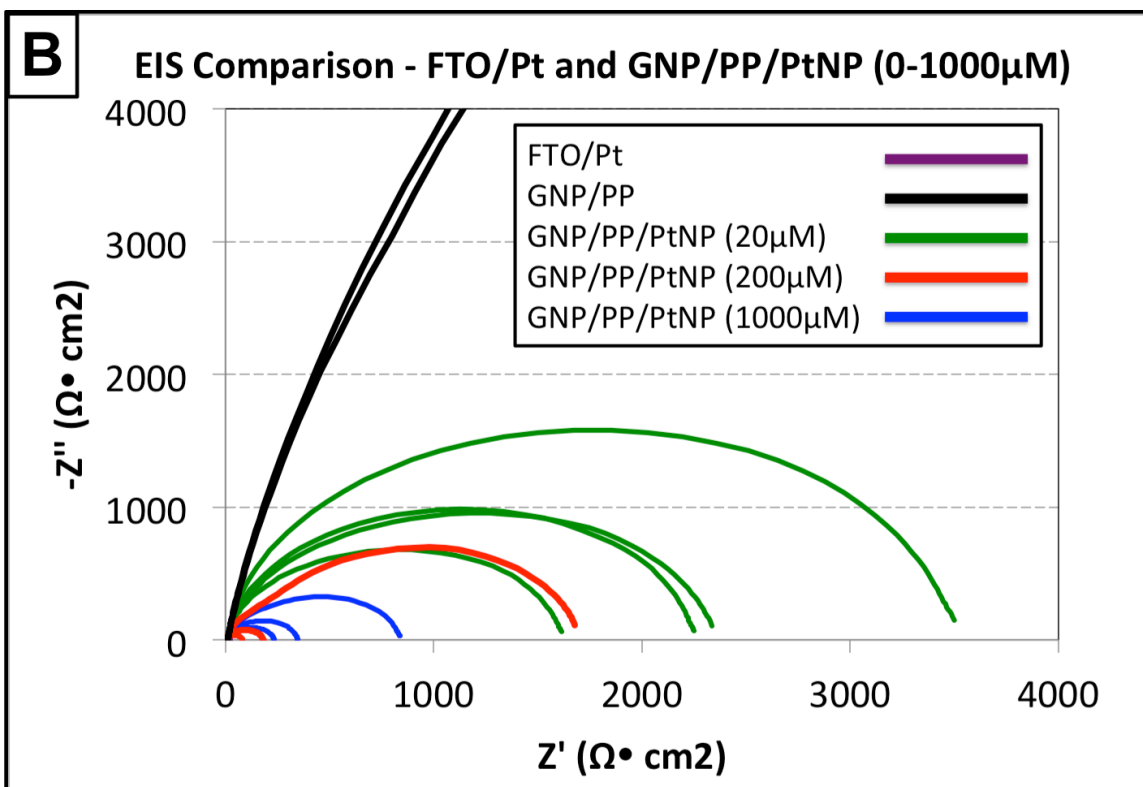
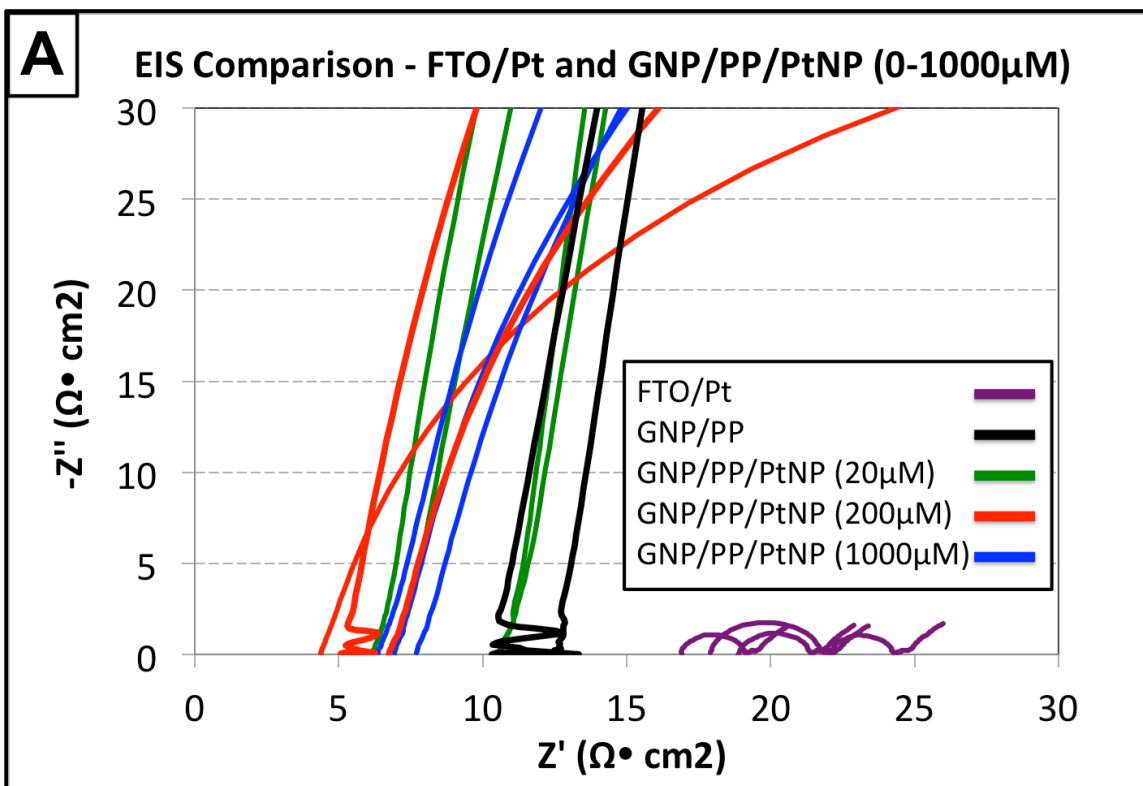


Figure 3.21: Nyquist plots of catalytic electrode surfaces at (A) low impedance values and (B) zoomed out to show the high impedance values.

Figure 3.21B shows the same data plotted on a different scale, showing R_{CT} values for GNP-based samples at least two to three orders of higher than the FTO-based samples. Considering the excellent performance of GNP-based electrodes on both CV and illuminated JV experiments, seeing such high values was unexpected. Samples were repeated after extensive conditioning and with higher frequency sweeps (to ensure that the large impedance values were indeed indicating high R_{CT} , rather than showing impedance associated with diffusion in the electrolyte). Samples were run at higher amplitudes as well, as high as ± 50 mV, without seeing a noticeable change in R_{CT} .

The only procedural change that actually improved R_{CT} values for GNP-based electrodes was an increase in the setpoint for the applied bias. By changing from a ± 10 mV cycling around 0 V, to a ± 10 mV cycling around 1 V, the impedance values for GNP/PP/PtNP systems dropped drastically, while that of FTO/Pt samples increased. Figure 3.22 shows that R_{CT} values both approach $20 - 30 \Omega/\text{cm}^2$ at higher bias, a drastic change from the orders of magnitude difference seen at no bias.

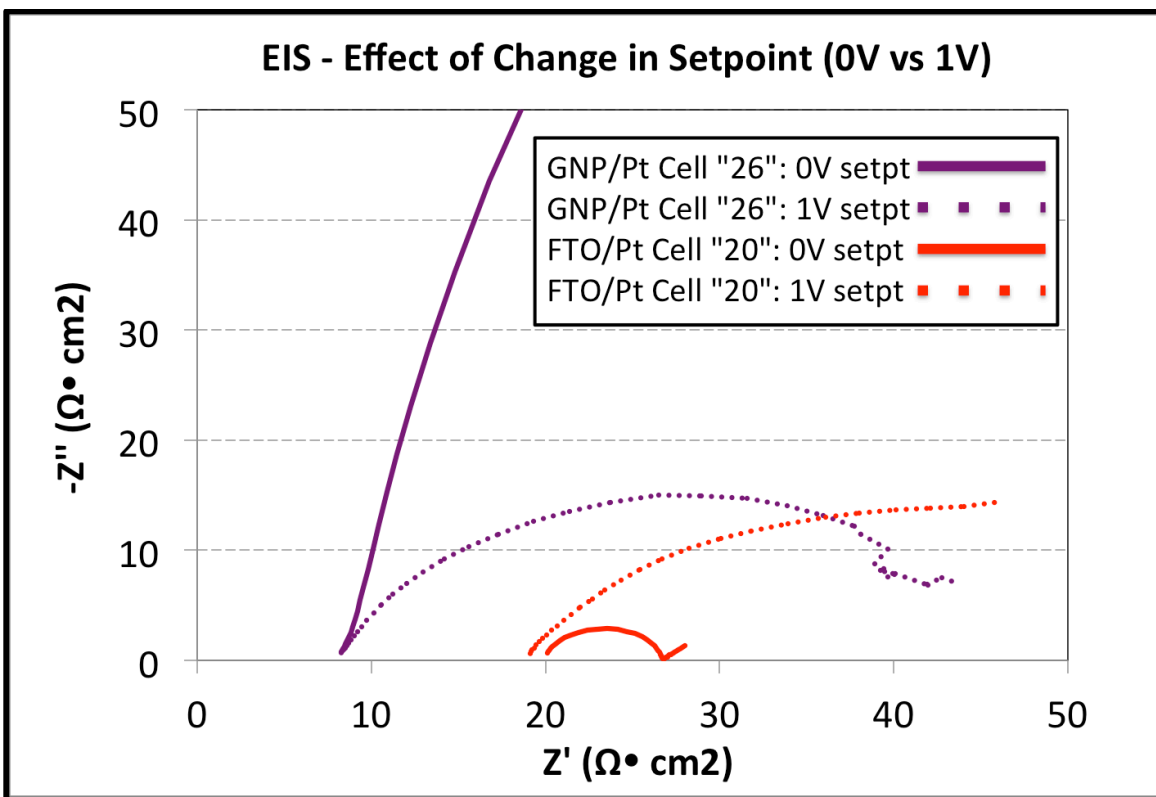


Figure 3.22: EIS measurement of GNP/PP/PtNP (1000 μM) electrode in comparison to FTO/Pt system.

A similar effect is seen at 500 mV bias, a trend noticed by Roy-Mayhew et al. in their investigation of functionalized graphene as a Pt replacement in DSSC counterelectrodes [17]. They note that the R_{CT} of their graphene samples “is 10 times greater than that of platinum at no applied bias and approaches that of platinum at applied bias” [17]. They conclude that it is “inappropriate” to use the models developed for analyzing pure Pt systems to measure R_{CT} values for carbon-based systems.

This brings up the interesting question of whether the GNP/PP/PtNP systems developed in this work are functioning because of Pt loading or because of a doping effect on the GNP. While CV and JV data suggests higher Pt loading would be responsible for better catalytic activity, the EIS data suggests otherwise. If Pt alone were

responsible for the improved performance of the prepared electrodes, R_{CT} values would be comparable to or better than FTO/Pt when measured around a 0 V bias. The fact that they behave in a similar manner to pure, functionalized graphene systems suggests the GNP may be participating in the catalysis reaction as well. The range of biases screened in EIS measurements (0.5-1.0 V) are within the range of DSSC operation, suggesting that the R_{CT} of the counterelectrode may indeed be quite low when operating in a full cell under illumination.

Conclusions

Paper-like materials made from GNP/PP proved to be ideal substrates for anchoring PtNPs. Their chemical stability and toughness allowed processing into flat substrates for DSSC counterelectrodes and the pore-filling of the polymer binder preventing leaking and delamination during cell fabrication and operation. The PtNP-decoration step proved to be controllable and robust and electrochemical analysis showed that it was suitable for catalyzing the I_3^- to I^- reduction reaction that is critical for cell operation in the most common DSSC configurations.

Most importantly, however, GNP/PP/PtNP electrodes proved to be excellent materials in actual DSSC operation. They matched and bettered the FTO/Pt standards in side-by-side comparisons and managed to do so with a significantly lower Pt loading (which was verified by two different analytic methods). Further optimization of the system can be done and the mechanism of catalysis requires further investigation (based on EIS data) but as a proof of concept, GNP/PP/PtNP systems have shown their worth.

REFERENCES

REFERENCES

- [1] R. M. Swanson, *Progress in Photovoltaics: Research and Applications* **2006**, *14*, 443–453.
- [2] B. E. Hardin, H. J. Snaith, M. D. McGehee, *Nature Photonics* **2012**, *6*, 162–169.
- [3] J. Burschka, N. Pellet, S.-J. Moon, R. Humphry-Baker, P. Gao, M. K. Nazeeruddin, M. Grätzel, *Nature* **2013**, *499*, 316–319.
- [4] A. Yella, H.-W. Lee, H. N. Tsao, C. Yi, A. K. Chandiran, M. K. Nazeeruddin, E. W.-G. Diao, C.-Y. Yeh, S. M. Zakeeruddin, M. Grätzel, *Science* **2011**, *334*, 629–634.
- [5] N. Papageorgiou, W. F. Maier, M. Graetzel, *Journal of The Electrochemical Society* **1997**, *144*, 876–884.
- [6] G. Boschloo, A. Hagfeldt, *Accounts of Chemical Research* **2009**, *42*, 1819–1826.
- [7] A. Hagfeldt, G. Boschloo, L. Sun, L. Kloo, H. Pettersson, *Chemical Reviews* **2010**, *110*, 6595–6663.
- [8] P. Joshi, L. Zhang, Q. Chen, D. Galipeau, H. Fong, Q. Qiao, *ACS Appl. Mater. Interfaces* **2010**, *2*, 3572–3577.
- [9] M. Wu, X. Lin, T. Wang, J. Qiu, T. Ma, *Energy Environ. Sci.* **2011**, *4*, 2308.
- [10] G. Calogero, P. Calandra, A. Irrera, A. Sinopoli, I. Citro, G. Di Marco, *Energy Environ. Sci.* **2011**, *4*, 1838.
- [11] Y. Wang, M. Wu, X. Lin, Z. Shi, A. Hagfeldt, T. Ma, *Journal of Materials Chemistry* **2012**, *22*, 4009.
- [12] A. Knop-Gericke, E. Kleimenov, M. H. vecker, R. Blume, D. Teschner, S. Zafeiratos, R. S. gl, V. I. Bukhtiyarov, V. V. Kaichev, I. P. Prosvirin, A. I. Nizovskii, H. Bluhm, A. Barinov, P. Dudin, M. Kiskinova, *Advances in Catalysis* **2009**, *52*, 213–272.
- [13] W. Vielstich, A. Lamm, H. A. Gasteiger, Eds., *Handbook of Fuel Cells: Fundamental Technology and Applications*, John Wiley & Sons, New York, **2012**.
- [14] T. J. Schmidt, *Journal of The Electrochemical Society* **1998**, *145*, 2354–2358.
- [15] X. Mei, S. J. Cho, B. Fan, J. Ouyang, *Nanotechnology* **2010**, *21*, 395202.

- [16] R. Bajpai, S. Roy, P. Kumar, P. Bajpai, N. Kulshrestha, J. Rafiee, N. Koratkar, D. S. Misra, *ACS Appl. Mater. Interfaces* **2011**, *3*, 3884–3889.
- [17] J. D. Roy-Mayhew, D. J. Bozym, C. Punckt, I. A. Aksay, *ACS nano* **2010**, *4*, 6203–6211.
- [18] B. O'Regan, M. Grätzel, *Nature* **1991**, *353*, 737–740.
- [19] A. Wagenpfahl, D. Rauh, M. Binder, C. Deibel, V. Dyakonov, *Physical Review B* **2010**, *82*, 115306.
- [20] I. Jeong, C. Jo, A. Anthonysamy, J.-M. Kim, E. Kang, J. Hwang, E. Ramasamy, S.-W. Rhee, J. K. Kim, K.-S. Ha, K.-W. Jun, J. Lee, *ChemSusChem* **2012**, *6*, 299–307.
- [21] Q. Wang, J. E. Moser, M. Grätzel, *The Journal of Physical Chemistry B* **2005**, *109*, 14945–14953.

Chapter 4

Graphite Nano-platelet Assemblies for Transparent Electrodes

Background

In DSSC construction, the photoanode is constructed on a substrate that is both highly electrically conductive and highly transparent to visible light. This combination of properties is quite difficult to achieve, which is reflected in the lack of diversity of materials usage. While semiconductors (TiO₂ [1], ZnO [2], polymer [3]), dyes (organic [4], Ru-based [5], Zn-based [6]), catalysts (platinum [7], carbon nanotube [8], graphene [9], vanadium [10]) and hole transport materials (liquid [11], gel [12], ionic liquid [13], polymer [3]) have been constructed from many different materials, transparent electrodes are fabricated almost entirely from tin-based oxides. The only competition, thus-far is from graphene.

The reason for the dominance of tin-based oxides (such as ITO and FTO) is the demanding nature of the application. The transparent layer is the first area for potential losses in energy conversion, making near-perfect light transmission a necessity. Complete absorption and fast electron transport within the semiconductor can't compensate for photons that never reach the dye. Commonly-used FTO allows 80-85% transparency, nearly as high as that of pure borosilicate glass [14]. And, because of the high electrical conductivity of FTO, sub-micron-thick layers can be constructed, yielding coatings with sheet resistances on the order of 10 Ω/\square [11,15]. These exceptional properties are difficult to match, making competition from other materials scarce.

However, new breakthroughs in the isolation and deposition of thin films of graphene have changed the playing field. Graphene possesses exceptional properties itself, offering a viable alternative for transparent electrodes. While a single layer of graphene absorbs 2.3% of incident white light [16], its superior electrical conductivity (estimated to be 6000 S/cm [17,18]) allows atomically thin films to provide suitable electron transport for photovoltaic devices. Bonaccorso et al. illustrate the competitive advantage of graphene-based systems with both theoretical and experimental values compared to ITO over numerous film thicknesses [19] (see Figure 4.1).

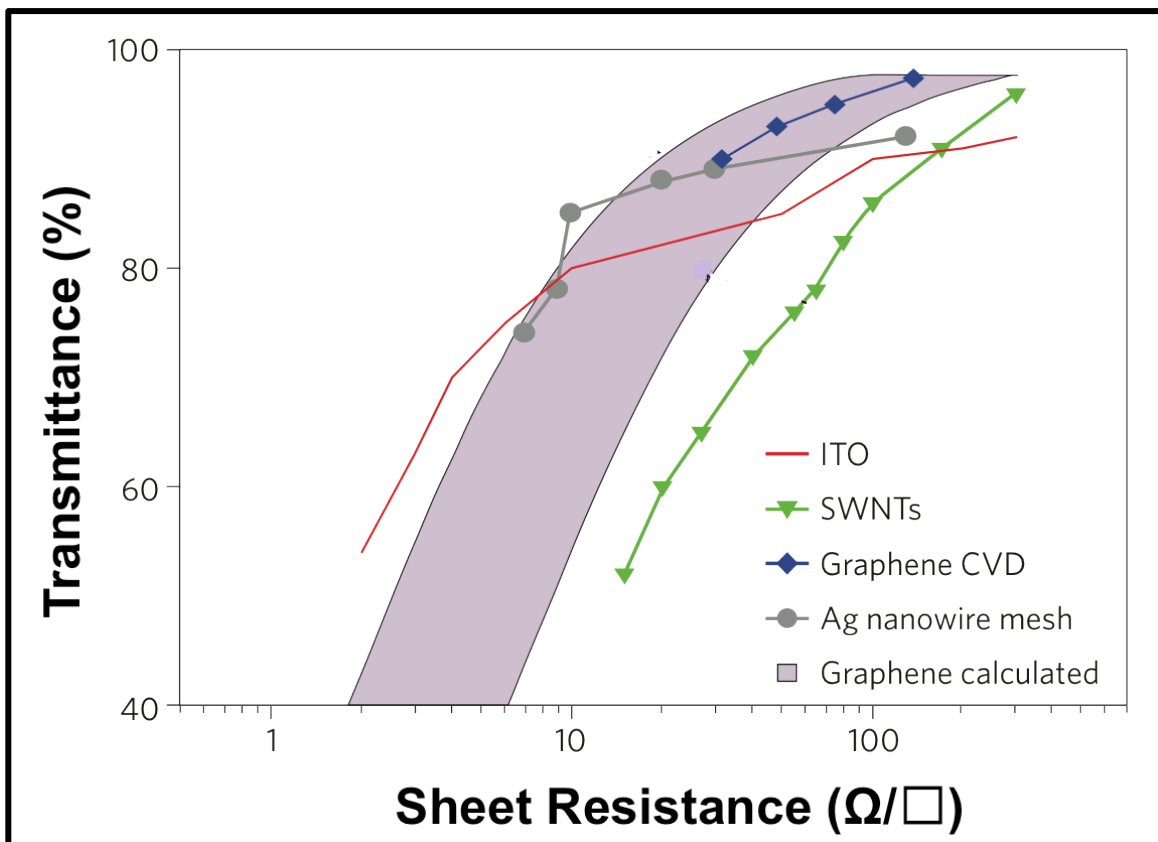


Figure 4.1: Comparison of electrical and optical properties for graphene, and ITO (as well as other potential transparent electrode systems such as silver wire mesh and single wall carbon nanotubes). Image adapted from [19].

For example, a single sheet of graphene would produce a layer approximately 98% transparent with a sheet resistance of $400 \Omega/\square$, orders of magnitude better than the resistance of a sheet of ITO with comparable transparency (tens of $k\Omega$) [20]. By stacking graphene layers, films with 90-95% transparency can be made, with sheet resistance dropping by an order of magnitude (while ITO films of comparable conductivity would provide only 80% transparency) [19].

While these values are quite promising, the movement from low-yield, small area techniques (like micromechanical cleavage [21] or epitaxial growth and transfer [22]) to larger, scalable processes is key. Rather than bottom-up approaches, work by Biswas et al. provide a possible large-scale solution [23].

Liquid-Liquid Interfacial Self-Assembly

Liquid phase exfoliation of GNP to produce suspensions of thin platelets opens up the possibility of large-scale, high-throughput processing. As opposed to epitaxial growth by chemical vapor deposition (CVD) (which requires controlled chambers and limited surface area), milligram to gram quantities of highly expanded graphite can be processed by ultrasonication. Using a two-phase system, a graphite source can be broken into thin platelets with thickness as small as 4 nm and self-assembled at a liquid-liquid interface between the two immiscible phases [24]. Disruption of this interfacial assembly transfers the thin GNP particles to the surface, allowing for deposition on hydrophilic substrates. Figure 4.2 shows the high transmittance of visible light (by UV-vis spectroscopy) at various thicknesses of deposition.

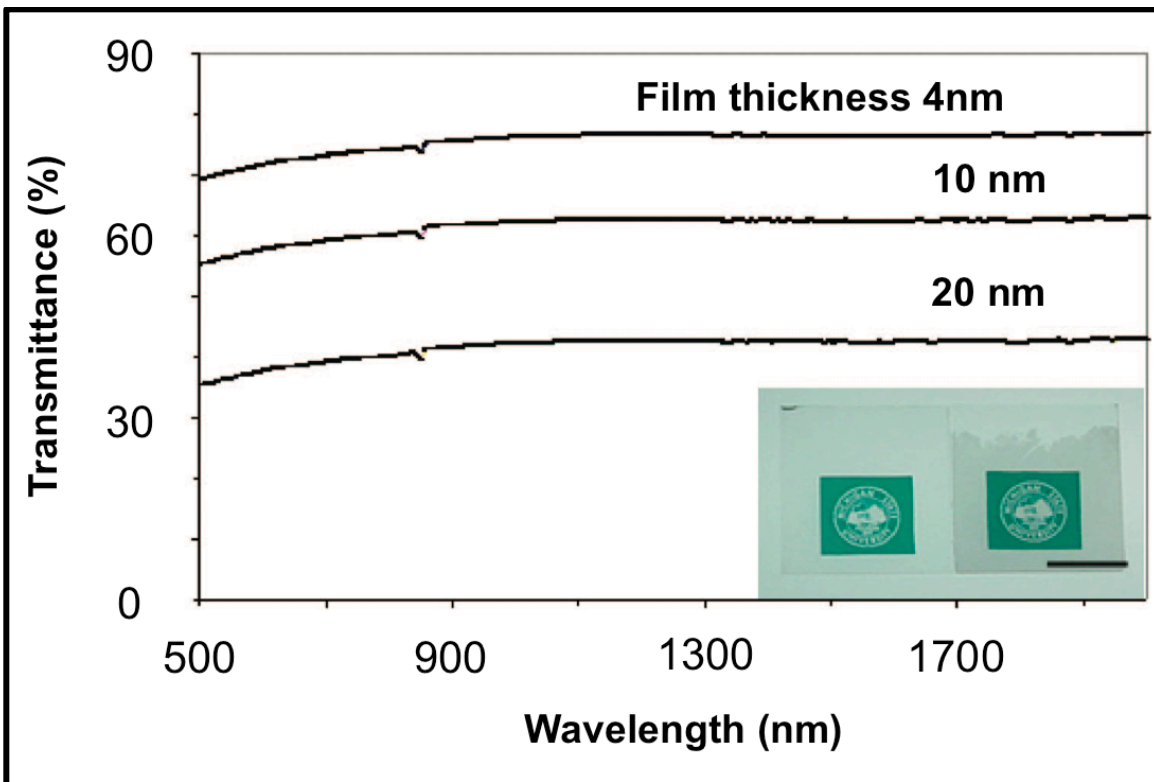


Figure 4.2: Thin film deposition of GNP resulting in highly transparent and conductive layers. Scalebar in lower right image is 1 in. Adapted from [24].

Despite this high value of optical transmittance, reaching as high as 80%, the thin films provide high electrical conductivity as well. Because the GNP networks are percolated, with platelets aligning flat on the surface and providing numerous electrically conductive pathways, values as high as 1000 S/cm are reported [24].

These excellent properties suggest a similar approach could be used for producing transparent electrodes for DSSCs. Multiple graphite sources were examined, including worms (form thermal exfoliation of Asbury GIC material – 5 min heating at 1200 W) and xGnP® material (graphite powder with BET surface area $200\text{-}300\text{ m}^2/\text{g}$, obtained from XG Sciences). Immersing 1-5 mg of dry powder in 150 ml chloroform, followed by 200 W ultrasonication for 1-2 min produced a fine dispersion of platelets, stable for several

minutes. Immediately after sonication in chloroform, addition of 75 ml RO water and continued 200 W sonication created an unstable suspension of small water droplets in chloroform. GNP collected at the chloroform-water interface, minimizing surface energy in the system [23] and formed a GNP-rich middle layer between the two phases as they separated. Disruption of this GNP-rich layer with a jet of liquid from a pipet caused chloroform to pool at the air-water interface and rapidly evaporate. The remaining GNP at the air-water interface could then be deposited on a glass slide, dried and annealed to create a stable, highly transparent layer. Figure 4.3 shows a schematic representation of the assembly and deposition process, as well as a digital image of the thin GNP layer at the air-water interface.

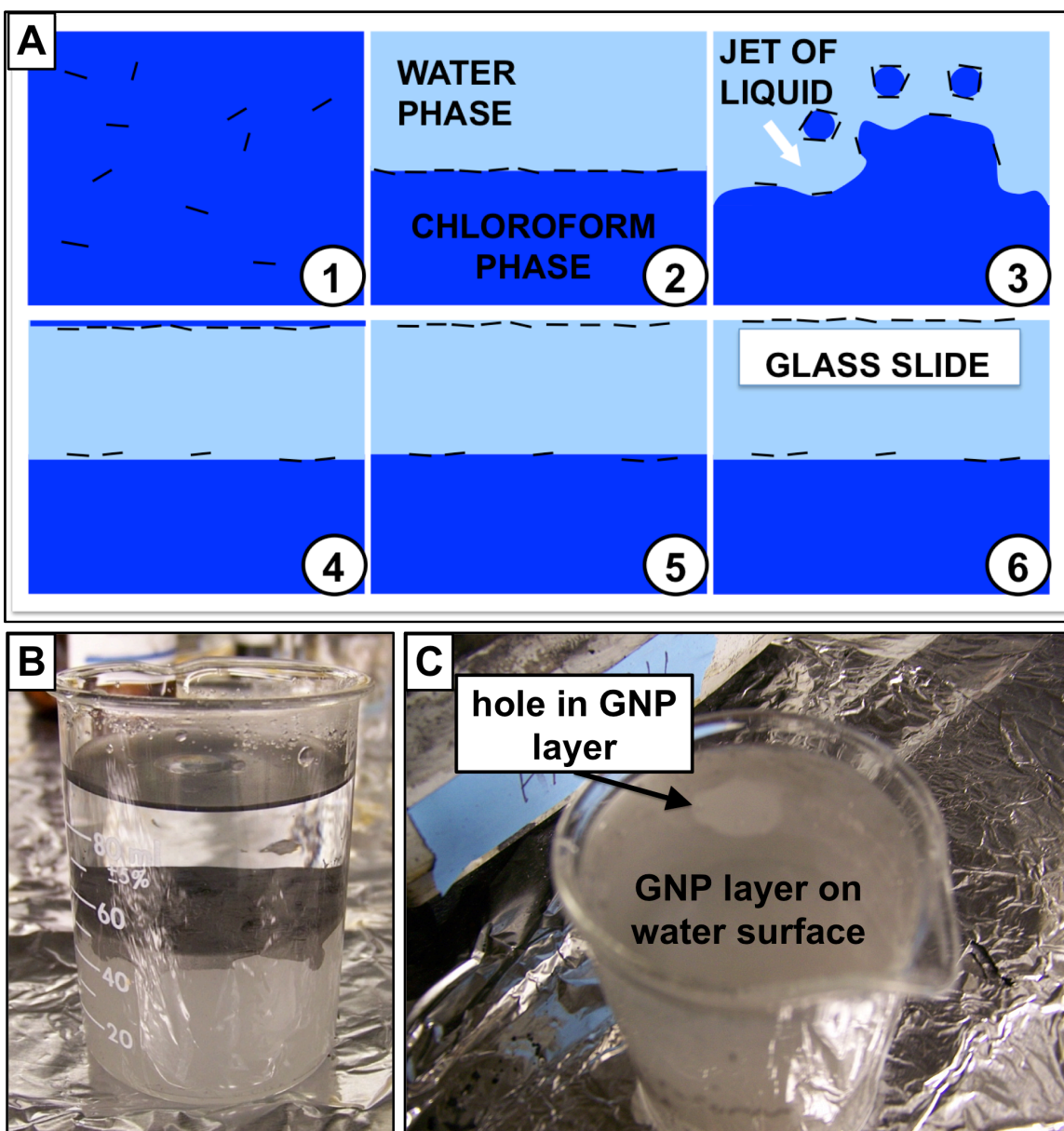


Figure 4.3: (A) Schematic representation of liquid-liquid, interfacial self-assembly of GNP. (1) sonication of GNP in chloroform to mechanically exfoliate and de-aggregate (2) addition of water and further sonication, followed by phase separation (3) disruption of GNP-rich layer but jet of liquid from pipet (4) formation of second interface at the top of the water phase (5) evaporation of chloroform, creating GNP layer at air-water interface (6) deposition of GNP layer on glass substrate. Image (B) shows the GNP-rich interface between the water on top and chloroform on bottom and image (C) shows the thin layer of GNP at the air-water interface after disruption of the water-chloroform interface and evaporation of surface chloroform.

This procedure did produce highly transparent films, reaching a maximum of 65% at 550 nm. However, problems of limited percolation of the platelets on the glass surface led to electrical conductivity values three orders of magnitude below values for thin layer graphite samples reported in literature. Figure 4.4B highlights the poor percolation among GNP platelets seen by reflected light microscopy (Keyence VHX 600 Digital Microscope).

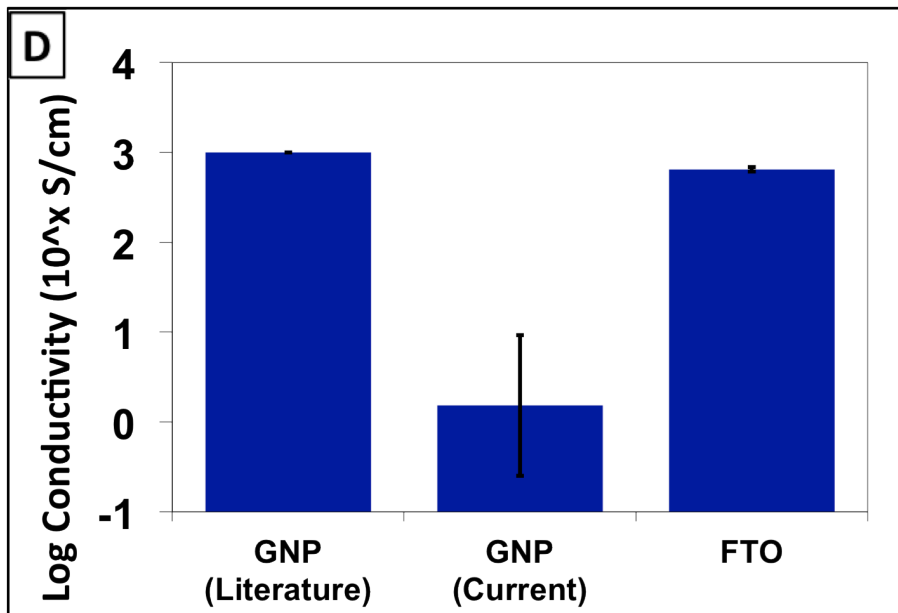
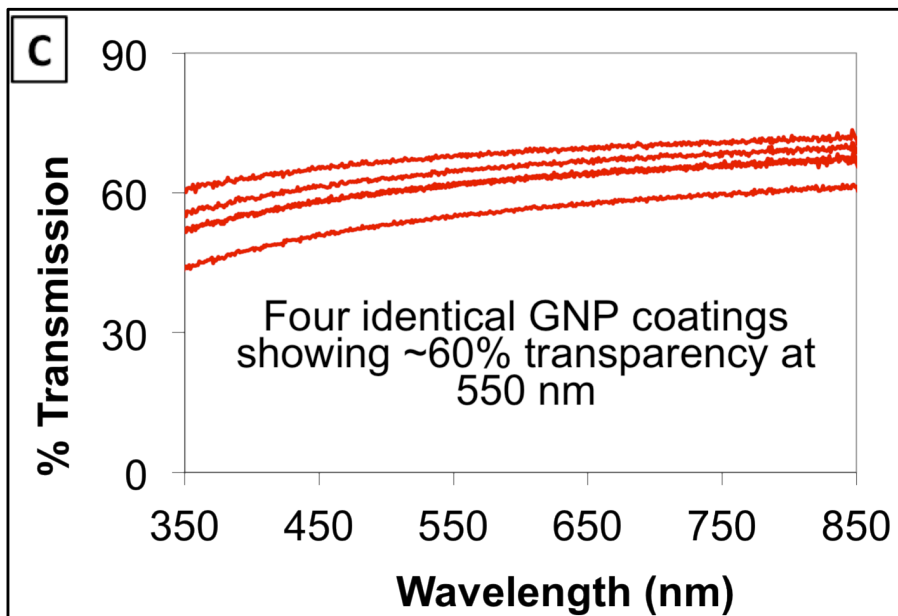
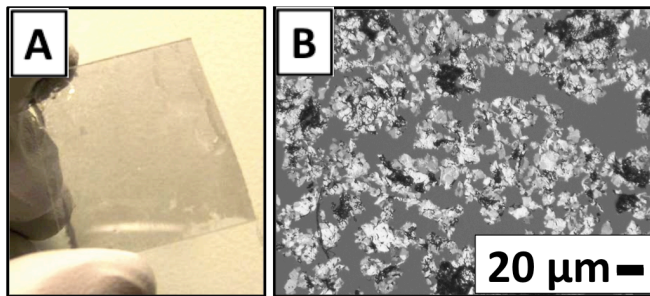


Figure 4.4: (A) Digital image and (B) optical micrograph of thin film GNP coating on glass. (C) Optical and (D) electrical properties from UV-vis spectroscopy and 2-point electrical conductivity measurements.

Tailoring the glass surface hydrophobicity by oxygen plasma treatment and silane modification was intended to improve GNP adhesion on the surface, aiding in percolation and film robustness. Water contact angle (WCA) measurement after various surface treatments can be seen in Figure 4.5C.

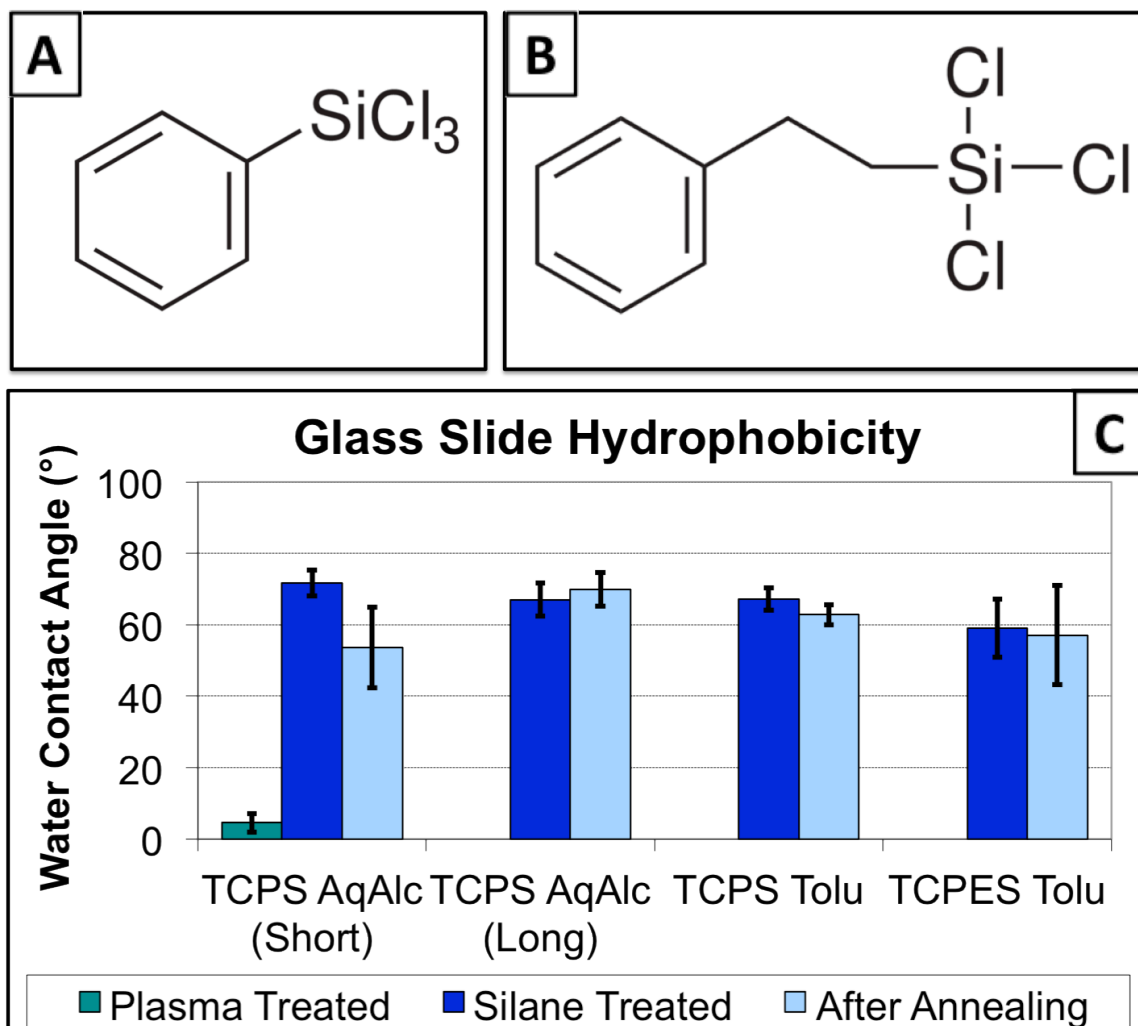


Figure 4.5: Surface treatment were performed on glass slides, including silane reaction with (A) trichloro(phenyl)silane (TCPS) and (B) trichlorophenethylsilane (TCPES). (C) Water contact angle measurements for various surface treatments.

Between the oxygen plasma treatment and reaction with various silanes with aromatic pendant groups, the chemistry of the glass surface could be tuned from highly hydrophilic (WCA~5°) to highly hydrophobic (WCA>70°). Despite measureable changes in surface

properties, change in GNP percolation was minimal. Highly hydrophilic surfaces allowed for good wetting and homogeneous GNP deposition, but poor robustness (films were easily wiped away after deposition and annealing at 250°C). Highly hydrophobic surfaces tended to coat non-uniformly, despite slight improvements in film stability. It was determined that other approaches might be better suited for transparent electrode fabrication.

Melt-Processing GNP/Polymer Substrates

Two major problems in forming uniform, highly conductive GNP films on glass were (a) proper, flat alignment of GNP particles at the film surface and (b) adhesion of GNP to the substrate. It was determined that changing substrate and GNP source might solve these problems.

In terms of GNP particle alignment, some of the most positive results were seen during paper processing. Recall Chapter 2, in which filtration of surfactant-stabilized GNP suspensions led to high alignment of platelets at the filter surface. Figure 4.6 shows the cross section of a GNP paper after filtration, annealing and pressing, highlighting the high alignment of particles at the top and bottom of the paper.

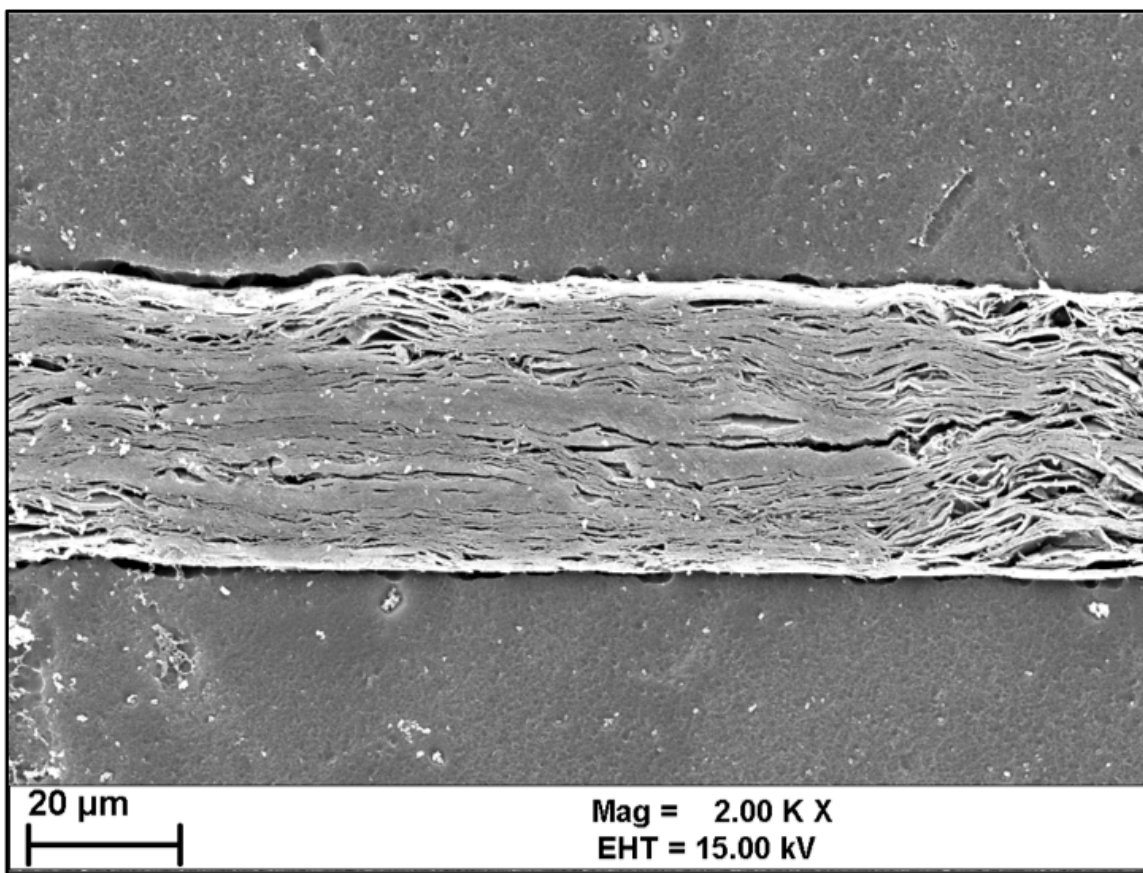


Figure 4.6: Cross section of pressed GNP paper embedded in epoxy after polishing, oxygen plasma treatment and Tugsten coating.

This highly percolated network could provide an ideal starting point for a transparent electrode, were it to be delaminated and transferred to a suitable substrate.

The original substrate choice, glass, is limited to film casting from GNP suspensions by two factors: (a) the brittleness of glass limits high-pressure compaction of films onto the surface and (b) glass must be processed in its solid state, restricting contact with the GNP, limiting adhesions between the two surfaces. In contrast, a polymer substrate is tough and flexible as well as having a low melt temperature. High-pressure compaction would allow for intimate contact between the two surfaces while melt processing would allow polymer flow, providing stronger adhesion.

Polyethylene terephthalate (PET), a well-studied substrate for flexible electronic devices [25,26], including solar cells [27], was chosen for melt processing studies. Differential scanning calorimetry (DSC) confirmed the melt temperature to be 250°C, as seen in Figure 4.7.

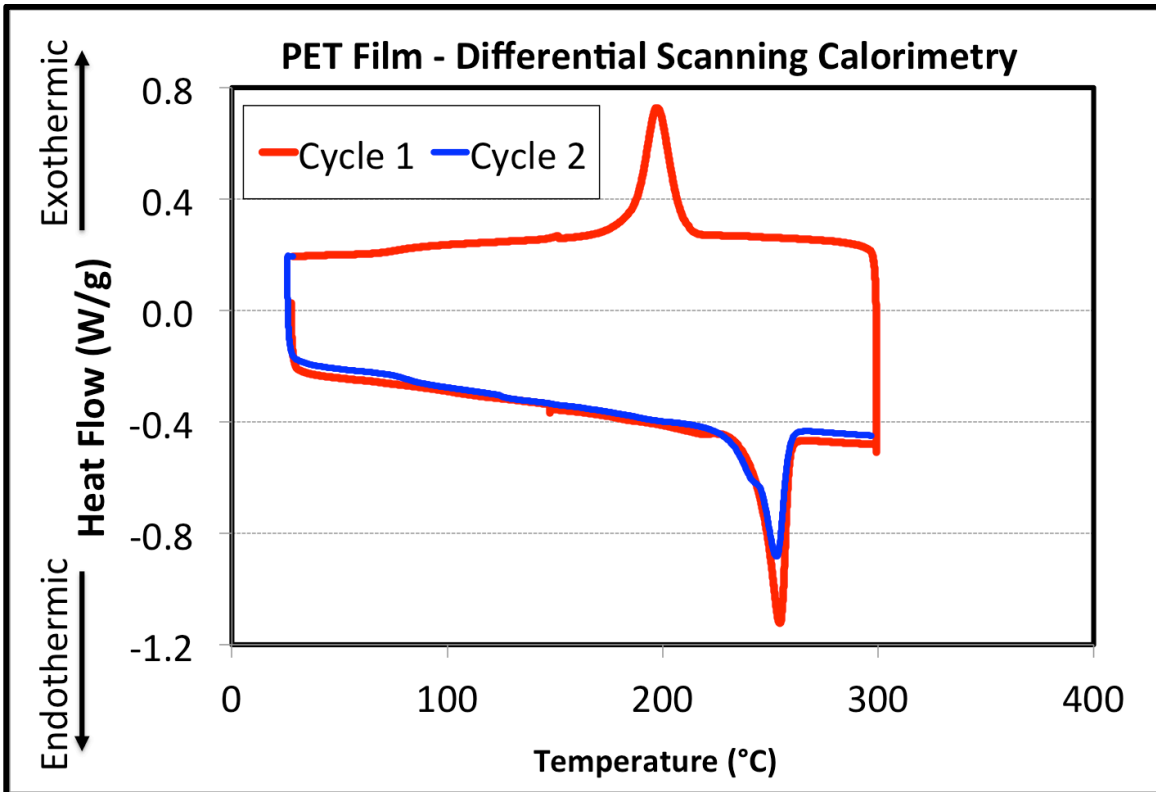


Figure 4.7: DSC characterization of PET film. Large endotherm at 250°C indicates melt transition.

Thin (0.007 in-thick) PET film was cut to 2 in by 1 in sections and pressed GNP paper was cut to size and laid on top. The sample was heated between sheets of mirror-finish aluminum foil and steel plates and heated to 250°C and held at temperature for 10 min to reach thermal equilibrium. While molten, 1000 psi of pressure was applied to the surface and then cooled (with cold water flow through the platens) while under pressure. The opaque PET/GNP was then subjected to a modified version of the micromechanical cleavage technique [21] to remove layers of GNP not immediately in contact with the

PET substrate. Adhesive tape was pressed to the GNP surface and peeled away and this process was repeated. This sequential delamination technique removed considerable GNP from the surface, but after several iterations, it became clear that many layers were not removable from the PET substrate, having been impregnated by molten polymer during melt processing. Figure 4.8 shows the PET/GNP laminate structure at various stages of processing.

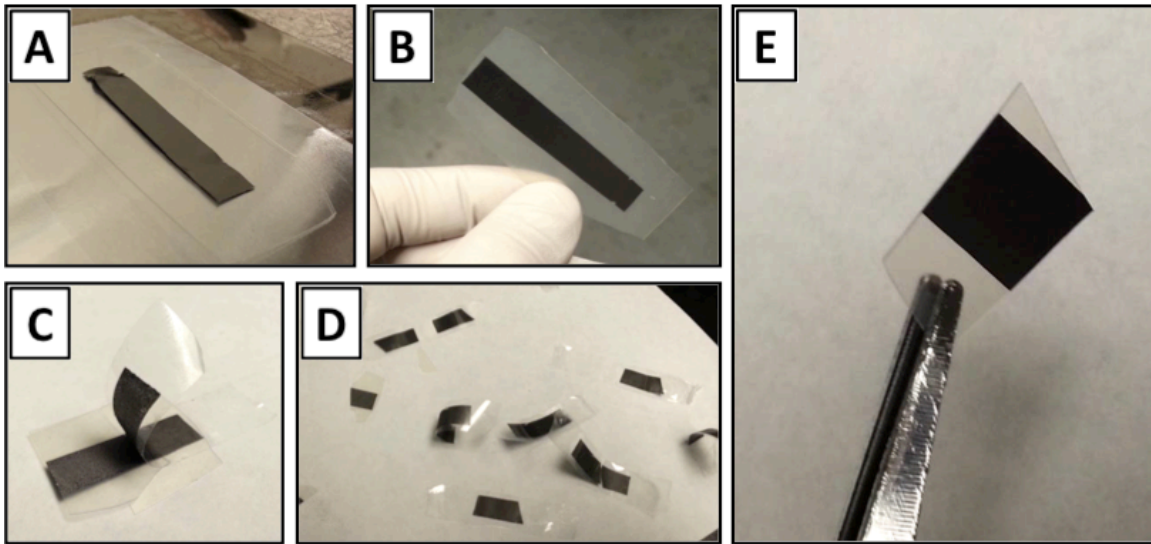


Figure 4.8: GNP/PET assembly (A) before and (B) after pressing at 250°C/1000 psi. Image (C) shows and examples of one delamination step and image (D) shows the high loading of GNP platelets in each of the subsequent delamination steps (each strip of tape is highly opaque after delamination). Image (E) shows the remaining PET/GNP structure, with very high loading of GNP remaining that cannot be removed by micromechanical cleavage.

In addition to excess GNP embedded in the polymer matrix, the PET film lost its flexibility and showed some opacity, suggesting crystallization. Processing parameters were adjusted, lowering residence time to 3 min at 250°C, pressing at 100 psi instead of 1000 and quenching the pressed sample in water bath, rapidly increasing the cooling rate. Subsequent attempts showed that PET transparency and flexibility could be largely maintained, but proper adherence of GNP was never accomplished. Some optimum

pressure and temperature may allow only a few layers for graphene to adhere to the PET surface, but it seems likely that subtle variations in GNP height and platelet interlaminar strength would prevent formation of a perfect, continuous film of high transparency.

Preliminary attempts were made with a liquid-liquid, interfacial self-assembly process on PET, similar to those experiments conducted on glass, but the surface proved inadequate for proper wetting of the water/GNP film on the surface, preventing coherent films from forming.

Conclusions

Two major approaches were tried to form highly conductive, transparent coatings for use as an electrode in DSSCs. Liquid-liquid, interfacial self-assembly has shown promise, but source material must be very thin and very pure to prevent aggregates forming during film formation. Even with well-formed films, robustness can be in issue as well. The inherent hydrophobicity of GNP makes it difficult to form stable bonds with glass substrates. It is likely that strong, covalent bonds must be formed to keep a thin GNP layer in tact during the necessary processing of a DSSC photoanode, that includes spreading TiO₂ films over the top of the electrode, as well as a high-temperature sintering process.

Pressing of GNP onto PET films was an intriguing concept as well. Melt processing has the potential to overcome some of the major issues of suspension processing on glass, but forming stable GNP films on the PET surface, prior to heating and pressing proved difficult. Using macroscopic assemblies of GNP (such as papers) proved too imprecise a

source for proper transparency. Investigating bottom-up approaches to GNP film formation prior to melt processing may yield better results.

REFERENCES

REFERENCES

- [1] B. O'Regan, M. Grätzel, *Nature* **1991**, *353*, 737–740.
- [2] M. Law, L. E. Greene, J. C. Johnson, R. Saykally, P. Yang, *Nature Materials* **2005**, *4*, 455–459.
- [3] C. J. Brabec, N. S. Sariciftci, J. C. Hummelen, *Advanced Functional Materials* **2001**, *11*, 15–26.
- [4] Y. Ooyama, Y. Harima, *European Journal of Organic Chemistry* **2009**, *2009*, 2903–2934.
- [5] Y. Sun, A. C. Onicha, M. Myahkostupov, F. N. Castellano, *Applied Materials & Interfaces* **2010**, *2*, 2039–2045.
- [6] A. Yella, H.-W. Lee, H. N. Tsao, C. Yi, A. K. Chandiran, M. K. Nazeeruddin, E. W.-G. Diao, C.-Y. Yeh, S. M. Zakeeruddin, M. Grätzel, *Science* **2011**, *334*, 629–634.
- [7] F. Cao, G. Oskam, G. J. Meyer, P. C. Searson, *The Journal of Physical Chemistry* **1996**, *100*, 17021–17027.
- [8] J. E. Trancik, S. C. Barton, J. Hone, *Nano Letters* **2008**, *8*, 982–987.
- [9] J. D. Roy-Mayhew, D. J. Bozym, C. Punckt, I. A. Aksay, *ACS nano* **2010**, *4*, 6203–6211.
- [10] M. Wu, X. Lin, Y. Wang, L. Wang, W. Guo, D. Qi, X. Peng, A. Hagfeldt, M. Grätzel, T. Ma, *Journal of the American Chemical Society* **2012**, *134*, 3419–3428.
- [11] N. Papageorgiou, W. F. Maier, M. Graetzel, *Journal of The Electrochemical Society* **1997**, *144*, 876–884.
- [12] P. Wang, S. M. Zakeeruddin, J. E. Moser, M. K. Nazeeruddin, T. Sekiguchi, M. Grätzel, *Nature Materials* **2003**, *2*, 402–407.
- [13] P. Wang, S. M. Zakeeruddin, J. E. Moser, M. Grätzel, *The Journal of Physical Chemistry B* **2003**, *107*, 13280–13285.
- [14] S. Shanthi, C. Subramanian, P. Ramasamy, *Materials Science and Engineering: B* **1999**, *57*, 127–134.
- [15] U. Bach, D. Lupo, P. Comte, J. E. J. Moser, F. Weissortel, J. Salbeck, H. Spreitzer, M. Gratzel, *Nature* **1998**, *395*, 583–585.

- [16] R. R. Nair, P. Blake, A. N. Grigorenko, K. S. Novoselov, T. J. Booth, T. Stauber, N. M. R. Peres, A. K. Geim, *Science* **2008**, *320*, 1308.
- [17] X. Du, I. Skachko, A. Barker, E. Y. Andrei, *Nature Nanotechnology* **2008**, *3*, 491–495.
- [18] C. Mattevi, G. Eda, S. Agnoli, S. Miller, K. A. Mkhoyan, O. Celik, D. Mastrogiovanni, G. Granozzi, E. Garfunkel, M. Chhowalla, *Advanced Functional Materials* **2009**, *19*, 2577–2583.
- [19] F. Bonaccorso, Z. Sun, T. Hasan, A. C. Ferrari, *Nature Photonics* **2010**, *4*, 611–622.
- [20] P. Blake, P. D. Brimicombe, R. R. Nair, T. J. Booth, D. Jiang, F. Schedin, L. A. Ponomarenko, S. V. Morozov, H. F. Gleeson, E. W. Hill, A. K. Geim, K. S. Novoselov, *Nano Letters* **2008**, *8*, 1704–1708.
- [21] C. Soldano, A. Mahmood, E. Dujardin, *Carbon* **2010**, *48*, 2127–2150.
- [22] K. S. Kim, Y. Zhao, H. Jang, S. Y. Lee, J. M. Kim, K. S. Kim, E. al, *Nature* **2009**, *457*, 706–710.
- [23] S. Biswas, Nanostructuring of Highly Aromatic Graphene Nanosheets - From Optoelectronics to Electrochemical Energy Storage Applications, Michigan State University, **2010**.
- [24] S. Biswas, L. T. Drzal, *Nano Letters* **2009**, *9*, 167–172.
- [25] A. Bessiere, J.-C. Badot, M.-C. Certiat, J. Livage, V. Lucas, N. Baffier, *Electrochimica Acta* **2001**, *46*, 2251–2256.
- [26] R. S. Tarighat, A. Goodarzi, S. Mohajerzadeh, B. Arvan, M. R. Gaderi, M. Fathipour, *Proceedings of the IEEE* **2005**, *93*, 1374–1378.
- [27] K.-H. Tsai, J.-S. Huang, M.-Y. Liu, C.-H. Chao, C.-Y. Lee, S.-C. Hung, C.-F. Lin, *Journal of The Electrochemical Society* **2009**, *156*, B1188.

Chapter 5

Conclusions and Future Work

Review

In Chapter 1, the nature of DSSCs was described and their potential for commercial application was discussed. Their unique properties, in terms of low-cost fabrication and increasingly effective energy conversion, suggest that continued refinement could make them a key player in renewable energy generation in the near future. Potential solutions to cost barriers were discussed and graphene-based materials, specifically low-cost, highly-scalable GNP, was proposed as a likely candidate.

Chapter 2 described a simple, scalable process by which PtNP-decorated GNP/PP surfaces can be made and highlighted their value in both electrical conductivity and catalytic surface area. The process was proven to be controllable and repeatable and, even under lab-scale conditions, produced gram-quantities of sample without special equipment or high-temperature processing.

In Chapter 3, these GNP/PP/PtNP surfaces were tested for potential as DSSC counterelectrodes. Despite some interesting findings in terms of Pt loading (measured by ICP-MS) and charge transfer resistance at the interface (as measured by EIS), the data showed conclusively that GNP-based electrodes provide high catalytic effect at minimal Pt loading. Full DSSCs were constructed and GNP/PP/PtNP materials beat the current standard (thermalized Pt) counterelectrode configuration in a side-by-side comparison.

Chapter 4 examined the possibility of forming thin GNP layers on various substrates to produce a highly transparent and conductive electrode. Despite the great success of GNP in numerous applications, none of the deposition and modification routes examined

showed the necessary transparency and conductivity to form a functioning DSSC photoanode. It was concluded that, as well-suited as GNP assemblies are for counterelectrodes, in applications where optical transparency is paramount, bottom-up/synthetic processes may be necessary.

In this chapter, a few potential areas for continued research are presented, for those with an interest in pursuing similar or related work. Possible avenues for improved GNP assembly properties are presented for both transparent and catalytic electrodes, as well as interesting alterations to DSSC cell design.

Transparent Electrode Improvements

Though the author has indicated that bottom-up processing of thin graphene layers may be preferable for transparent electrode fabrication, there are other possibilities for GNP-based work that have not been exhausted. The simplest of these may be repeating the same procedures (liquid-liquid, interfacial self-assembly or melt-processing with PET films) with a different GNP source. The platelets used were not particularly thin or high surface area. Drop-casting and SEM imaging the GNP materials used for electrode formation showed them to be relatively thick and rigid. Figure 5.1 shows the highly aggregated stacks of graphene sheets within each individual GNP particle, even after extensive, high-power ultrasonication.

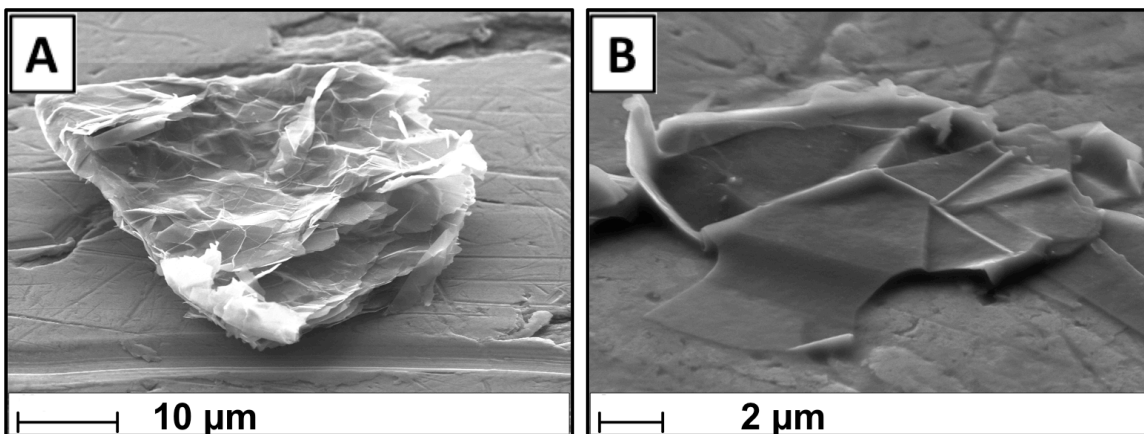


Figure 5.1: GNP from microwave exfoliated GIC (Asbury grade 3772) dropcast on Al stub and imaged by FESEM after (A) 1 min and (B) 10 min sonication in chloroform.

Even commercially exfoliated GNP sources (xGnP® from XG Sciences) shows isolated platelets to be relatively thick and rigid after an identical sonication procedure (see Figure 5.2).

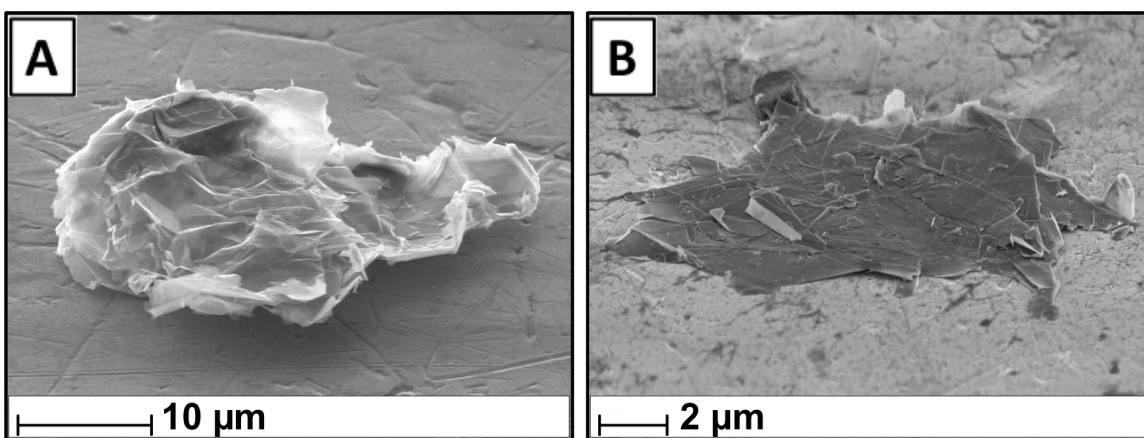


Figure 5.2: xGnP® from XG Sciences (grade M-25) after (A) 1 min and (B) 10 min sonication in chloroform.

The numerous folds and edges seen make it clear that the sample is composed of several (perhaps tens) of layers of individual graphene, making it too thick for effective transparency applications. The distinct kinks and folds in the material also suggest a rigidity that may prevent the sample from lying flat on the substrate, preventing

percolation and limiting film stability. Thinner GNP would improve both transparency and percolation (if aspect ratio is maintained). Though high-powered, mechanical exfoliation by ultrasonication appears to have limits (particle size is reduced with treatments >30 min, decreasing aspect ratio), other solution processing methods have great potential.

Isolation of very thin (few-layer) graphene from liquid exfoliation is an active research area. Providing higher yields than CVD routes and better material properties than reduction of graphite oxide (GO), these liquid-phase exfoliation and extraction techniques are more sophisticated than mechanical exfoliation by ultrasonication, but can produce individual graphene platelets. Figure 5.3 shows isolation of single platelets from a number of different, low-power exfoliation methods in a number of different solvent systems.

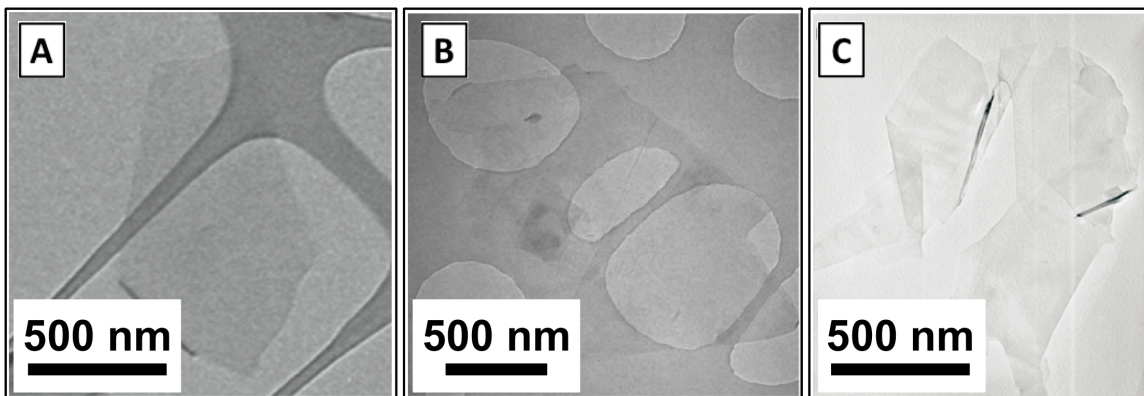


Figure 5.3: TEM images of individual graphene sheets produced by various liquid-exfoliation and extraction methods. Image (A) from bath sonication in N-methylpyrrolidone [1]. Image (B) from bath sonication in water/sodium dodecylbenzene sulfonate [2]. Image (C) from bath sonication in water/1-pyrenecarboxylic acid [3].

Though yields might be lower and purification steps (to remove surfactant or unwanted solvent may be necessary, the quality of the material produced by these techniques surpasses that of the simple horn sonication in common organic solvent. Isolating

particles this thin would greatly improve the quality of the films produced by liquid-liquid, interfacial self-assembly or melt processing on PET films. With optimization of the deposition and post-treatment, films rivaling the properties of FTO should be possible.

Another possibility for improving GNP-based thin films, would be deposition of thick layers, followed by post treatment. Brief examination of oxygen plasma treatment on layers of GNP on glass showed that reduction in film thickness and increase in transparency was possible. Figure 5.4 shows the drastic effect of the plasma treatment on the macroscopic properties of the film, as well as the extensive etching to the individual particles.

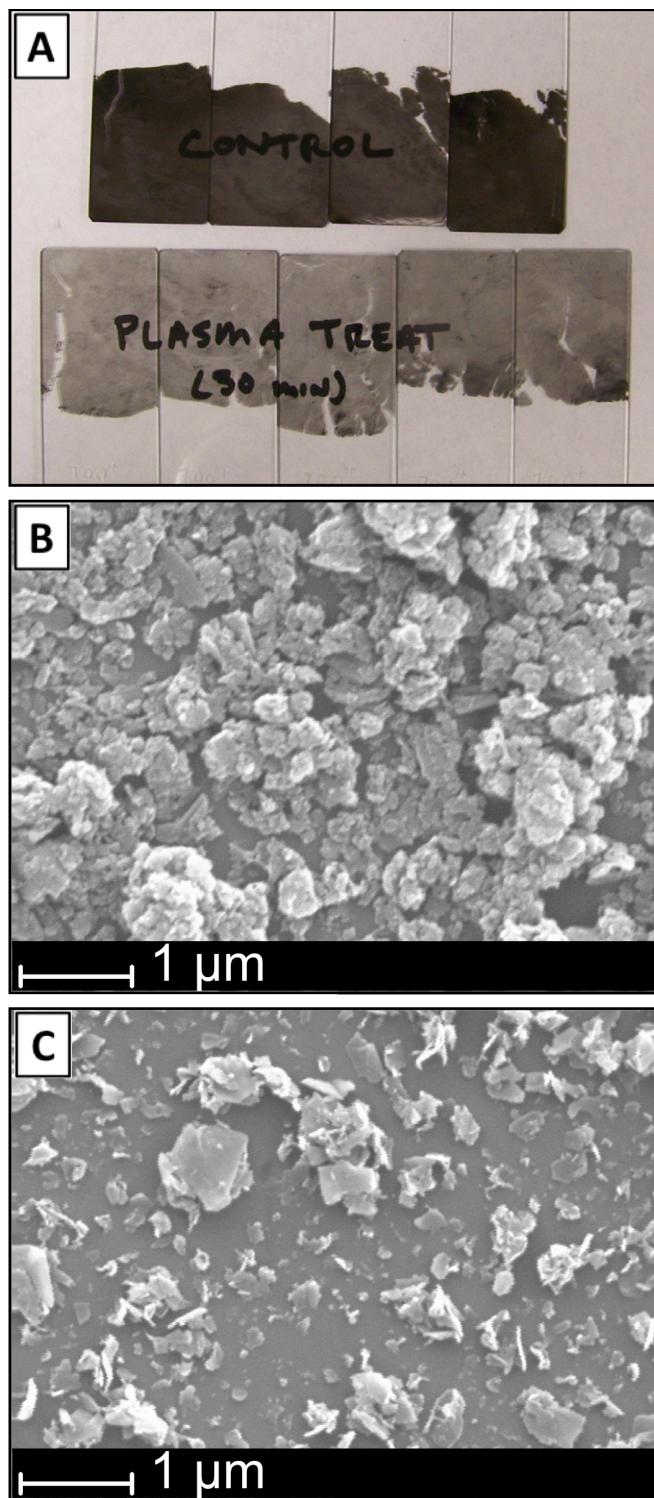


Figure 5.4: GNP films on glass were exposed to a 450 W, 30 min, 265 mtorr oxygen treatment. A Digital image (A) of the samples show dark, untreated GNP layers compared to more transparent, oxygen plasma treated samples ones. SEM imaging of the samples (B) before and (C) after the treatment show drastic changes in particle coverage.

Though the percolated network is destroyed during etching, it made clear the value of oxygen plasma to control film transparency. Literature suggests that a gentler treatment, in the range of 20-60 W, would allow single layer etching of graphene, potentially allowing percolated layers to remain intact, while reducing the number of layers of graphene within individual particles, thereby improving transparency [4,5]. Though the process is simple enough, great care would have to be taken to ensure uniform film thickness prior to plasma treatment to prevent selective etching and destruction of the percolated network.

Production of few-layer and single-layer graphene coatings by these techniques holds great promise for the DSSC field, as well as numerous other research areas. Continued development of these techniques should be closely monitored as future generations of DSSC devices could benefit from their application.

Counterelectrode Improvement

While thin film, transparent GNP proved inadequate for actual DSSC construction, GNP-based counterelectrodes performed admirably. The fabrication technique could be taken in a number of different directions. Firstly, UV-vis spectroscopy data of the GNP surfaces, in comparison with standard, thermalized Pt on FTO electrodes, showed that part of the success of GNP-based devices might be improved reflectance. Figure 5.5 compares the two surfaces over the range of visible light.

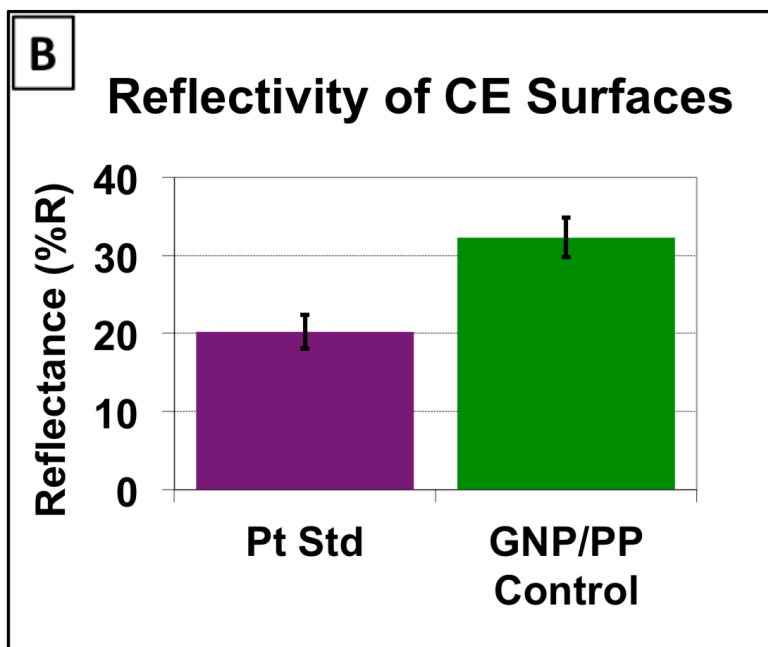
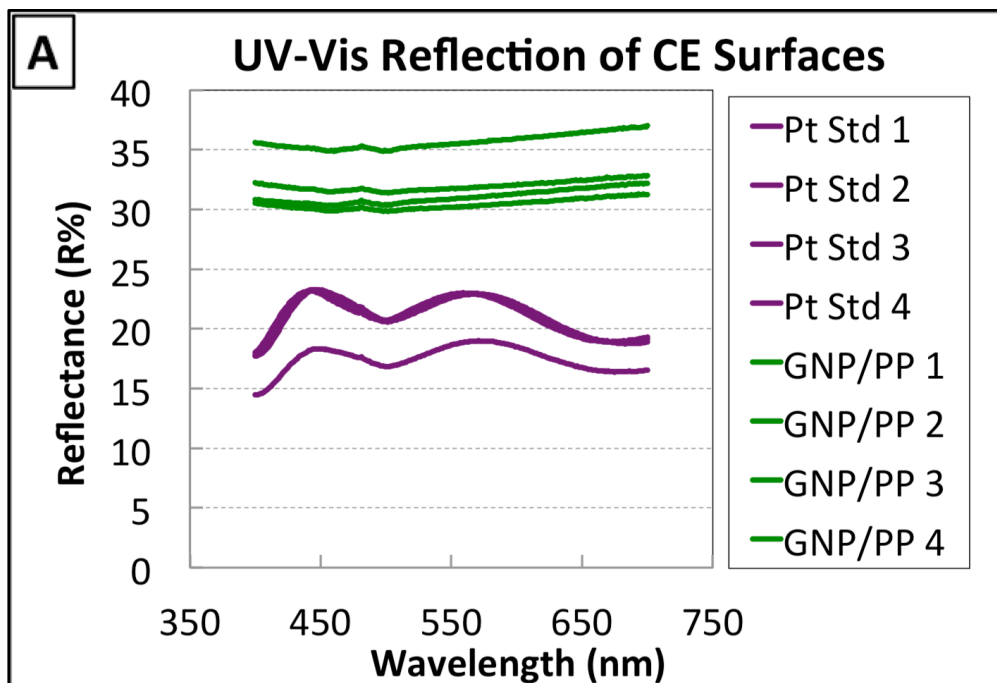


Figure 5.5: UV-vis comparison of GNP/PP and FTO/Pt counterelectrode samples. (A) Spectra of various samples plotted for range of visible light and (B) comparison of average surface reflectance over visible range.

Pressing of GNP/PP papers in contact with mirror finish aluminum foil likely account for the limited topology and high reflectance. Optimization of compression molding

parameters (mold temperature, applied pressure, cooling rate) might improve reflectivity even more, potentially improving cell efficiency.

Secondly, expanding the range of Pt loadings might yield improvements in cell performance. The highest PtNP loading on the GNP substrates was still a factor for four (at least) below the standard. Increasing CPA concentration in solution during the microwave heating/PtNP synthesis process should increase the surface area for catalysis and potentially improve the conversion efficiency of the cell.

Lastly, but perhaps most intriguing, is possibility of *removal* of Pt from the system entirely. Pure GNP/PP samples (with surfaces cleared of polymer by oxygen plasma etching) showed poor cell performance, but *still* produced measurable photocurrent. Other research groups have investigated high surface area carbon materials for counterelectrodes and shown promising results [6-8]. Functionalization of the GNP counterelectrode or use of a high surface area material, such as commercially available xGnP-C-700 (from XG Sciences, BET Surface area $\sim 755 \text{ m}^2/\text{g}$) should greatly improve the catalytic effect compared to the flat, compacted platelets used in the GNP/PP paper-making process. Preliminary work, placing this high-surface area xGnP-C-700 on lower surface area platelets, can be seen in Figure 5.6.

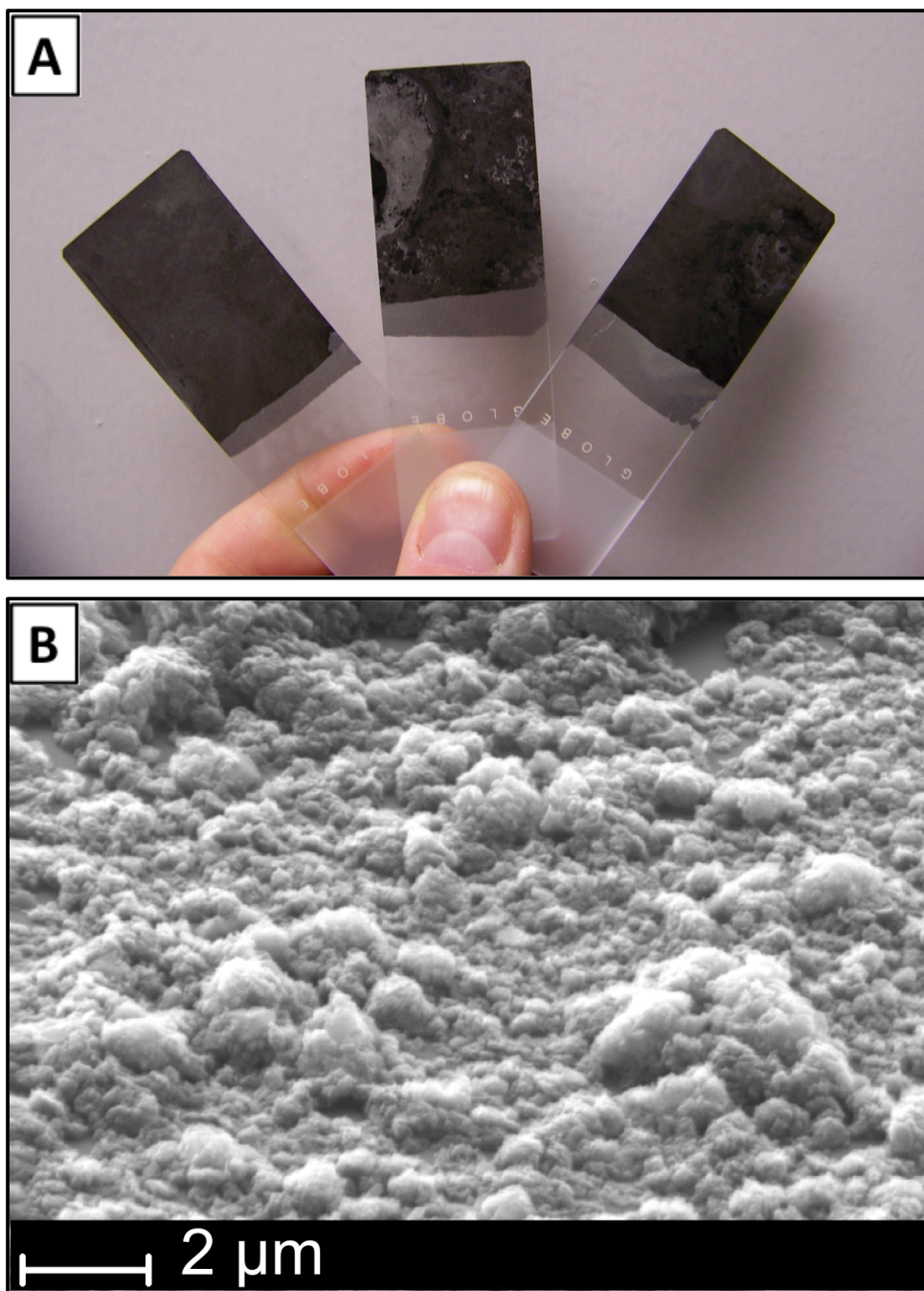


Figure 5.6: (A) Digital image of high surface area xGnP-C-700 material deposited on thin layers of low surface area graphite by multiple liquid-liquid, interfacial self-assembly interaction. (B) SEM imaging of the surface shows the high surface area of the deposited material, likely improving catalytic ability.

While the high surface area material lacks the electrical conductivity of its low-surface area counterpart, the bi-layer provides a unique synergy, providing both high electrical conductivity *and* high surface area.

Movement towards Pt-free systems is evident in literature [9-12], suggesting Pt loading reduction may not be the best route to commercial viability. Relying on Pt-free systems, build from low-cost graphite sources could be a leap forward in terms of cost improvements. And, with proper engineering of the catalytic surface, it may be done without sacrificing performance.

Counterelectrode design for DSSC is a diverse topic so this short list of future improvements to GNP-based electrode design is by no means exhaustive. In fact, the diversity of GNP in terms of morphology, properties and potential functionalization make the possibilities limitless.

DSSC Efficiency Improvement

While the comparison between GNP-based and FTO-based electrodes was informative, the absolute performance of the cells was below the values seen in literature. Values of conversion efficiency around 1.5% were achieved in this work, far below the 7-10% commonly reported [13-15]. It was assumed originally that the size of the cells constructed (with a photosensitized TiO₂ area of 1 cm by 1 cm), double the length and width of many cells reported in literature, was large enough to cause resistive losses, limiting performance. Smaller cells, with 5 mm by 5 mm TiO₂ layers, were constructed and tested for conversion efficiency. Figure 5.7 shows the cell dimensions before and after assembly.

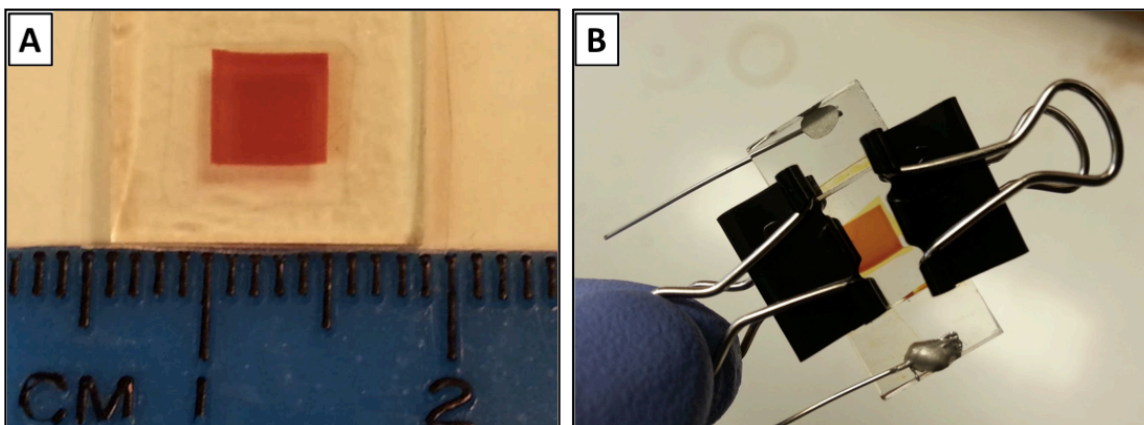


Figure 5.7: Digital images of (A) 5 mm by 5 mm photoanode after dyeing and drying and (B) cell construction with standardized FTO/Pt counterelectrode and LiI, I₂, TBP electrolyte.

Despite reducing lateral dimensions and keeping all other cells parameters constant, no change in cell efficiency was observed. Similarly, changing from 700 μm thick EPDM rubber gaskets, to silicone-based gaskets only 100 μm thick, made no difference in cell efficiencies.

Another possibility was that back reactions between the photoanode and electrolyte were causing current losses, leading to poor cell efficiencies. To correct for this, a 15 nm TiO₂ blocking layer, formed by atomic layer deposition (ALD) was placed between the mesoporous semiconductor layer and FTO current collector. Again, full cells were constructed with standard dye, electrolyte and counterelectrode configuration, and no change in efficiency was seen. JV curves for the different cell configurations can be seen in Figure 5.8.

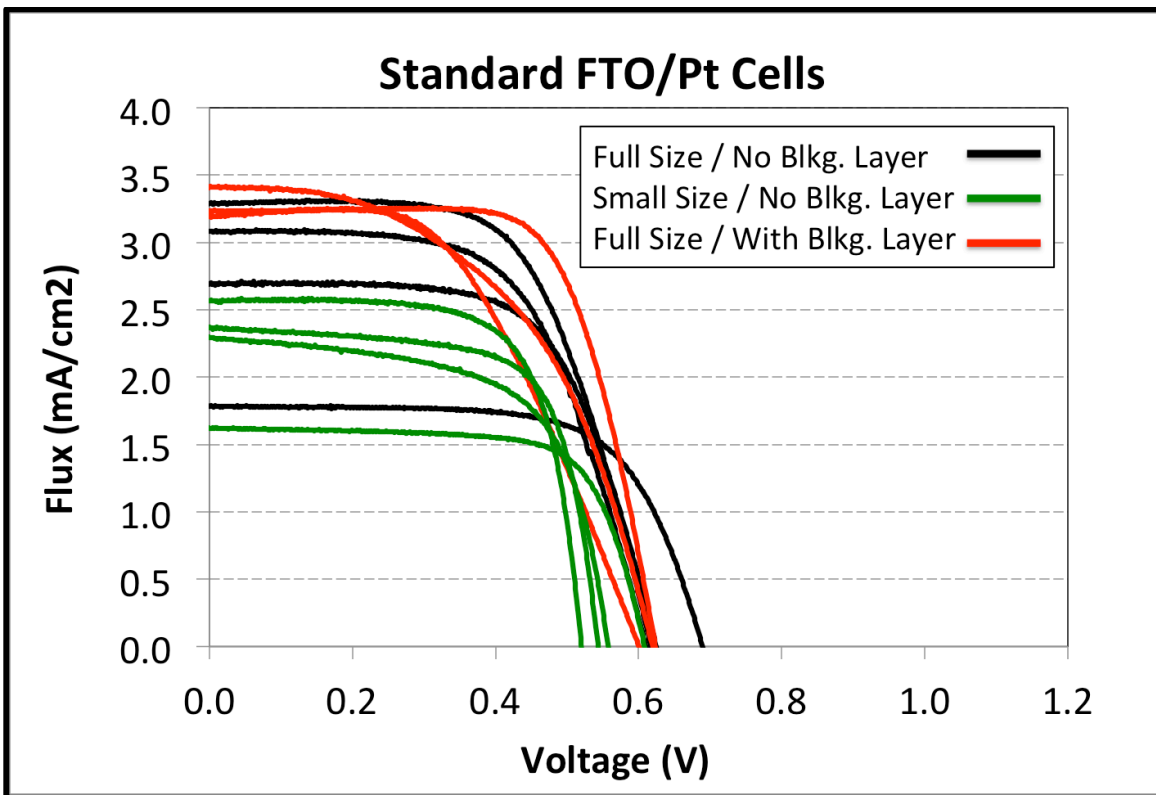


Figure 5.8: JV curve comparison various FTO/Pt DSSC configurations.

Despite changing photoanode dimensions, limiting diffusion distances by thinning the gasket material and adding a blocking layer to prevent back reactions, no improvement in DSSC performance was seen.

It is still unclear as to why these cells exhibit such low performance. Extensive characterization of the dye and electrodes suggested no obvious remedies. Future work, perhaps with different dye systems or electrolyte composition might elucidate the problem and provide efficiency measurements more consistent with the values reported in literature.

PET Substrates for Flexible Devices

In addition to cost reduction in counterelectrode materials, improving processibility is vital for commercialization. Pressing GNP/PP/PtNP papers onto glass provides a

simple structure for lab-scale observation, but changing from rigid glass to flexible polyester would be desirable for the next iteration of the cell in terms of scalability, weight savings and flexibility (allowing for photovoltaic devices that conform to curved or irregular surfaces).

Preliminary work has been done, taking PtNP-decorated GNP/PP papers and hot pressing (~5000 psi) onto polyethylene terephthalate (PET) backing at 180°C (above the melt temperature of PP). The excellent adhesion of the GNP/PP/PtNP to the PET surface and high flexibility can be seen in Figure 5.9.

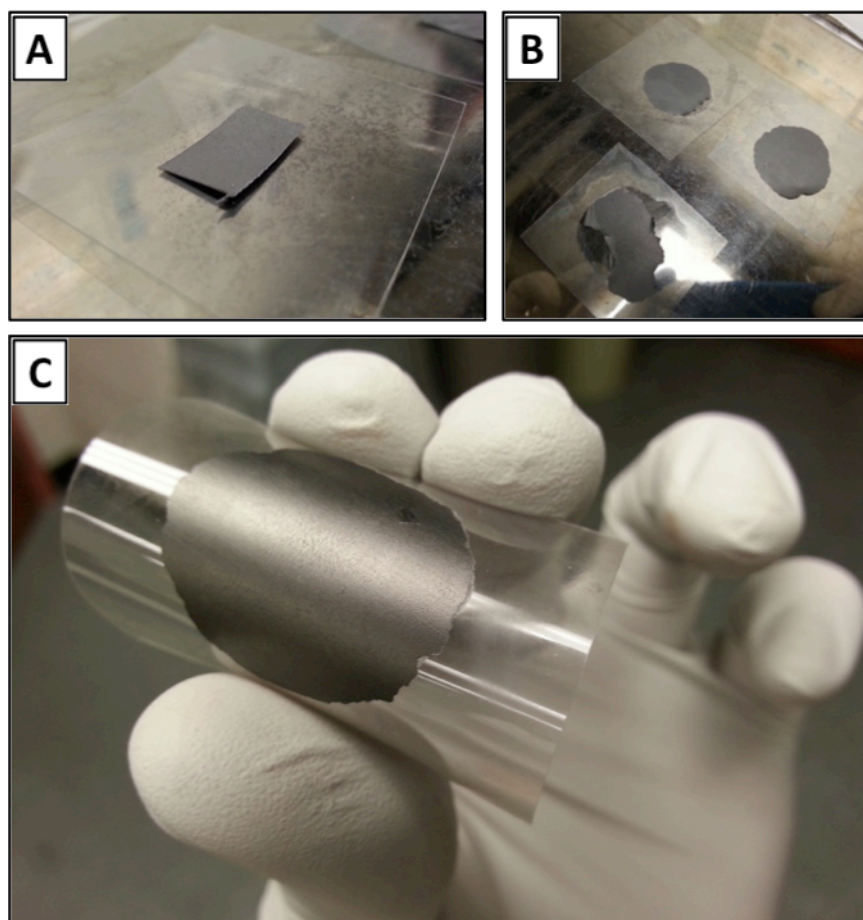


Figure 5.9: GNP/PP/PtNP paper on PET film (A) before and (B) after pressing. Image (C) shows the stability of the film during repeated flexing.

The dimensional change of the GNP/PP during pressing, however, suggested PP flow during the molding operation. An oxygen plasma treatment (40 min, 450 W, 265 mtorr O_2) was used to clear PP from the PtNP-decorated surface. FESEM of the treated surface confirmed the presence of the PtNPs after hot pressing to the PET backing, as seen in Figure 5.10.

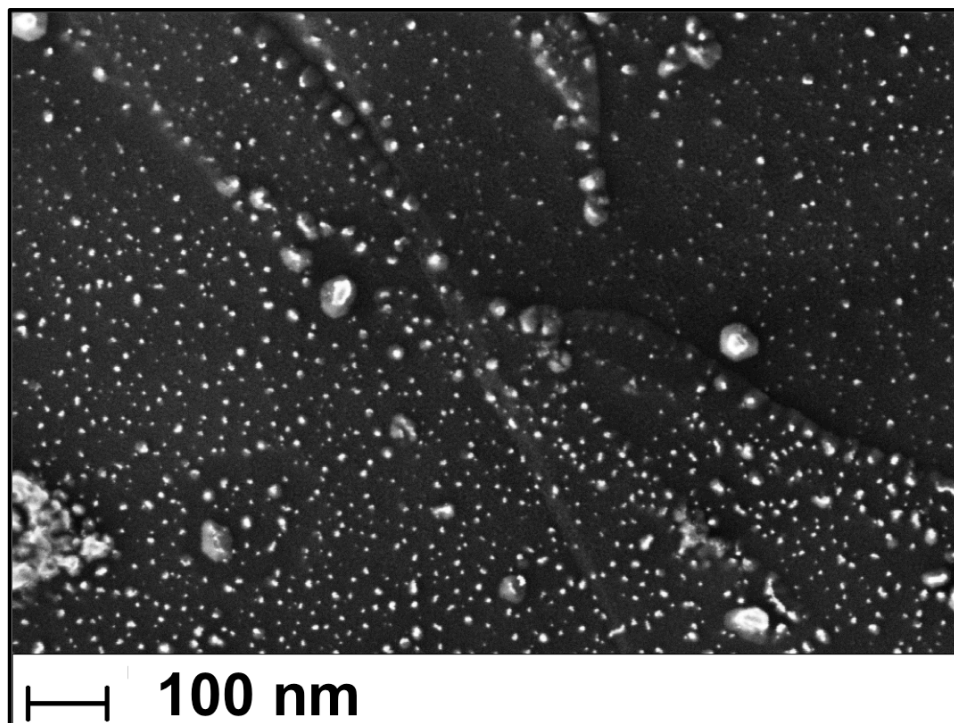


Figure 5.10: PtNP presence on PET/GNP/PP/PtNP structure after pressing and oxygen plasma treatment. Confirmation of Pt presence was provided by back-scatter imaging of the same area.

The long-term stability of the PET/GNP/PP/PtNP system has not been studied and molding conditions have not been optimized. This system holds great promise, however, because it provides all the key features desired in catalytic electrode systems: flexibility, light weight, low-cost constituent materials, low processing temperature and low capital equipment cost for processing.

If further work in this area were to be pursued, construction of a full cell with a flexible photoanode [16] should be considered. Proving full cell function with a low-cost, flexible counterelectrode would be a valuable step towards large-scale DSSC commercialization.

Conclusions

This thesis describes several approaches implementing low-cost, high-performance GNP materials into DSSC fabrication. Both transparent and catalytic electrodes have the potential to be improved by proper application of GNP assemblies and simple, scalable procedures can be used to produce them. The most promising avenue is catalytic counterelectrode fabrication, in which significant reductions in Pt loading have been achieved and the performance of full cells under standard conditions has been matched and surpassed. Mechanically robust, chemically stable GNP/PP/PtNP surfaces provide a unique surface with excellent catalytic and electronic properties. While future refinement may lead to performance improvement in DSSC, and even application to other devices and processes, its incorporation into DSSC function has already proven its worth.

REFERENCES

REFERENCES

- [1] Y. Hernandez, V. Nicolosi, M. Lotya, F. M. Blighe, Z. Sun, S. De, I. T. McGovern, B. Holland, M. Byrne, Y. K. Gun'Ko, J. J. Boland, P. Niraj, G. Duesberg, S. Krishnamurthy, R. Goodhue, J. Hutchison, V. Scardaci, A. C. Ferrari, J. N. Coleman, *Nature Nanotechnology* **2008**, *3*, 563–568.
- [2] M. Lotya, Y. Hernandez, P. J. King, R. J. Smith, V. Nicolosi, L. S. Karlsson, F. M. Blighe, S. De, Z. Wang, I. T. McGovern, G. S. Duesberg, J. N. Coleman, *Journal of the American Chemical Society* **2009**, *131*, 3611–3620.
- [3] X. An, T. Simmons, R. Shah, C. Wolfe, K. M. Lewis, M. Washington, S. K. Nayak, S. Talapatra, S. Kar, *Nano Letters* **2010**, *10*, 4295–4301.
- [4] J. D. Jones, R. K. Shah, G. F. Verbeck, J. M. Perez, *Small* **2012**, *7*, 1066–1072.
- [5] T. Feng, D. Xie, H. Tian, P. Peng, D. Zhang, D. Fu, T. Ren, X. Li, H. Zhu, Y. Jing, *Materials Letters* **2012**, *73*, 187–189.
- [6] M. Wu, X. Lin, T. Wang, J. Qiu, T. Ma, *Energy Environ. Sci.* **2011**, *4*, 2308.
- [7] J. E. Trancik, S. C. Barton, J. Hone, *Nano Letters* **2008**, *8*, 982–987.
- [8] J. D. Roy-Mayhew, D. J. Bozym, C. Punckt, I. A. Aksay, *ACS nano* **2010**, *4*, 6203–6211.
- [9] M. Wu, X. Lin, Y. Wang, L. Wang, W. Guo, D. Qi, X. Peng, A. Hagfeldt, M. Grätzel, T. Ma, *Journal of the American Chemical Society* **2012**, *134*, 3419–3428.
- [10] J. Burschka, N. Pellet, S.-J. Moon, R. Humphry-Baker, P. Gao, M. K. Nazeeruddin, M. Grätzel, *Nature* **2013**, *499*, 316–319.
- [11] Y. Wang, M. Wu, X. Lin, Z. Shi, A. Hagfeldt, T. Ma, *Journal of Materials Chemistry* **2012**, *22*, 4009.
- [12] I. Chung, B. Lee, J. He, R. P. H. Chang, M. G. Kanatzidis, *Nature* **2012**, *485*, 486–489.
- [13] M. Grätzel, *Journal of Photochemistry and Photobiology C: Photochemistry Reviews* **2003**, *4*, 145–153.
- [14] A. Hagfeldt, M. Grätzel, *Accounts of Chemical Research* **2000**, *33*, 269–277.
- [15] B. O'Regan, M. Grätzel, *Nature* **1991**, *353*, 737–740.

- [16] C. Longo, A. F. Nogueira, M.-A. De Paoli, H. Cachet, *The Journal of Physical Chemistry B* **2002**, *106*, 5925–5930.